Hard X-Ray Photoelectron Spectroscopy of Bulk and Thin Films of Heusler Compounds

Dissertation
zur Erlangung des Grades
"Doktor der Naturwissenschaften"
am Fachbereich Physik, Mathematik und Informatik
der Johannes Gutenberg-Universität Mainz

vorgelegt von
Xeniya Kozina
geboren in Almaty/Kazakhstan

Mainz, 2012

Tag der mündlichen Prüfung: 26. März 2012

Die vorliegende Arbeit wurde in der Zeit von Nov 2008 bis Feb 2012 am Institut für Anorganische und Analytische Chemie im Fachbereich Chemie, Pharmazie und Geowissenschaften der Johannes Gutenberg-Universität, Mainz angefertigt.

Mainz, Februar 2012

Hiermit versichere ich, dass ich die vorliegende Dissertation selbstständig verfasst und keine anderen als die angegebenen Hilfsmittel benutzt habe. Alle der Literatur entnommenen Stellen sind als solche gekennzeichnet.

Mainz, Februar 2012

1 List of Publications

1. *Electronic structure and symmetry of valence states of epitaxial NiTiSn and $NiZr_{0.5}Hf_{0.5}Sn$ thin films by hard x-ray photoelectron spectroscopy*
   Xeniya Kozina, Tino Jaeger, Siham Ouardi, Andrei Gloskowskij, Gregory Stryganyuk, Gerhard Jakob, Takeharu Sugiyama, Eiji Ikenaga, Gerhard H. Fecher, and Claudia Felser
   Appl. Phys. Lett., 99, 221908 (2011)

2. *Magnetic dichroism in angle-resolved hard x-ray photoemission from buried layers*
   Xeniya Kozina, Gerhard H. Fecher, Gregory Stryganyuk, Siham Ouardi, Benjamin Balke, Claudia Felser, Gerd Schönhense, Eiji Ikenaga, Takeharu Sugiyama, Naomi Kawamura, Motohiro Suzuki, Tomoyuki Taira, Tetsuya Uemura, Masafumi Yamamoto, Hiroaki Sukegawa, Wenhong Wang, Koichiro Inomata, and Keisuke Kobayashi
   Phys. Rev. B, 84, 054449 (2011)

3. *A nondestructive analysis of the B diffusion in Ta-CoFeB-MgO-CoFeB-Ta magnetic tunnel junctions by hard x-ray photoemission*
   Xeniya Kozina, Siham Ouardi, Benjamin Balke, Gregory Stryganyuk, Gerhard H. Fecher, Claudia Felser, Shoji Ikeda, Hideo Ohno, and Eiji Ikenaga
   Appl. Phys. Lett., 96, 072105 (2010)

4. *Valence states of off-stoichiometric thin films based on the Heusler compound Co_2MnSi*
   Xeniya Kozina, Siham Ouardi, Gregory Stryganyuk, Benjamin Balke, Stanislav Chadov, Gerhard H. Fecher, Claudia Felser, Takayuki Ishikawa, Tetsuya Uemura, Masafumi Yamamoto, Eiji Ikenaga, Yoshiyuki Yamashita, Shigenori Ueda, and Keisuke Kobayashi
   J. Phys. D: Appl. Phys., *under review*

5. *Spin polarimetry and magnetic dichroism on a buried magnetic layer using hard x-ray photoelectron spectroscopy*
   Gregory Stryganyuk, Xeniya Kozina, Gerhard H. Fecher, Siham Ouardi, Stanislav Chadov, Claudia Felser, Gerd Schönhense, Andreas Oelsner, Pasqual Bernhard,

Eiji Ikenaga, Takeharu Sugiyama, Hiroaki Sukegawa, Zhenchao Wen, Koichiro Inomata, and Keisuke Kobayashi
Jap. J. Appl. Phys., 51, 016602 (2012)

6. *Symmetry of Valence States of Heusler Compounds Explored by Linear Dichroism in Hard-X-Ray Photoelectron Spectroscopy*
Siham Ouardi, Gerhard H. Fecher, Xeniya Kozina, Gregory Stryganyuk, Benjamin Balke, Claudia Felser, Eiji Ikenaga, Takeharu Sugiyama, Naomi Kawamura, Motohiro Suzuki, and Keisuke Kobayashi
Phys. Rev. Lett., 107, 036402 (2011)

7. *Epitaxial growth and thermoelectric properties of TiNiSn and $Zr_{0.5}Hf_{0.5}NiSn$ thin films*
Tino Jaeger, Christian Mix, Michael Schwall, Xeniya Kozina, Joachim Barth, Benjamin Balkeb, Martin Finsterbusch, Yves U. Idzerda, Claudia Felser, and Gerhard Jakob
Thin Solid Films, 520, 1010-1014 (2011)

8. *Electronic structure of Pt based topological Heusler compounds with C_{1b} structure and "zero band gap"*
Siham Ouardi, Chandra Shekhar, Gerhard H. Fecher, Xeniya Kozina, Gregory Stryganyuk, Claudia Felser, Shigenori Ueda, and Keisuke Kobayashi
Appl. Phys. Lett., 98, 211901 (2011)

9. *Exploring the details of the martensite-austenite phase transition of the shape memory Heusler compound Mn_2NiGa by hard x-ray photoelectron spectroscopy, magnetic and transport measurements*
Christian G. F. Blum, Siham Ouardi, Gerhard H. Fecher, Benjamin Balke, Xeniya Kozina, Gregory Stryganyuk, Shigenori Ueda, Keisuke Kobayashi, Claudia Felser, Sabine Wurmehl, and Bernd Bchner
Appl. Phys. Lett., 98, 252501 (2011)

10. *Thermoelectric properties and electronic structure of substituted Heusler compounds: $NiTi_{0.3-x}ScxZr_{0.35}Hf_{0.35}Sn$*
Siham Ouardi, Gerhard H. Fecher, Benjamin Balke, Michael Schwall, Xeniya Kozina, Gregory Stryganyuk, Claudia Felser, Eiji Ikenaga, Yoshiyuki Yamashita, Shigenori Ueda, and Keisuke Kobayashi
Appl. Phys. Lett., 97, 252113 (2010)

11. *Electronic transport properties of electron- and hole-doped semiconducting C_{1b} Heusler compounds: $NiTi_{1-x}M_xSn$ (M=Sc, V)*

Siham Ouardi, Gerhard H. Fecher, Benjamin Balke, Xenia Kozina, Gregory Stryganyuk, Claudia Felser, Stephan Lowitzer, Diemo Ködderitzsch, Hubert Ebert, and Eiji Ikenaga, Phys. Rev. B, 82, 085108 (2010)

12. *Magnetic circular dichroism in photoelectron emission from partially compensated ferromagnetic $Mn_{3-x}Ga$ thin films*
Xeniya Kozina, Gregory Stryganyuk, Andrei Gloskovskii, Benjamin Balke, Juergen Winterlik, Gerhard H. Fecher, and Claudia Felser
DESY Annual Report (2010)

13. *Preparation of amorphous aluminium oxide thin films by electrophoresis, (in Russian)*
Xeniya Kozina
Proceedings of 60th students and young scientists conference "Youth and science: creative work and innovation", Almaty, April, (2006)

14. *Preparation of thin films from metal alkoxides, (in Russian)*
Xeniya Kozina, Nataliya Korobova
Proceedings of intercollegiate conference "New innovation technologies in Physics", Almaty, May, (2006)

2 Zusammenfassung

Röntgenphotoelektronenspektroskopie (XPS) ist eine der gebräuchlichsten und vielseitigsten Methoden, um die chemischen Zusammensetzung und elektronischen Struktur von Materialien zu bestimmen. Die Anwendung von harten Röntgenstrahlen erhöht die mittlere freie Weglänge der emittierten Elektronen im Festkörper. Somit ist hard X-ray Photoelektronenspektroskopie (HAXPES) eine ideale Methode um Volumeneigenschafen zerstörungsfrei zu bestimmen.

Diese Arbeit fokussiert sich auf die Untersuchung von mehrschichtigen Strukturen, die als Bauelemente in Tunnelkontakten den magnetischen Tunnelwiderstand (TMR) nutzen wobei verschiedene Anwendungen der HAXPES Technik zum Einsatz kommen. Solche Spintronik-Bauelemente sind wichtige Komponenten der Nanotechnik. HAXPES ermöglicht die Untersuchung und das detaillierte Verständnis der Mechanismen und Eigenschaften der verwendeten magnetischen Materialien, bestimmt durch ihre Elektronenstruktur, die für die Leistung dieser Bauelemente bestimmend sind.

Ausführlich wurde die B-Diffusion von auf CoFeB basierenden Tunnelelementen als Funktion der Anlass-Temperatur und die daraus resultierenden Änderungen der elektronischen Struktur der CoFeB Elektroden untersucht, wodurch der hohe TMR-Wert erklärt werden kann. Diese Ergebnisse werden in Kapitel 6 dieser Arbeit erläutert. Die Änderung der Valenzzustände und des TMR von nicht stöchiometrischen $Co_2Mn_\alpha Si$-Elektroden bei Änderung des Mangangehalts α wurden mittels hochauflösender HAXPES untersucht, die Ergebnisse sind in Kapitel 7 dargestellt.

Um magnetoelektrische Eigenschaften wie die Austauschaufspaltung in Ferromagneten näher zu bestimmen, eignet sich die Untersuchung des magnetischen zirkularen Dichroismus (MCDAD) mittels Photoemission. Dabei tritt eine Asymmetrie in den Photoemissions-spektren auf, wenn entweder die Helizität bei fester Magnetisierung der Probe oder die Magnetisierungsrichtung bei fester Helizität verändert wird. Da diese Technik bis jetzt aufgrund niedriger Photonenergien nur zur Untersuchung von Oberflächen zu gebrauchen war, wurde diese Methode in HAXPES Experimente integriert, um einen Zugang zu den magnetischen Eigenschaften von komplexen Multilagensystem zu erlangen. Die Ergebnisse der MCDAD Messungen an CoFe und an vergrabenen Tunnelkontakten aus halbmetallischen Ferromagneten Co_2FeAl mittels hochenergetischer Röntgenstrahlung sind in Kapitel 8 dargestellt.

Obwohl die magnetoresistiven Eigenschaften von Spintronik-Bauelementen durch den Spin der Elektronen der ferromagnetischen Materialien festgelegt sind, waren direkte Messungen der Spinpolarisation bis jetzt aufgrund der Oberflächensensitivität der klassischen Photoemission eingeschränkt. In Kapitel 9 werden die ersten Ergebnisse von spinaufgelösten HAXPES Experimenten an magnetischen Schichtsystemen aus $Co_2FeAl_{0.5}Si_{0.5}$ mittels eines SPLEED Spin-Polarimeters präsentiert. Die Messungen belegen eine 50 % Spin-Polarisation der Photoelektronen der durch eine 3 nm dicke Oxiddeckschicht emittierten Photoelektronen aus Fe $2p_{3/2}$ Zuständen. Damit ist gezeigt, dass die Methode des Spin-HAXPES für die magnetische Charakterisierung von vergrabenen Schichten und inneren Grenzschichten möglich ist. Dies eröffnet für die Zukunft eine neue Klasse von Experimenten.

3 Abstract

X-ray photoemission spectroscopy (XPS) is one of the most universal and powerful tools for investigation of chemical states and electronic structures of materials. The application of hard x-rays increases the inelastic mean free path of the emitted electrons within the solid and thus makes hard x-ray photoelectron spectroscopy (HAXPES) a bulk sensitive probe for solid state research and especially a very effective nondestructive technique to study buried layers.
This thesis focuses on the investigation of multilayer structures, used in magnetic tunnel junctions (MTJs), by a number of techniques applying HAXPES. MTJs are the most important components of novel nanoscale devices employed in spintronics.
The investigation and deep understanding of the mechanisms responsible for the high performance of such devices and properties of employed magnetic materials that are, in turn, defined by their electronic structure becomes feasible applying HAXPES. Thus the process of B diffusion in CoFeB-based MTJs was investigated with respect to the annealing temperature and its influence on the changes in the electronic structure of CoFeB electrodes that clarify the behaviour and huge TMR ratio values obtained in such devices. These results are presented in chapter 6. The results of investigation of the changes in the valence states of buried off-stoichiometric Co_2MnSi electrodes were investigated with respect to the Mn content α and its influence on the observed TMR ratio are described in chapter 7.

Magnetoelectronic properties such as exchange splitting in ferromagnetic materials as well as the macroscopic magnetic ordering can be studied by magnetic circular dichroism in photoemission (MCDAD). It is characterized by the appearance of an asymmetry in the photoemission spectra taken either from the magnetized sample with the reversal of the photon helicity or by reversal of magnetization direction of the sample when the photon helicity direction is fixed. Though recently it has been widely applied for the characterization of surfaces using low energy photons, the bulk properties have stayed inaccessible. Therefore in this work this method was integrated to HAXPES to provide an access to exploration of magnetic phenomena in the buried layers of the complex multilayer structures. Chapter 8 contains the results of the MCDAD measurements employing hard x-rays for exploration of magnetic properties of the common CoFe-based band-ferromagnets as well as half-metallic ferromagnet Co_2FeAl-based MTJs.

Inasmuch as the magnetoresistive characteristics in spintronic devices are fully defined by the electron spins of ferromagnetic materials their direct measurements always attracted much attention but up to date have been limited by the surface sensitivity of the developed techniques. Chapter 9 presents the results on the successfully performed spin-resolved HAXPES experiment using a spin polarimeter of the SPLEED-type on a buried $Co_2FeAl_{0.5}Si_{0.5}$ magnetic layer. The measurements prove that a spin polarization of about 50 % is retained during the transmission of the photoelectrons emitted from the Fe $2p_{3/2}$ state through a 3-nm-thick oxide capping layer.

Contents

4 Introduction and the basic principles

4.1 Spintronics

While the traditional electronics utilizes only the charge degree of freedom of an electron by controlling its movement in electric field, the spin degree of freedom is completely disregarded. Thus the common microelectronic circuits, that save and express information in the binary number system, employ two possible states of the existence and the absence of electric charge as "0" and "1" bits. For the last decades the high electronics demand, described well by the Moor's law, has lead to the huge increase of the data storage capacity along with the shrinking of the size of the circuits components packed on Si chips. Approaching the physical limits of such technologies, the eager of engineers of the whole world to obtain devices even of much higher performance attracted attention to employment of the quantum properties of an electron such as spin. The spin, being quantized, allows to distinguish electrons of the two sorts "spin-up" and "spin-down" with respect to a chosen quantization axis (which is usually adopted from the magnetization direction). Moreover correspondence of the spin to the magnetic moment of an electron provides the feasibility of its controlling by an externally applied magnetic field as it is already developed in the conventional electronics. Hence these two inherent states of an electron can be efficiently used in the frames of the same binary system defining "0" and "1" in the new logic operation. The further benefits of spin contain its long relaxation time and less energy and time required for a single spin-flip process induced by an external magnetic field than for a displacement of an electron charge. Communication between such devices or their constituent elements additionally to the charge currents is realized by the spin currents that is a momentum transfer across the structure. The newly emerged field of engineering that employs electron spins and named as spinelectronics (or simply spintronics) opens a wide range of possible improvements on the way of elaboration of new non-volatile miniature high-performance devices with high data processing speeds, increased storage capacity and low energy consumption.

4.1.1 Giant magnetoresistance

The new technologies allowing to produce nanometer-scale layers available at that time lead in 1986 to the discovery of the giant magnetoresistance effect (GMR) by Peter

Gruñberg and Albert Fert [1, 2]. This new effect significantly surpassed already known magnetoresistance effects, that gave an impetus to the development of information technologies and brought a Nobel Prize to these two eminent scientist in 2007. It is noteworthy that in a GMR device being comprised of alternating ferromagnetic layers separated by antiferromagnetic ones (as it is shown in Figure 4.1(a), (b)) the resistance can differ to some orders of magnitude. First of all it depends on the thickness of the antiferromagnetic layer and what is more remarkable it can be switched by an externally applied magnetic field. The fact is, that in such structures the exchange coupling mechanism between contiguous ferromagnetic layers comes into play. If the thickness of the spacer layer is comparable with the coherence length of an electron in the given material the coupling is ferromagnetic (the two ferromagnetic layers are magnetized parallel) then the electron having a given spin direction reaches the interface between the antiferromagnetic spacer layer and the next ferromagnetic layer with high probability to penetrate as its spin direction matches the magnetization of the next layer. This leads to the low resistance of the stack (Figure 4.1(a)). In the case of antiferromagnetic coupling when two adjacent ferromagnetic layers are magnetized antiparallel and the flowing electrons are scattered the resistance is getting much higher (Figure 4.1(b)). The magnetoresistance (MR) in general is defined as

$$\frac{\Delta R}{R} = \frac{R_{ap} - R_p}{R_p} \tag{4.1}$$

where R_{ap} stands for the resistance in the case of antiparallel magnetization of the layers, and R_p stands for the parallel one. This is so-called optimistic definition that gives unlimited values of the maximal magnetoresistance. The larger GMR effect is observed when the bias voltage is applied perpendicular to interfaces therefore providing the current to flow perpendicular to the planes (CPP-configuration) than in the case when the current is parallel to the planes (CIP-configuration). At the time of its discovery a GMR of around 80% at 4K was achieved in Fe/Cr multilayers giving the name "giant" to the observed MR [2].

Nowadays the commercial devices in the read out heads of hard disc drives are built on the above described principle of operation and comprised of spin valves based on GMR. Basically, spin-valves are a simple trilayer structures of two ferromagnetic layers separated by a thin non-magnetic layer, though of course it can be buried in a complex multilayer stack. One of these ferromagnetic layers is "pinned" by a antiferromagnetic layer. Both are in contact to each other. The antiferromagnetic layer provides its fixed magnetization direction disregarding the applied magnetic field. The second ferromagnetic layer is "free" and therefore it is sensitive a relatively small values of the applied magnetic field (see Figure 4.1(c)). Thus the spin-valve can exist in two stable states.

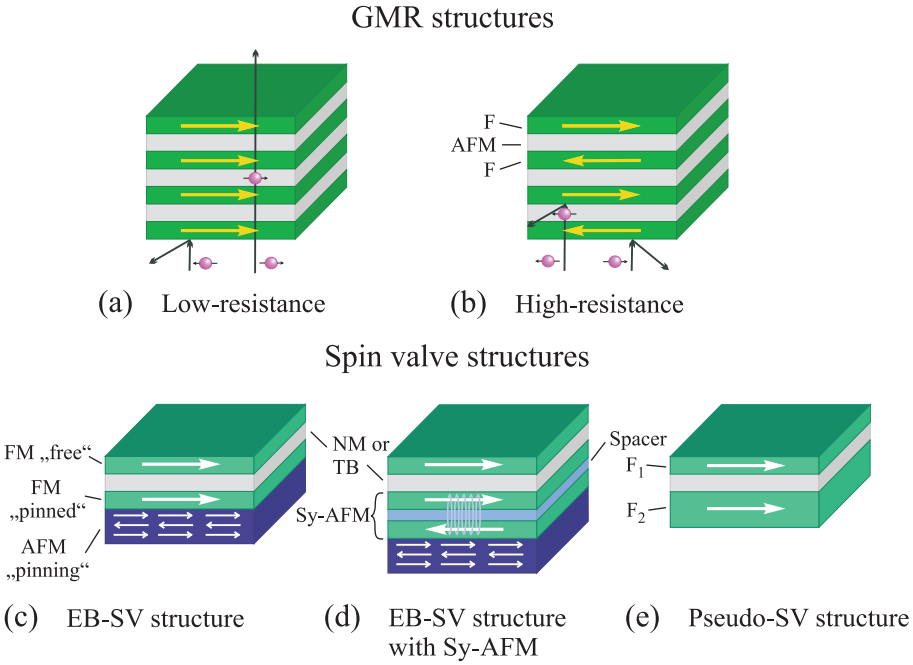

Figure 4.1: Schematic representation of the typical GMR multilayers, comprised of alternating ferromagnetic (F) and antiferromagnetic (AFM) layers, in its low-resistance state when the neighboring FM layers magnetizations are aligned parallel (a) and the high-resistance state in (b) with antiparallel magnetization directions. (c) represents an exchange-biased spin-valve (EB-SV) structure with a pinning AFM layer. An EB-SV structure with pinned synthetic AFM (Sy-AFM) layer constructed from two FM layers coupled antiferromagnetically through a thing spacer layer is illustrated in (d). (e) shows a pseudo-spin-valve (pseudo-SV) structure. The SV-structures (c), (d) and (e) are also typical in the case of MTJs when the non-magnetic layer is replaced by an insulating one.

One is that with the parallel orientation of the ferromagnetic electrodes magnetizations, defined as the low-resistance state or the "open"-state. Another one with the antiparallel magnetizations is defined as the high-resistance state or the "closed"-state. When the spin-valve is used in a sensor mode the magnetization of one ferromagnetic layer turns continuously with respect to that one of another ferromagnetic layer involving the change of the resistance. Thus playing a role of a magnetic sensor this structure is employed in the hard disk drive read/write heads. This brought a wide success to spintronic technologies permitting the storage of tens of gigabytes of data on the notebooks computer drives. The resistance of a spin-valve is typically 5-10% when the magnetization is switched from the parallel to the antiparallel configurations [3].

Lately, on the way of increase of MR ratios, the single "pinned" layer was substituted by a so-called synthetic antiferromagnetic layer that consists of two ferromagnetic layers sandwiching a non-magnetic conducting layer as demonstrated in Figure 4.1(d). Commonly a 1-nm-thick Ru layer spacer is used for this purpose allowing to reach a GMR of 20% in the commercially produced devices [4]. These two structures described above are also very often called exchange biased spin-valve structures (EB-SV structures).

In contrast to the exchange biased spin-valves, a pseudo spin-valve structure employs two ferromagnetic layers separated by a non-magnetic spacer layer without any antiferromagnetic "pinning" layer (Figure 4.1(e)). Different coercitivities of these two ferromagnetic layers lead to their switching in the different values of the applied magnetic fields. To obtain the difference in coercitivity values either materials with different magnetic properties are used as the electrodes or the electrodes of the same material but different thicknesses are employed.

4.1.2 Tunnel magnetoresistance. Coherent tunneling

Further developments in spinelectronics concerned the replacement of the non-magnetic conducting layer separating two ferromagnetic electrodes in spin-valve structure by a non-magnetic insulating layer. The thickness of this thin insulating layer is about 1-2 nm that in such a multilayer stack plays the role of a potential barrier for the electrons current.

As it is well know, an electron can be assigned by a wave function and according to quantum mechanics the electron wave function can penetrate inside the potential barrier where it has an exponential decay and has a non-zero probability for existence behind the barrier [5]. Since the existence of the current in such structures is based on the tunneling effect of electrons these structures were called magnetic tunnel junctions (MTJs).

First observed by Julliere in 1975 for the Fe-Ge-Co junctions, the MR was found to depend on the relative magnetizations of the two ferromagnetic electrodes when the

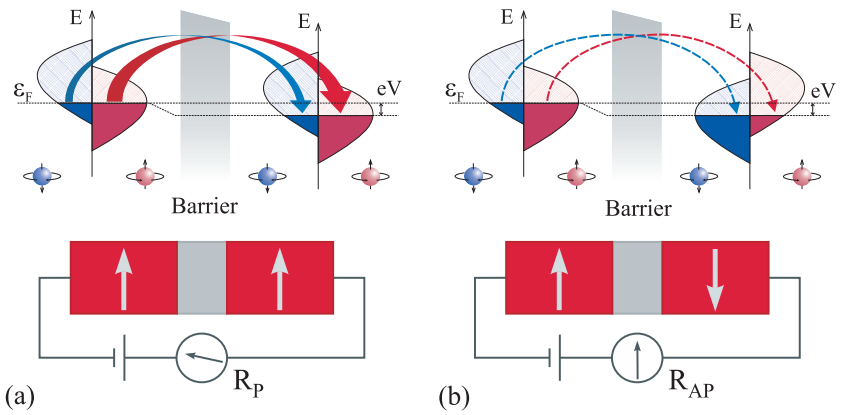

Figure 4.2: Schematic illustration of the TMR effect an a MTJ. (a) denotes the low-resistance (or "open") state of an MTJ with the parallel orientation of the electrodes magnetizations while (b) shows the high-resistance (or "closed") state of the MTJ. The upper panels explain the tunneling process from the spin-resolved density of states point of view.

bias voltage is applied in the CPP geometry likewise in the GMR-based spin-valves [6]. Thus the resistance for antiparallel orientation of the magnetizations is much higher than that for the parallel one (Figure 4.2(a) and (b)). Significant improvements in vacuum deposition techniques lead to the first large TMR values of up to 70% at room temperature (RT) obtained by Miyazaki and Moodera for the Al_2O_3 barrier [7, 8]. Although Al_2O_3 barriers are the mostly used ones their incorporation into the MTJs is rather limited from both the applications point of view and the point of view of obtained TMR values. Thermal instability of such aluminium-oxide barriers reveals the unwanted sensitivity of such MTJs to the technological processing that involves high temperature treatment that makes it difficult to incorporate such stacks into commercially produced devices. Furthermore, the absence of any crystallinity of such barriers leads to a quite large number of imperfections at the FM/barrier interfaces that provokes a diffusive scattering of the electrons mixing all electronic states with the same energy and all this leads to uncertainty in the theoretical predictions of TMR ratios.

A first theoretical model describing TMR effects was introduced by Julliere [6]. In this model he related the TMR ratio to the spin-polarization of the electrodes as follows:

$$TMR = \frac{2P_1P_2}{1+P_1P_2} \tag{4.2}$$

Here P_i is defined as:

$$P_i = \frac{D_{i\uparrow} - D_{i\downarrow}}{D_{i\uparrow} + D_{i\downarrow}} \tag{4.3}$$

D_i stands for the density of states (DOS) at the ϵ_F of the given electrode for majority and minority bands.

Most often this model is used for the estimation of the spin polarization for experimentally obtained TMR ratios. Unfortunately these values sometimes do not correspond, often even in sign [9, 10], to the values obtained experimentally by different techniques such as direct measurements of spin current using superconducting contacts. Thus for systems as Fe/MgO/Fe or CoFe/MgO/CoFe, with the very high TMR ratios of 180% and 220% respectively, the Julliere model gives a value of about 85% (for CoFe) that is inconsistent with spin-polarization values calculated from the bulk DOS of this compound [11, 12, 13]. Therefore, it follows that this model is relevant in giving a so-called effective spin polarization that is the spin polarization specifically of the states with high tunneling probability. This discrepancy originates from the fact that Julliere's model implies that all states of ferromagnetic electrodes have equal tunneling probabilities. Hence it fits well only for description of incoherent tunneling that is, in general, not appropriate even for the amorphous Al_2O_3 barriers [14].

As the tunneling in MTJs is mostly defined by the states that fulfill the criterium of $k_\parallel$ conservation, especially in the case of the thick barriers from quantum mechanical point of view, the considering of the band structures at electrode/barrier interface is highly desirable. As it was shown by Butler and Mathon the huge TMR ratios even higher than 1000% can be reached in fully epitaxial MTJs based on MgO barriers [15, 16]. Thus at the Fermi energy in Fe(001) there are Bloch states with different symmetries at $k_\parallel = 0$: Δ_1, a double degenerated Δ_5 and $\Delta_{2'}$ states for majority channel and Δ_5, $\Delta_{2'}$ and Δ_2 for minority one. The huge tunneling probability in such junctions depends on the unique complex band structure of MgO(001) [17] and its good matching to the free propagating states of the electrode in the following way. The Bloch states with Δ_1 symmetry decay as evanescent states of the same symmetry of MgO. The Δ_5 states of Fe decay as Δ_5 ones in MgO. The Fe states with $\Delta_{2'}$ and Δ_2 symmetries inherent for both majority and minority channels decay as evanescent states of Δ_2 and $\Delta_{2'}$ symmetries of MgO, where such a swap in the symmetry is simply caused by the rotation of the MgO unit cell by $\pi/4$ relatively to that of Fe (Figure 4.3(a)). The second factor influencing the high TMR is the difference in attenuation rate of the states with different symmetries. Δ_1 states have the slowest decay among all the others leading to the dominant tunneling of electrons in these states through the barrier. Moreover Δ_1 states are present only in the majority channel and therefore bring their full spin polarization in the dominant tunneling current that conditions the huge values of TMR

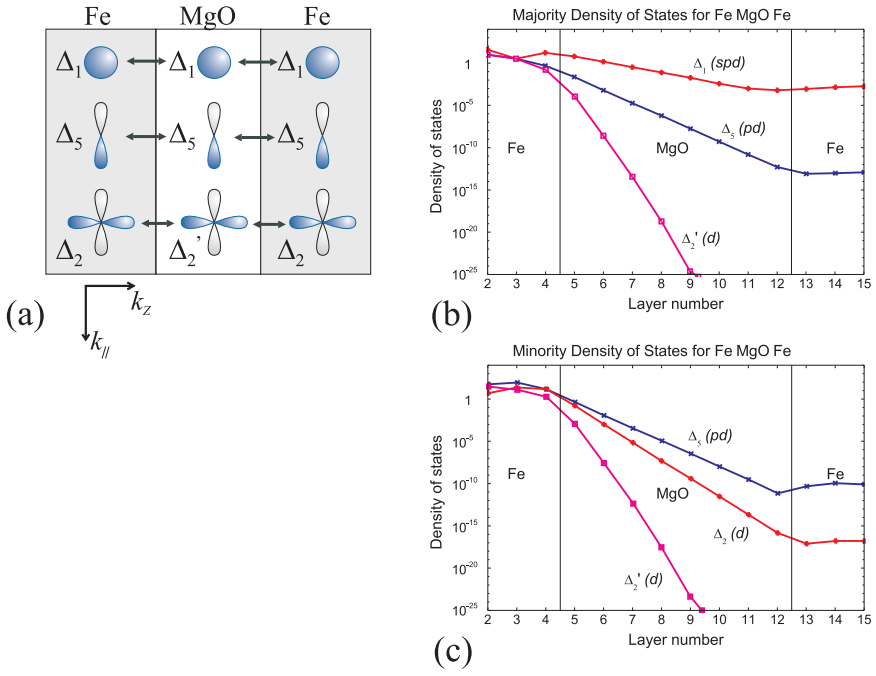

Figure 4.3: Schematic illustration of the coupling mechanism in a fully epitaxial MTJ with single-crystalline MgO barrier in (a). The Bloch states of Fe couple with the evanescent states of MgO for the $k_{||} = 0$ direction (adopted from [14]). (b) shows the tunneling DOS of different symmetries inherent for majority channel and (c) represents the tunneling DOS of different symmetries inherent for minority channel for $k_{||} = 0$ in Fe—MgO—Fe stack in the case of parallel alignment of electrodes magnetizations.

(Figure 4.3(b), (c)). It is noteworthy to say that a lot of other *bcc*-type ferromagnetic materials besides Fe have full spin polarized states with Δ_1 symmetry. This opens a wide range of possible improvements in MTJs by utilizing different materials.

4.1.3 Half-metallic ferromagnets

As it is known the higher TMR ratios and therefore the performance of spintronic devices is conditioned basically by two factors such as high spin polarization of the materials used as electrodes in MTJs and the quality of epitaxial layers and interfaces. Consequently active effort of the researches and engineers of spintronics is taken in two ways either in improvements of produced devices or in developing new materials with higher spin polarization.

Besides the variety of ferromagnetic materials employed in MTJs and showing good results in spin-dependent tunneling the most remarkable are that ones called half-metallic ferromagnets (HMFs). In a common ferromagnet spin-up and spin-down den-

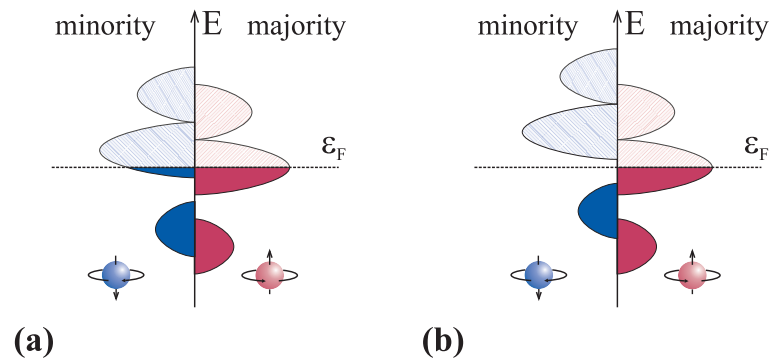

Figure 4.4: Schematic representation of the DOS of a common ferromagnetic material (a) and a half-metallic ferromagnet (b).

sities of states are shifted with respect to each other producing the difference between spin-up and spin-down populations of electronic states that gives rise to a net magnetic moment in the material (See Figure 4.4(a)). The difference in spin-up and spin-down DOS at the ϵ_F results in the finite spin polarization of a ferromagnetic material. In contrast to this in a half-metallic ferromagnet only the states of one spin-direction are occupied at the ϵ_F while for another spin-direction there is a band gap at the ϵ_F as it is shown in Figure 4.4(b). Therefore such a material reveals itself as a metal for one spin-direction and as an insulator for the other. Hence a 100%-spin-polarization of HMFs makes them ideal materials for spintronic applications.

Among the variety of HMFs, Co_2-based Heusler compounds are the most promising candidates. Discovered in 1903 by F. Heusler [18, 19] they still are taken in much interest. Theoretical prediction of their half-metallicity by Kübler for Co_2MnSn in 1983 provoked an enormous activity in the worldwide research aiming at employment of Heusler HMFs in MTJs [20]. A remarkable result was achieved for Co_2MnSi-based MTJs with a Al_2O_3 barrier where a TMR ratio of up to 600% at 4K and 70% at RT was reported by Sakuraba *et.al.* [21].

4.2 Photoelectron spectroscopy

Initially observed by Heinrich Hertz in 1887 [22] photo-induced emission of electrons was found out to be incompatible with the classical Maxwell's wave theory and later in 1905 was described by the quantum nature of light and the dependency of its energy on its frequency. For this work Einstein was honored the Nobel Prize in 1921. Further developments of experimental techniques and the improved theoretical understanding of the materials structure have lead to a wide range of studies feasible by employing the photoelectric effect.

The investigation of the electronic structure of materials is the key point in understanding of their properties, defined by the electronic subsystem. A variety of information can be obtained from the photoelectron spectra and their analysis makes photoelectron spectroscopy (PES) the most convenient and powerful technique for probing electrons in the matter.

In the common PES experiment a specimen is being exposed to radiation with particular energy hν and the photoemitted electrons are being analyzed by their kinetic energies according to the following expression:

$$E_{kin} = h\nu - \phi - |E_{bin}|, \tag{4.4}$$

where E_{kin} is the kinetic energy of an emitted electron, ϕ is the work function and $|E_{bin}|$ is the binding energy [23].

Figure 4.5 schematically illustrates the energy diagram of the photoemission process. An electronic structure of the given sample is represented, in general, by the inner-shell states (or "core-levels") and the valence band that is formed by the delocalized electrons. Followed by the absorption of the incoming photon, an electron is ejected into vacuum to the level separated from the initial one by hν and is in turn detected by the energy analyzer. As it is seen, this diagram corresponds to the solid sample where ϵ_F is the highest occupied level, and it is separated from the vacuum level by the work function. If spectrometer and specimen are in thermodynamic equilibrium the Fermi levels of them are equal. Then the kinetic energy can be written as:

$$E_{kin} = h\nu - E_{bin}^{F} - \phi_{sp}, \tag{4.5}$$

where E_{bin}^{F} stands for the binding energy of the emitted electron with respect to the Fermi level and ϕ_{sp} is the spectrometer work function.

The work function of a sample determines the low energy cutoff of the secondary electrons (the minimal kinetic energy allowing electrons to leave the sample) and therefore determines the "zero" in the energy scale of the measured spectrum. $\phi_s > \phi_{sp}$ and thus can be measured by the spectrometer at a certain kinetic energy (with respect to the vacuum level of the analyzer). The high-energy cutoff is formed by the electrons ejected from the occupied states at the Fermi energy. The difference of these two values gives the work function of the specimen ϕ_s. Since ϕ_s can be easily affected by changes of the surface composition, one often determines the location of ϵ_F by using a reference metallic sample (usually Au) which is in electrical contact with the sample of interest and the spectrometer [24]. This is one of the reasons why the PES experiments require

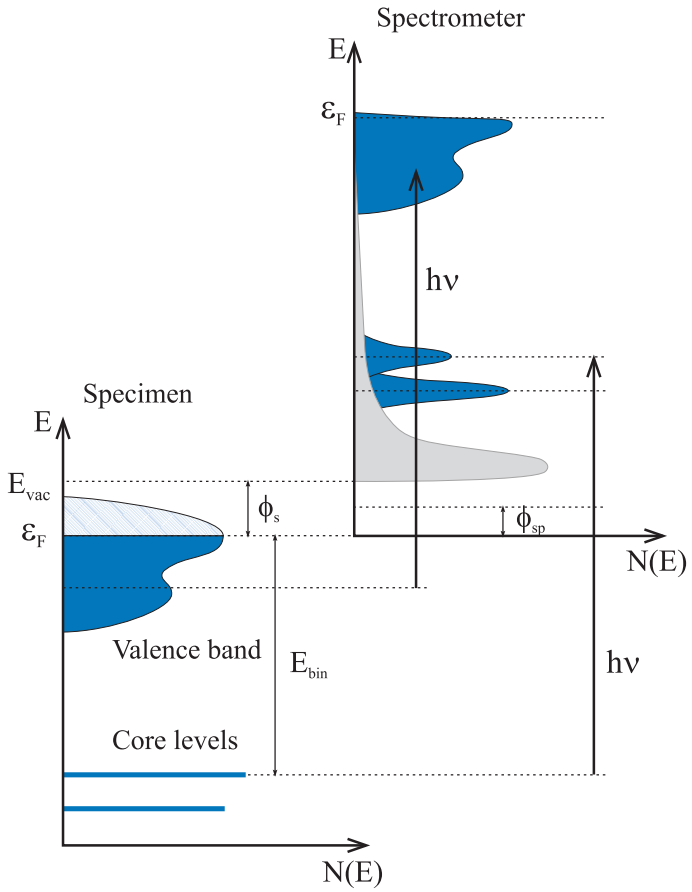

Figure 4.5: Energy diagram demonstrating the relation between the energy levels in a solid specimen (left) and spectrum obtained by the anergy analyzer in a photoemission experiment (right).

ultra high vacuum (UHV) conditions.

4.2.1 Inelastic mean free path. Hard x-ray photoelectron spectroscopy

Another reason why a PES experiment requires UHV conditions is related to the *electron mean free path* (IMFP) in matter. While an exited electron is traveling to the surface of a solid sample, it is undergoing elastic or inelastic scattering events. These processes can occur once or multiple times (due to electron-electron or electron-phonon interactions) before the electron leaves the surface leading to the formation of the secondary electron background in the PES spectra. These are particularly the final-state electrons that can be detected in a PES experiment.

The IMFP of the final-state electrons, defining the probing depth, is rather short and depends on the electron's kinetic energy. For a variety of materials the energy dependent IMFP curve follows the same trend and therefore is known as the "universal

curve" as is shown in Figure 4.6. Here the calculations of the IMFP for 41 elemental solids are shown in the energy range from 50 eV to 30 keV [25]. The minima of all the curves lie in between 10 eV and 100 eV giving a IMFP value of roughly a few $\AA$. This implies that using common laboratory sources for the excitation such as gas-discharge lamps or x-ray tubes makes common photoemission spectroscopy a very surface sensitive method. Therefore UHV conditions are highly desirable providing the necessary cleanness of the surface. Qualitatively the form of the inelastic tail and the background in an XPS spectrum can provide some information of the probing depth from which the signal is obtained. The low intensity of the inelastic tail gives a hint for the surface location of the atom emitting the detected electrons while a high intensity of the inelastic tail of the peak, in contrast, should originate from the bulk [26].

As the electron-phonon scattering is relevant only at very low energies in most cases it can be neglected. With this assumption the IMFP is determined by the electron-electron interaction with the crossection of scattering defined as [23]:

$$\frac{d^2\sigma}{d\Omega d\omega} = \frac{\hbar^2}{(\pi e a_0)^2}\frac{1}{q^2} Im\{-\frac{1}{\varepsilon(\mathbf{q},\omega)}\}, \tag{4.6}$$

where $\hbar\mathbf{q}$ is the momentum transfer, ω is the energy transfer in the scattering process, a_0=0.529 $\AA$ (Bohr radius), and Ω is the solid angle into which the electrons are scattered. The inverse of the average mean free path λ^{-1} is derived by integration over all energy transfers (ω) and momentum transfers ($\hbar\mathbf{q}$). As λ^{-1} is mostly determined by the dielectric function $\varepsilon(\mathbf{q},\omega)$ which is material specific, the IMFP is a particular characteristic of each material. The intensity from a certain emission depth z will decay as

$$dI \propto exp(-z/\lambda cos\theta)dz, \tag{4.7}$$

where θ is the angle of detection with respect to the surface normal. The probing depth (defined as the depth where the signal dropped to $\frac{1}{e}$) is derived as:

$$\Delta = \lambda cos\theta \tag{4.8}$$

and consequently only in the "normal emission" geometry (θ=0) $\Delta = \lambda$=IMFP [23]. Tanuma and co-workers [25] calculated the IMFP dependence with respect to the kinetic energy applying the TPP-2M formula:

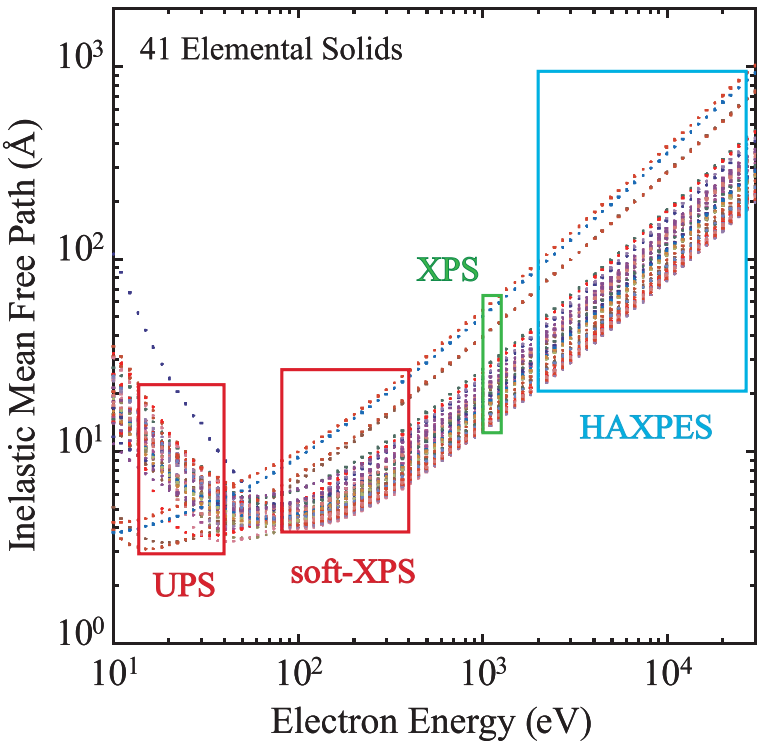

Figure 4.6: Calculated IMFP for 41 elemental solids as a function of electron kinetic energy. Adopted from [25].

$$\lambda \quad = \quad E/\{E_p^2[\beta ln(\gamma E) - (C/E) + (D/E^2)]\}, \tag{4.9}$$

where besides already mentioned parameters $E_p = 28.8(N_V\rho/M)^{1/2}$ stands for the free electron plasmon energy, ρ is density, N_V is number of valence electrons for element or compound, M is the atomic or molecular weight, E_g is the band gap energy for the case of insulators and the values for the parameters are $\beta = -0.10 + 0.944/(E_p^2 + E_g^2)^{1/2} + 0.069\rho^{0.1}$, $\gamma = 0.191\rho^{-1/2}$, $C = 1.97 - 0.91U$, $D = 53.4 - 20.8U$, $U = N_V\rho/M = E_p^2/829.4$.

The curve shows a decrease at energies below the minimum (roughly 20 eV) and a very pronounced increase while going to the energies of keVs. This makes a suggestion to go beyond the common XPS regime into the multi-keV range of the excitation energies that will allow PES to be a bulk sensitive technique. Thus for the case of Au, λ can be estimated to be about 8 nm (at E_{kin}=10 keV) that is 5.7 times larger than that at E_{kin}=1 keV [25]. The feasibility of the very high information depth reached by hard x-ray photoelectron spectroscopy (HAXPES) was demonstrated by a clear observation of the Si 1*s* signal from a SiO_2 layer buried under 15 nm of NiGe in

the structure Si(substr.)/SiO_2(12 nm)/NiGe(15 nm) and moreover the substrate signal from underneath of 27 nm overlayer was still detectable at 8 keV excitation energy [27].

HAXPES suffers from the considerable reduction of the photoionization crossections with increase of the kinetic energies. The decreasing rate for the different subshells is not equal. Thus the photoionization crossection for s-states decreases much slower compared to that of p, d and f states. While analyzing the experimentally obtained spectra by means of comparison with the calculated DOS or with the spectra obtained at different excitation energies one should take care of the quite different partial contributions from various states in the spectrum. This changes significantly the shape of the spectrum, especially in the valence band region.

The decrease in the intensity caused by the reduction of photoionization cross sections at high energies can be overcome by utilizing synchrotron radiation. The world-wide interest in HAXPES has appeared in recent years due to elaboration and availability of 3rd generation synchrotrons that fulfil the number of experimental conditions desirable for performing PES experiments with hard x-rays. Employment of undulators delivering an extremely high photon flux (more than 10^{11} photons/sec) along with a high flux density with a bandwidth of about 1 eV was followed by an improvement of the analytical hardware. The stable, low-noise, high-energy-compatible electron spectrometers, adapted to the beam spot size and grazing incidence geometry, in the combination with a well monochromatized beam obtained by using channel-cut Si single crystal monochromators allowed to provide high energy resolution, high photoelectron yield experimental conditions. As it was recently demonstrated the energy resolution of about 60 meV can be achieved at 8 keV excitation energy [27]. All this together makes HAXPES a unique tool for non-destructive, element-specific exploration of the electronic structure of buried layers and interfaces in nano-scale devices such as MTJs that are of a great technological interest and are in the focus of the present investigation.

4.3 Magnetic dichroism in the angular distribution of photoelectrons (MDAD)

As it is known the DOS of a ferromagnetic material is characterized by the different number of occupied electron states for two opposite spin directions. This results in the net magnetic moment or a spontaneous magnetization in the ground state. The direction of the sample magnetization $\overrightarrow{M}$ defines the quantization axis. In ferromagnets the spin-splitting appears not only in the electronic states close to the Fermi energy ϵ_F but also as a feature of photoelectrons ejected from the core levels, as it was demonstrated by the spin-resolved core level spectroscopy [28].

Consider the photoionization as an only one-electron process for the case of Fe $2p$

subshell where the spin-orbit splitting is much larger being compared with the exchange splitting as demonstrated in Figure 4.7. The initial state is characterized by the closed subshell while in the final state as a result of electron photoexcitation a core-hole is produced. Due to the exchange interaction of this core-hole with the spin polarized valence band of a ferromagnet its state will be energetically split into components defined by the projection m_j. It was shown that such consideration can be described by the same equations as that one taking into account a photoionization of initially polarized one-electron subshell with the same orbital and total angular momenta [29].

Application of the circularly polarized light leads to selective excitation of electrons with a given spin direction as the dipole transitions from m_j sublevels are defined by $\Delta m = \pm 1$ selection rules for the right and left circularly polarized light respectively. The circularly polarized light helicity defines another quantization axis during the excitation along with the first one defined by the sample magnetization $\overrightarrow{M}$. These two axes define the optical orientation of the photoemission experiment on ferromagnetic materials that has a dichroic nature. Therefore the effect observed in such an experiment is called magnetic circular dichroism in photoemission.

Baumgarten et al. [30] carried out a pioneering study on magnetic dichroism in photoemission and observed this phenomenon in the core-level spectra of transition metals. The effect, however, was rather small (few %) because of the limited resolution of the experiment. It was later shown that dichroic effects are also obtained using linearly or even unpolarized photons [31, 32]. The observed intensity differences in photoemission are essentially a phenomenon specific to angular-resolved measurements, and therefore, these have been termed as magnetic circular dichroism in the angular distribution (MCDAD) [33, 34, 35].

Theoretical atomic single-particle models were quite successful in describing, explaining, and predicting many aspects of magnetic dichroism. Cherepkov et al. elaborated the general formalism for the dichroism in photoemission excited by circularly, linearly, and unpolarized radiation [33]. They showed that MCDAD is very sensitive to the geometry of the experiment and depends strongly on the relative orientation between the sample magnetization $\overrightarrow{M}$, photons helicity σ, and momentum of the excited electrons $\overrightarrow{k}$. The maximum effect is obtained when the magnetization and helicity vectors are parallel; the effect decreases with an increase in the angle between these vectors. The grazing incidence geometry provides the largest value of the photon spin projection onto the sample magnetization $\overrightarrow{M}$.

The dipole transition probability in MCDAD experiment depends on the azimuthal quantum number m_j. Thus for the left-circularly polarized light it increases with m_j for $2p_{3/2}$ levels and decreases for the right-circularly polarized one. The magneto-dichroic signal is defined in general by the intensity asymmetry $A = \frac{(I^+ - I^-)}{(I^+ + I^-)}$ calculated from the intensities obtained by the one of the quantization axes reversal. In other words

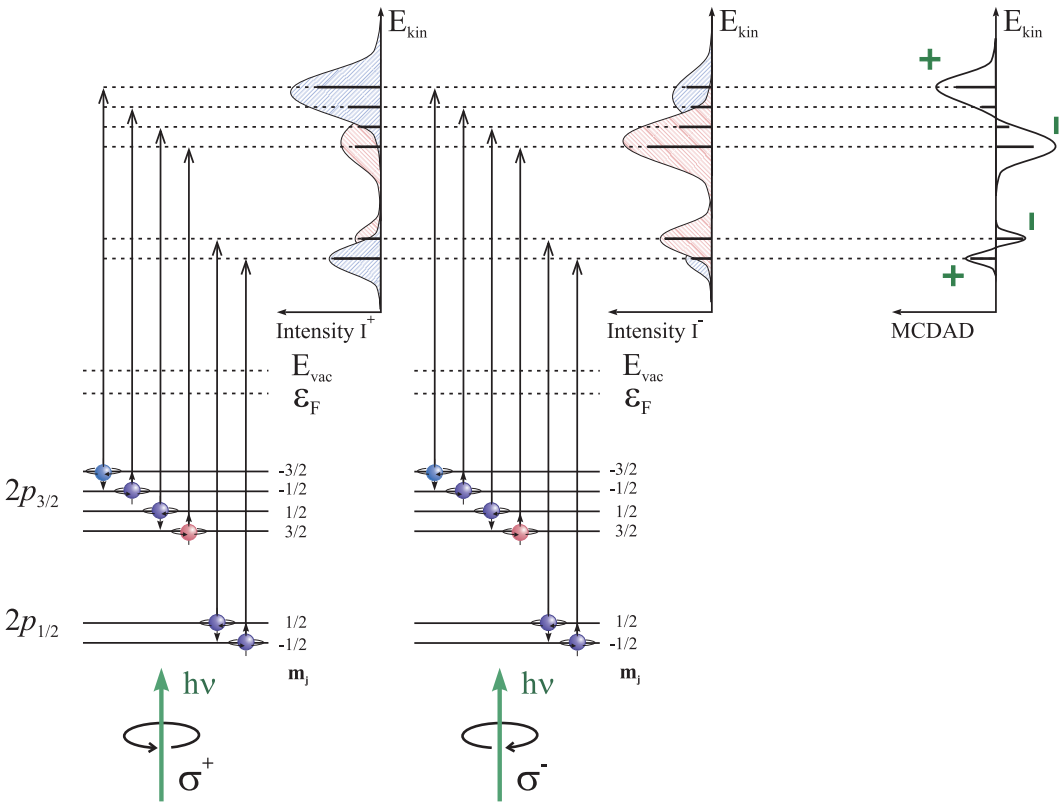

Figure 4.7: The schematic representation of the magnetic circular dichroism effect for Fe $2p$ states. Asymmetry obtained by the reversal of photon spin direction. The pure spin states are marked for $m_j = \pm 3/2$ sublevels.

either the light helicity (σ^+, σ^-) or magnetization of the sample (M^+, M^-) is reversed leading to the different values of observed intensities (I^+, I^-) and ($I(M^+)$, $I(M^-)$) respectively. This originate the formation of +/- feature for $2p_{1/2}$ and -/+ one for $2p_{3/2}$ levels as the spin-orbit interaction reverses the sequence of m_j levels corresponding to $2p_{3/2}$ states compared to $2p_{1/2}$ states. Magnetic dichroism may be defined in a similar manner using the differences in the intensities if the direction of the magnetization $\overrightarrow{M}$ is changed keeping the polarization of the photons fixed. As the m_j values are defined with respect to the first quantization axis $\overrightarrow{M}$, its direction reversal causes the energy positions of m_j levels to be swapped over with that ones of -m_j levels leading to the similar shape of the asymmetry curve as for the case of helicity axis reversal [36].

It is worthwhile to say that in contrast to the spin-resolved photoemission measurements the energy splitting obtained in MCDAD spectra cannot be directly referred to the exchange splitting. For the case of Fe $2p$ states within the perturbational approach, when the spin-orbit coupling is much larger than exchange coupling, the latter hybridizes the $2p_{1/2}$ and $2p_{3/2}$ wave functions. As a consequence of this the spin polarization expectation values along $\overrightarrow{M}$ vary for the different m_j sublevels. Only the states with $m_j = \pm 3/2$ can be considered as pure spin states as it is marked in the Figure 4.7. In the case of Fe $3p$ shallow core states, where spin-orbit splitting is comparable with exchange splitting and the latter cannot treated as a perturbation, none of the m_j states appear to be pure spin states [36].

The electronic states in solids usually do not carry a spherical or axial symmetry as in free atoms but have to follow the symmetry of the crystal [37]. The angular distribution $I^j(\mathbf{k}, \mathbf{n})$ of the photoemitted electrons - as derived for example in Reference [33] for the case of axially symmetric polarized atoms - has to account for the non- diagonal density matrix $\rho^{\mathbf{n}}_{NM'_N}$ [38]. This leads to the following equation for the case of a non-axial symmetry:

$$\begin{aligned} I^j(\mathbf{k},\mathbf{n}) &= \frac{c_\sigma}{[l]}\sqrt{\frac{3\,[j]}{4\pi}}\sum_{\kappa,L}\sum_{N}[N]^{1/2}\,C^j_{\kappa LN}\sum_{x,M}\sum_{M_N,M'_N}\rho^\gamma_{\kappa x}\rho^{\mathbf{n}}_{NM'_N}(j)Y^*_{LM}(\mathbf{k}) \\ &\quad\times D^N_{M_N M'_N}(\Omega)\begin{pmatrix} \kappa & L & N \\ x & M & M_N \end{pmatrix} \end{aligned} \tag{4.10}$$

l and j are the orbital and the total angular momentum of an electron in the initial state. $C^j_{\kappa LN}$ are the dynamic parameters derived from the radial matrix elements and $\rho^\gamma_{\kappa x}$ are photon state multipoles [38]. $D^j_{mm_j}(\Omega)$ is the Wigner rotation matrix with Ω being the set of Euler angles describing the rotation from the laboratory to the atomic coordinate frame. The direction of the electron momentum $\overrightarrow{k} = \mathbf{k}(\theta, \phi)$ is defined by the angles θ and ϕ (see Figure 4.8). Finally, c_σ is a photon-energy ($h\nu$) dependent

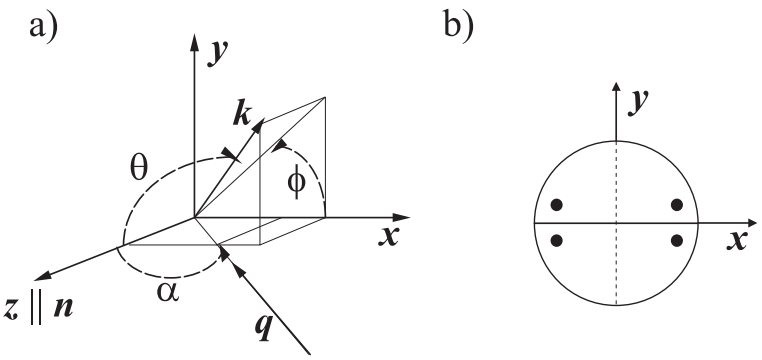

Figure 4.8: (a) The coordinate system used for the investigation of photoemission. $\mathbf{k}(\theta, \phi)$ is the electron momentum, $\mathbf{q}$ is the photon beam and $\mathbf{n}$ is the principal axis of alignment. θ and ϕ are the angles defining the direction of the outgoing photoelectrons. α is the angle of photon incidence (in the XZ plane) as defined in optics. It is seen that the angle describing the photon propagation in spherical coordinates is given by $\Theta_q = \alpha + \pi$. The direction of the z axis corresponds to the quantization axis $\mathbf{n}$. (b) The direction of the in-plane axes x and y is illustrated for an object with C_{2v} symmetry.

constant: $c_\sigma = \frac{4\pi^2 \alpha\ h\nu}{3}$ where α is the fine structure constant.

This formalism can also be used to consider open shell atoms and the multiplets resulting from the interaction between the core states and the open shell valence states. In that case, the dynamic parameters $C^j_{J\kappa LN}$ have to be calculated for the appropriate coupling scheme (jj, LSJ, or intermediate) with the single particle quantum numbers j, m being replaced by those (J, M) describing the complete atomic state [33]. In that case, the dynamic parameter will redistribute the single-electron results in a particular way over the states of a multiplet (see References [39, 40, 41, 42, 43]).

The state multipoles of the s, p, and d-states that define the intensity and the sign and magnitude of the dichroism are summarized in Tables 4.1 and 4.2. Note that the state multipoles are independent of the orbital angular momentum L, they depend only on the total angular momentum J and its projection M_J.

Table 4.1: State multipoles of $|L, J\rangle = |0, 1/2\rangle$, $|1, 1/2\rangle$, $|1, 3/2\rangle$, and $|2, 3/2\rangle$ states.

J	$\frac{1}{2}$		$\frac{3}{2}$			
M_J	$+\frac{1}{2}$	$-\frac{1}{2}$	$+\frac{3}{2}$	$+\frac{1}{2}$	$-\frac{1}{2}$	$-\frac{3}{2}$
ρ_{00}	$\frac{1}{\sqrt{2}}$	$\frac{1}{\sqrt{2}}$	$\frac{1}{2}$	$\frac{1}{2}$	$\frac{1}{2}$	$\frac{1}{2}$
ρ_{10}	$\frac{1}{\sqrt{2}}$	$-\frac{1}{\sqrt{2}}$	$\frac{3}{2\sqrt{5}}$	$\frac{1}{2\sqrt{5}}$	$-\frac{1}{2\sqrt{5}}$	$-\frac{3}{2\sqrt{5}}$
ρ_{20}	-	-	$\frac{1}{2}$	$-\frac{1}{2}$	$-\frac{1}{2}$	$\frac{1}{2}$
ρ_{30}	-	-	$\frac{1}{2\sqrt{5}}$	$-\frac{3}{2\sqrt{5}}$	$\frac{3}{2\sqrt{5}}$	$-\frac{1}{2\sqrt{5}}$

Table 4.2: State multipoles of $|L, J\rangle = |2, 5/2\rangle$ states.

J	$\frac{5}{2}$					
M_J	$-\frac{5}{2}$	$-\frac{3}{2}$	$-\frac{1}{2}$	$+\frac{1}{2}$	$+\frac{3}{2}$	$+\frac{5}{2}$
ρ_{00}	$\frac{1}{\sqrt{6}}$	$\frac{1}{\sqrt{6}}$	$\frac{1}{\sqrt{6}}$	$\frac{1}{\sqrt{6}}$	$\frac{1}{\sqrt{6}}$	$\frac{1}{\sqrt{6}}$
ρ_{10}	$-\frac{5}{\sqrt{70}}$	$-\frac{3}{\sqrt{70}}$	$-\frac{1}{\sqrt{70}}$	$\frac{1}{\sqrt{70}}$	$\frac{3}{\sqrt{70}}$	$\frac{5}{\sqrt{70}}$
ρ_{20}	$\frac{5}{2\sqrt{21}}$	$-\frac{1}{2\sqrt{21}}$	$-\frac{2}{\sqrt{21}}$	$-\frac{2}{\sqrt{21}}$	$-\frac{1}{2\sqrt{21}}$	$\frac{5}{2\sqrt{21}}$
ρ_{30}	$-\frac{5}{6\sqrt{5}}$	$\frac{7}{6\sqrt{5}}$	$\frac{2}{3\sqrt{5}}$	$-\frac{2}{3\sqrt{5}}$	$-\frac{7}{6\sqrt{5}}$	$\frac{5}{6\sqrt{5}}$
ρ_{40}	$\frac{1}{2\sqrt{7}}$	$-\frac{3}{2\sqrt{7}}$	$\frac{1}{\sqrt{7}}$	$\frac{1}{\sqrt{7}}$	$-\frac{3}{2\sqrt{7}}$	$\frac{1}{2\sqrt{7}}$
ρ_{50}	$-\frac{1}{6\sqrt{7}}$	$\frac{5}{6\sqrt{7}}$	$-\frac{5}{3\sqrt{7}}$	$\frac{5}{3\sqrt{7}}$	$-\frac{5}{6\sqrt{7}}$	$\frac{1}{6\sqrt{7}}$

4.3.1 MDAD equations for the grazing incidence geometry

In the following, let us consider the special case of geometry with the photons impinging in the $x-z$ plane with unit vector of the photon momentum $\hat{q} = (-\cos(\alpha), -\sin(\alpha), 0)$. At such a grazing incidence with $\alpha = \pi/2$ it becomes $\hat{q} = (-1, 0, 0)$. The electrons are observed in the direction perpendicular to the photon beam ($\theta = \frac{\pi}{2} - \alpha$) with the momentum $\hat{k} = (-\sin(\theta), 0, \cos(\theta))$. At a photon incidence of $\alpha = \pi/2$ it becomes $\hat{k} = (0, 0, 1)$. (Compare also Figures 4.8 and 5.2.)

Now examine the case: $\vec{n} \rightarrow -\vec{n}$ where the magnetic dichroism emerges from a switching of the direction of magnetization with the initial direction $\vec{n} = (1, 0, 0)$ that is along the x-axis. Applying Equation (4.10) and the state multipoles of Table 4.1 the circular magnetic dichroism in the angular distribution for p-states is given by the equations:

$$\begin{aligned} CMDAD^{\sigma+}(p) &= -\rho_{10}\sin(\alpha)\left(\sqrt{\tfrac{2}{3}}C^{(1,0,1)}_{JkLN} + \sqrt{\tfrac{1}{15}}C^{(1,2,1)}_{JkLN}(1 - 6\cos^2(\alpha))\right) \\ CMDAD^{\sigma-}(p) &= +\rho_{10}\sin(\alpha)\left(\sqrt{\tfrac{2}{3}}C^{(1,0,1)}_{JkLN} + \sqrt{\tfrac{1}{15}}C^{(1,2,1)}_{JkLN}(1 - 6\cos^2(\alpha))\right) \end{aligned} \tag{4.11}$$

The circular magnetic dichroism in the angular distribution (CMDAD) for opposite helicity of the photons has an opposite sign. The equations for the $p_{1/2}$ and $p_{3/2}$ states are the same. The magnitude differs, however, because of the differences in the state multipoles ρ_{10} and dynamical parameters C_{JkLN}.

For $\alpha = \pi/2$ the $CMDAD$ of the p-states ($J = 1/2, 3/2$) becomes simply:

$$CMDAD^{\sigma\pm}(p_J) = \mp\rho_{10}\left(\sqrt{\frac{2}{3}}C^{(1,0,1)}_{JkLN} + \sqrt{\frac{1}{15}}C^{(1,2,1)}_{JkLN}\right) \tag{4.12}$$

The linear counterpart LMDAD vanishes in that geometry, independent whether the photons are s or p polarized. At $\alpha = \pi/2$ the magnetic dichroism in the angular distribution vanishes for all p-states independent of the polarization of the photons if

the magnetization is perpendicular to the plane spanned by the photon incidence and the electron momentum (here for the x-z plane with $\vec{n}= (0, \pm 1, 0)$).

4.4 Principles of spin-resolved photoelectron spectroscopy

If considering the assumption that in a photoemission process the incoming photon couples directly only with the orbital momentum of the electron but not its spin, the spin should therefore be conserved during the excitation. Hence the spin in the initial state can be determined if one could measure the spin of the final-state electrons. This holds as long as spin-orbit interaction at the surface is negligible [44].

The employment of the spin-analysis technique in a HAXPES experiment, as it is sketched in Figure 4.9 is of great interest as it allows to investigate not only a spin-integrated electronic structure but directly probes spin-up and spin-down states with high bulk sensitivity. The measurements of the spin of the photoemitted electrons applied to the valence band region will make it possible to probe directly the exchange-split band structure of magnetic materials as well as their spin-polarization at ϵ_F. If applied to the core levels this technique gives access to the local magnetic information. This makes spin-resolved HAXPES to be undoubtedly a key tool in engineering of novel materials for spintronics applications and investigating the magnetic properties of buried layers and interfaces in a non-destructive way.

In a spin-resolved PES experiment the spin-polarization **P** of an electron beam, particularly its projection onto the quantization axis, is defined as:

$$P = \frac{N^{\uparrow} - N^{\downarrow}}{N^{\uparrow} + N^{\downarrow}}, \tag{4.13}$$

where $N^{\uparrow(\downarrow)}$ is the number of electrons whose spin is parallel or antiparallel to the quantization axis.

In the present work spin-resolved photoelectron are obtained by using a spin-polarized low-energy electron diffraction (SPLEED) polarimeter. The spin sensitivity of this method originates from the spin-orbit coupling. The spin-orbit interaction can be represented as an additional potential term in a non-relativistic approximation [45]:

$$V_{SO} = \frac{1}{2m^2c^2}\frac{1}{r}\frac{dV}{dr}(\mathbf{s}\cdot\mathbf{l}), \tag{4.14}$$

where **s** and **l** are the spin and orbital moment operator respectively.

In general, this leads to the fact that the scattering process of an electron from an atom has a different probability in the two opposite directions. The spin-orbit coupling

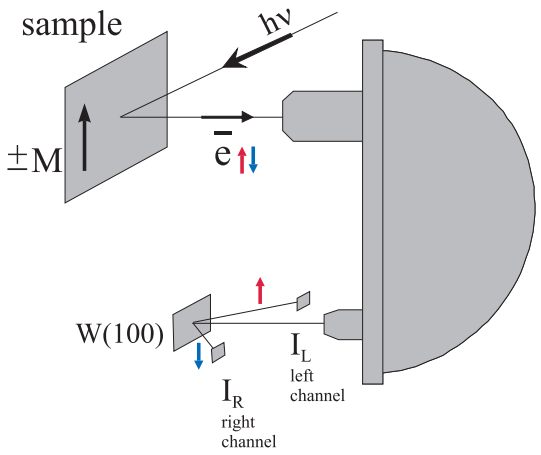

Figure 4.9: Schematic representation of the spin-HAXPES experiment employing a spin-polarimeter of the SPLEED-type integrated into the high-energy analyzer. M± assigns two antiparallel directions of the sample magnetization that are used to account for the instrumental error inevitable in such types of experiments.

term in the crystal Hamiltonian couples the spin of an electron and its orbital angular momentum. Therefore the electron eigenfunctions are not pure spin states any longer but are rather a mixture of spin-up $|\uparrow>$ and spin-down $|\downarrow>$ states. Thus they can be assigned as $|+>$ and $|->$ respectively. These states are not simply related to the experiment as the scattering event occurs on the crystal surface where there is no spatial inversion symmetry. This leads to different probabilities for the transmittance events for the incident electrons with spin-up $|\uparrow>$ and spin-down $|\downarrow>$ states into $|+>$ and $|->$ crystal states. Therefore the reflection and transmission of the incoming electrons at the crystal surface has a spin-dependent character and the intensities of the diffracted electron beams are defined by the spin-polarization of the incident electron beam [46].

The SPLEED detector spin-discrimination system consists of the (001) surface of a tungsten crystal that has a fourfold rotation symmetry about its normal and two mirror-symmetry planes, containing the surface normal. In the SPLEED-type detectors the electron beam impinges on the (001) surface of the analyzer crystal along its normal. If the beam has no spin-polarization (Figure 4.10(a)), then the intensities of the four diffracted beams lying in the mirror planes are equal, $I_1 = I_2 = I_3 = I_4$. If the beam has a finite spin-polarization which is, for instance, perpendicular to one of the mirror planes, then there is only one mirror plane left as **P** is included in the former one (see Figure 4.10(b)). The diffraction maxima lying out of the plane, in which **P** is included (I_3 and I_4), are interchanged and have the same intensity but the other ones (I_1 and I_2) will have different intensities.

The sign of the additional spin-orbit potential V_{SO} is defined by the spin direction of an electron and the direction of its path nearby the nucleus (left-hand or right-hand

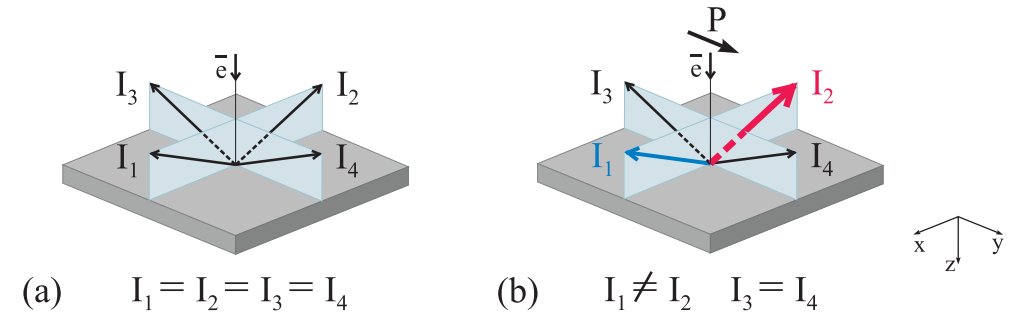

Figure 4.10: Schematic illustration of the geometry in the scattering process at the tungsten crystal surface in the SPLEED detector. (a) presents the case where the impinging electron beam is unpolarized resulting in diffraction maxima with equal intensity. (b) presents the case where the incoming electron beam is polarized in the direction perpendicular to $(z - x)$ plane resulting in non-equal I_1 and I_2 intensities (adopted from [46]).

wise). If we consider the traveling direction of an electron as z axis, its polarization - along the y axis, and its scattering in the $(z - x)$ plane (I_2 beam) then the orbital moment is parallel to the spin and we label the I_2 beam as "left" (L). Respectively, the I_1 beam is labeled as "right" (R). Due to the different differential cross sections for spin-up and spin-down electrons one observes the intensity asymmetry defined as:

$$A = \frac{I_L - I_R}{I_L + I_R}, \tag{4.15}$$

If I_0 is the total intensity of the spin-polarized beam, the completely unpolarized part of a beam with mixed polarization can be written as I_0(1-P) and the completely polarized part as I_0P. Therefore the asymmetry is proportional to the spin-polarization:

$$A = SP, \tag{4.16}$$

where S is the Sherman function [47] defined from the scattering conditions of each particular experiment (geometry, material, surface structure etc.)

Thus the spin-polarization of the incoming beam can be derived from the asymmetry values obtained experimentally. In calculations of the spin-polarization it is worthwhile to take into account the instrumental asymmetry P_{ins} which disappears when the magnetization of the sample is reversed. If we assign I^+ to the intensity of a signal obtained using the M^+ direction of magnetization and I^- to that of the M^- direction one can write:

$$\begin{aligned} P &= P_{real} + P_{ins} \\ P(M+) &= P_{real} + P_{ins} \\ P(M-) &= P_{real} - P_{ins} \\ P(M+) &= -P(M-) \\ A(M+) &= \frac{I_L^+}{I_R^+} \\ A(M-) &= \frac{I_L^-}{I_R^-} \\ A_0^2 &= A(M+)A(M-) \\ \overline{A} &= \sqrt{A_0^2} \\ &= \sqrt{\frac{I_L^+ I_R^-}{I_R^+ I_L^-}}, \end{aligned} \tag{4.17}$$

P_{real} stands here for the real polarization of the electrons leaving a specimen, $P(M+)$ and $P(M-)$ are the total polarizations measured using M^+ and M^- magnetizations of the sample, A^+ and A^- are the measured asymmetries respectively. $\overline{A}$ is the average asymmetry for both magnetization directions and is used in the determination of the spin-polarization from the experiment as:

$$\begin{aligned} P &= \frac{1}{S}\frac{\sqrt{\frac{I_L^+ I_R^-}{I_R^+ I_L^-}} - 1}{\sqrt{\frac{I_L^+ I_R^-}{I_R^+ I_L^-}} + 1} \\ &= \frac{1}{S}\frac{\sqrt{I_L^+ I_R^-} - \sqrt{I_R^+ I_L^-}}{\sqrt{I_L^+ I_R^-} + \sqrt{I_R^+ I_L^-}}, , \end{aligned} \tag{4.18}$$

Measuring the spin-integrated spectra $\langle I \rangle$ (total for all four reflexes of the (2,0) series) in the photoemission experiment as a function of E_{kin} one can calculate the spin-up and spin-down partial spectra as follows:

$$I^{\uparrow} = \langle I \rangle (1 + P) \tag{4.19}$$

$$I^{\downarrow} = \langle I \rangle (1 - P) \tag{4.20}$$

,

where $\langle I \rangle$ is defined as:

$$\langle I \rangle = \frac{I_L^+ + I_L^- + I_R^+ + I_R^-}{4}, \tag{4.21}$$

The quantity which characterizes the efficiency of a spin polarimeter is the figure of merit, defined as:

$$F = S^2 \frac{[I_L + I_R]}{I_0}, \tag{4.22}$$

For the SPLEED-type detectors the Sherman function was determined as S=-0.27±0.02 and F=$1.6 \cdot 10^{-4}$ for the (2,0) family of reflexes at the optimum working point at a scattering energy of 104.5 eV.

5 Experimental details

5.1 Hard x-ray photoelectron spectroscopy

The investigation of the electronic structure of materials as well as their chemical composition is feasible by X-ray photoelectron spectroscopy (XPS) as it was already discussed in the first chapter. Under laboratory conditions with energies obtained from commonly used Al-K_α (1486.6 eV) and Mg-K_α (1253.6 eV) sources this method is extremely surface sensitive with an electron escape depth in the order of few $\mathring{A}$ only [48]. The development of synchrotron facilities opened the unique opportunity to utilize high-energy radiation for hard X-ray photoelectron spectroscopy (HAXPES) that increases the probing depth by an increase of the inelastic mean free path of the photoemitted electrons.

Synchrotron radiation (SR) is the term designated on electromagnetic radiation which is produced by charged particles (normally electrons, but sometimes positrons as well) moving along a closed orbit with a speed close to the speed of light. Thus a synchrotron is a particle accelerator or storage ring used as a source of light that can be applied to a broad range of experimental purposes. To deflect the electron beam, direct it along the ring path and focus it different types of magnets are used such as bending magnets, quadrupole and sextupole magnets. While quadrupole and sextupole magnets mostly are employed for providing excellent focusing conditions the bending magnets can also serve as a source of synchrotron radiation with a continuous spectrum of energy ranging from infrared to hard x-rays.

Synchrotron radiation is always polarized in the plane of the electrons' orbit, only if emitted in the plane of the synchrotron, and the polarization reaches almost 100%. The invention and further employment of insertion devices such as undulators has lead to a huge increase of the photon flux (of more than 10^{11} photons/sec [27]). Along with the good focusing this allowed to reach the high photon flux density that is delivered onto the sample surface. In an undulator, consisting of multiple permanent magnet sections with the alternating polarity entering electrons are forced to wiggle for multiple times each time producing synchrotron radiation. Due to the interference effect the result is quasi-monochromatic, highly directional and ultra-bright light. In the elliptical type of undulator it is even possible to change and control the type of polarization of the produced light by changing the geometry of the undulator magnets' arrangement.

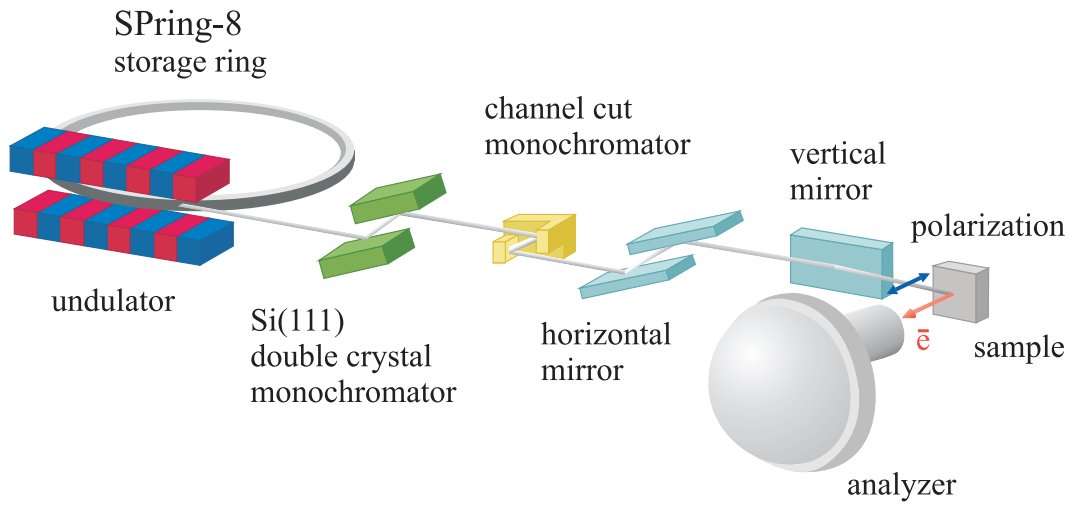

Figure 5.1: Schematic representation of the experimental setup used for HAXPES measurements at BL47XU at SPring-8. Adopted from [27].

Owing to such pronounced advantages the undulators have become the most widely used type of SR source.

The HAXPES experiments described in this work were performed at the SPring-8 synchrotron radiation facility located in Harima Science Garden City, Hyogo, Japan. This is a 3rd generation synchrotron source providing a beam energy of 8 GeV with 100 mA current. SPring-8 opened for the users in 1997 and is up to date the largest and the most powerful light source in the world.

The experiments were based and carried out at the undulator beamlines BL47XU and BL15XU. For the conventional HAXPES studies the photon energy of 3.24 keV at BL15XU, 5.95 keV and 7.94 keV at BL47XU was set. The schematic illustration of the HAXPES experimental setup used at the BL47XU is represented in Figure 5.1. The reduction of the energy bandwidth of the radiation outgoing from the undulator was achieved by using a Si(111) double crystal monochromator. The(444) reflection plane of the Si channel-cut post-monochromator was used for further reduction resulting in 38 meV energy bandwidth. Spot size values of about 30 μm in both vertical and horizontal directions were achieved [27]. At beamline BL15XU, having the similar setup, the photon energy was fixed at 3.24 keV by using (220) reflection plane of the Si channel-cut monochromator following after a Si(111) double crystal monochromator. At both beamlines the high stability of the beam was verified by measurements of the Au $4f$ spectra that is attributed to the remarkable stability of the high-energy spectrometer electronics as well as constant current provided by the top-up operation mode of the synchrotron.

At both beamlines, the photoelectrons were analyzed for their kinetic energy and de-

tected by using hemispherical analyzers (VG Scienta R4000). In such kind of analyzers the photoemitted electrons are collected by a lens system which further retards them to the pass energy and focuses the photoelectron image of the sample onto the entrance plane of the analyzer. In the radial electrostatic field the electrons are dispersed by their energy passing through the concentric hemispheres with difference in applied voltages. The energy dispersion is achieved due to the dependence of the bending radius of an electron on its kinetic energy. The overall energy resolution (monochromator plus analyzer) was set to about 250 meV and for more precise measurements (as for those in the valence band region) to 150 meV, as verified by spectra of the Au valence band at ϵ_{F}. The angle between the electron spectrometer and photon propagation is fixed at 90°. An angle of incidence of $\alpha = 88°$ was chosen in order to be just below the angle of internal reflection. Angles closer to 90° result in a high surface sensitivity. The large angle of incidence results in a near normal emission detection angle of $\theta = 2°$. Using such a grazing geometry the HAXPES experiment leads to the stretching of the beam spot along the sample surface providing better acceptance of the electrons by the analyzer as its entrance slit is also elongated in the horizontal direction. Thus the vertical spot size on the sample is 30 μm, while in horizontal direction, along the entrance slit of the analyzer, the spot was stretched to approximately 7 mm. The measurements were performed under UHV conditions with a pressure of the order of 10^{-9} mbar in the chamber. The experimental chamber is equipped with a 4-axis manipulator for different temperatures of 20 K and 300 K. The cooling was established by the sample holders attached to a He-flow cryostat.

5.2 Magnetic circular and linear dichroism in photoemission

The measurements of magnetic circular dichroism in the angular distribution of electrons (MCDAD) were performed at BL47XU with an excitation energy of 7.940 keV. As it was already mentioned above the direct beam from the undulator is linearly polarized with $P_p = 0.99$. To perform such experiments one needs to use circularly polarized light. The experiments were carried out using grazing incidence geometry. The detection angle was set to $\theta = 2°$ 5.2 in order to reach the near-normal emission geometry and to ensure that the polarization vector of the circularly polarized photons is nearly parallel (σ^-) or antiparallel (σ^+) to the in-plane magnetization M^+. The sign of the magnetization was varied by mounting samples with opposite directions of magnetization (M^+, M^-).

The magnetized samples were mounted pairwise with opposite magnetization on the same sample holder and can be selected via sample shift. Care was taken that the magnetization directions were antiparallel and that surfaces were parallel to avoid different detection angles. The mounting of the samples at the fixed sample manipulator

was chosen to have up/down as well as left/right pairs as it is shown in the Figure 5.2. This allowed to probe the dichroism by varying both the direction of magnetization and the direction of helicity.

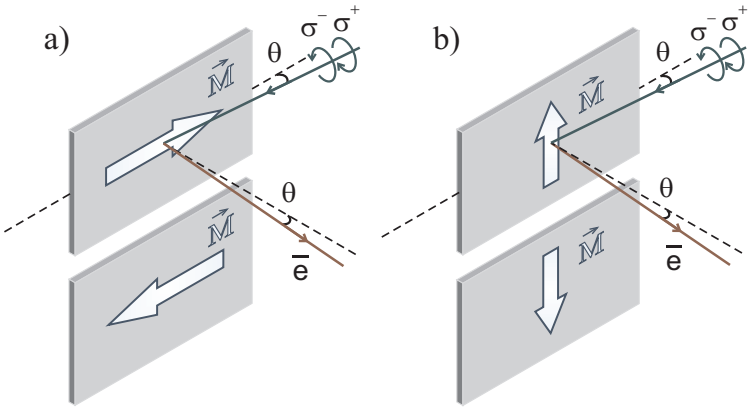

Figure 5.2: Scheme of the experimental geometry.
The incidence angle θ (with respect to the surface plane) of the circularly polarized photons was fixed to 2°. X-rays of opposite helicity (σ^+ and σ^-) were provided by a phase retarder. Further, samples with opposite directions of magnetization are used. In (a) the in-plane magnetization **M** is nearly parallel to the beam axis and in (b) the in-plane magnetization is perpendicular to the beam axis. The electron detection is fixed and perpendicular to the photon beam.

To provide different kinds of possible polarization of the incoming photon beam it was decided to install a polarizer, i.e. an in-vacuum diamond based phase retarder (see Figure 5.3). The thickness of the diamond crystal with (220) orientation [49] is only 600 μm. The phase retarder manipulates the beam polarization by varying the relative phase between the horizontal and vertical field components causing, in general, elliptical polarization and in extreme cases circular and vertical polarization. Light passing through the phase retarder has a very high degree of polarization for both circular and vertical polarizations. One of the disadvantages of using this technique is the loss of 1 order of magnitude in the intensity when light passes through the phase retarder due to the absorption of the diamond crystal. Using the phase retarder, the degree of circular polarization is set such that $P_c > 0.9$ and P_s=0.90 for the linearly s-polarized photons..

The circular dichroism is characterized by an asymmetry that is defined as the ratio of the difference between the intensities I^+ and I^- and their sum:

$$A = \frac{I^+ - I^-}{I^+ + I^-}, \tag{5.1}$$

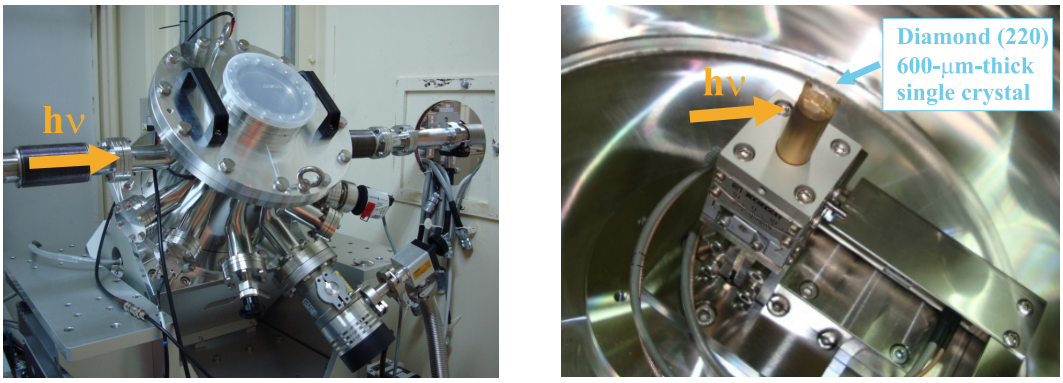

(a) (b)

Figure 5.3: Photos of the diamond-based in-vacuum phase retarder installed at the beamline BL47XU, SPring-8. The general view is presented in (a), (b) shows an enlarged view of the in-vacuum part where the diamond crystal is fixed in the brazed holder. The holder is equipped with a piezo-stage for fine adjustment. The arrows assign the direction of the impinging x-ray beam. (Photos courtesy of Dr. Eiji Ikenaga.)

where I^+ corresponds to σ^+- and I^- to σ^-- type helicity.

The photon flux on the sample was about 10^{11} photons per second in a bandwidth of 10^{-5} during the measurements at the given excitation energy. The resulting count rates (taken from the equivalent gray scale values provided by the spectrometer software) were in the order of 0.6 to 6 MHz for the core level spectra including shallow core levels and about 0.25 MHz for the valence band.

5.3 Spin-resolved hard x-ray photoelectron spectroscopy

The spin-resolved HAXPES experiment has been implemented by a combination of a Scienta R-4000-10keV hemispherical analyzer with an integrated spin detector based on spin polarized LEED at a W(100) surface [50]. For the spin resolved measurements with the SPLEED detector, the photon energy was set to 5.95 keV because of a higher photoelectron intensity expected from the increase of ionization cross section at lower energies. The photon flux at 5.95 keV was $\approx 10^{11}$ photons/s with 50 meV intrinsic bandwidth after a Si channel-cut post-monochromator [27] with (333) reflection plane. The total energy resolution for spin resolved measurements was set to about 1 eV with fixed 2 mm entrance slit of the SPLEED detector and 200 eV pass energy of the analyzer.

The SPLEED detector used in this work serves for measurements of electron spin polarization at kinetic energies of up to 10keV. It is designed as a high-voltage compatible

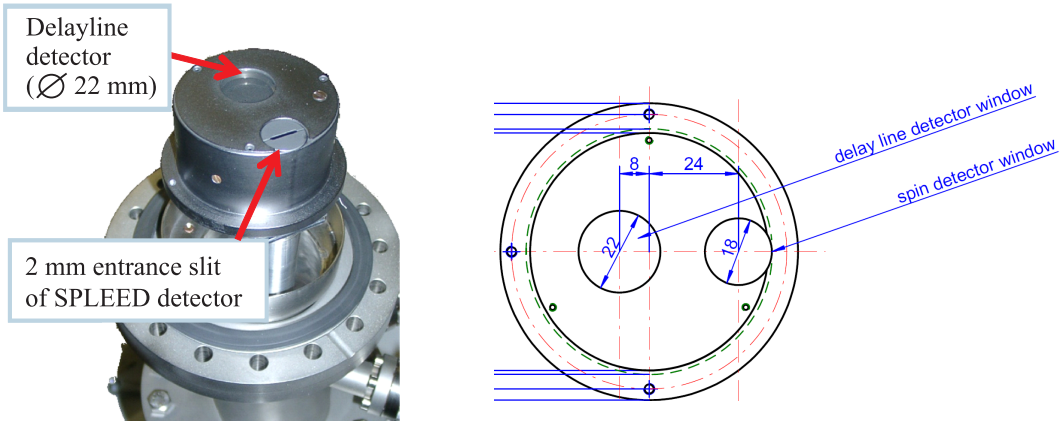

(a) (b)

Figure 5.4: Photo of the entrance plane of the SPLEED detector-DLD assembly (a). The drawing in (b) shows the arrangement of the two detector entrances with respect to the exit port of the Scienta high-energy analyzer.

version of the well-established SPLEED detector adapted to a high-energy electron analyzer (e.g. the Scienta R4000). A delayline detector (DLD) is mounted in the exit plane of the electron analyzer as it is shown on Figure 5.4(a). Such a construction facilitates the alignment procedure and regular measurements with a high detection efficiency parallel to the spin polarization measurements. At the entrance of the transfer optics to the SPLEED detector, the electron beam passes a slit aperture that acts as exit slit of the electron spectrometer (2 mm in dispersive direction, 18 mm in non-dispersive direction). As it is seen from the drawing of this assembly in Figure 5.4(b) the center of the DLD as well as 2-mm-slit of the SPLEED detector are shifted with respect to the center of the analyzer axis. Thus the entrance slit of the SPLEED detector is displaced 24 mm out of the center of the spectrometer exit towards the outer hemisphere and the DLD is displaced 8 mm out of the center of the spectrometer exit towards the inner hemisphere. Taking into account the energy dispersion in the Scienta-analyzer exit port, which is 0.5 eV/mm at the pass energy of 200 eV, one can calculate the energy shift for both detectors that corresponds to +12 and -4 eV for SPLEED detector and DLD respectively.

Figure 5.5(a) shows a cross sectional view of the SPLEED detector. Analyzer chamber, channeltron assembly, and electron-optical transfer system have been designed by Surface Concept GmbH. The lens system consists of 8 tube lens elements, one of which is an x/y deflector unit. The front part of the electron focusing system provides an enhanced transmission with extended acceptance angle of the detector. The back part that is separated from the the front part by a UHV valve is equipped with the spin-discriminating system: a W(100) analyzer crystal with filament heating device located

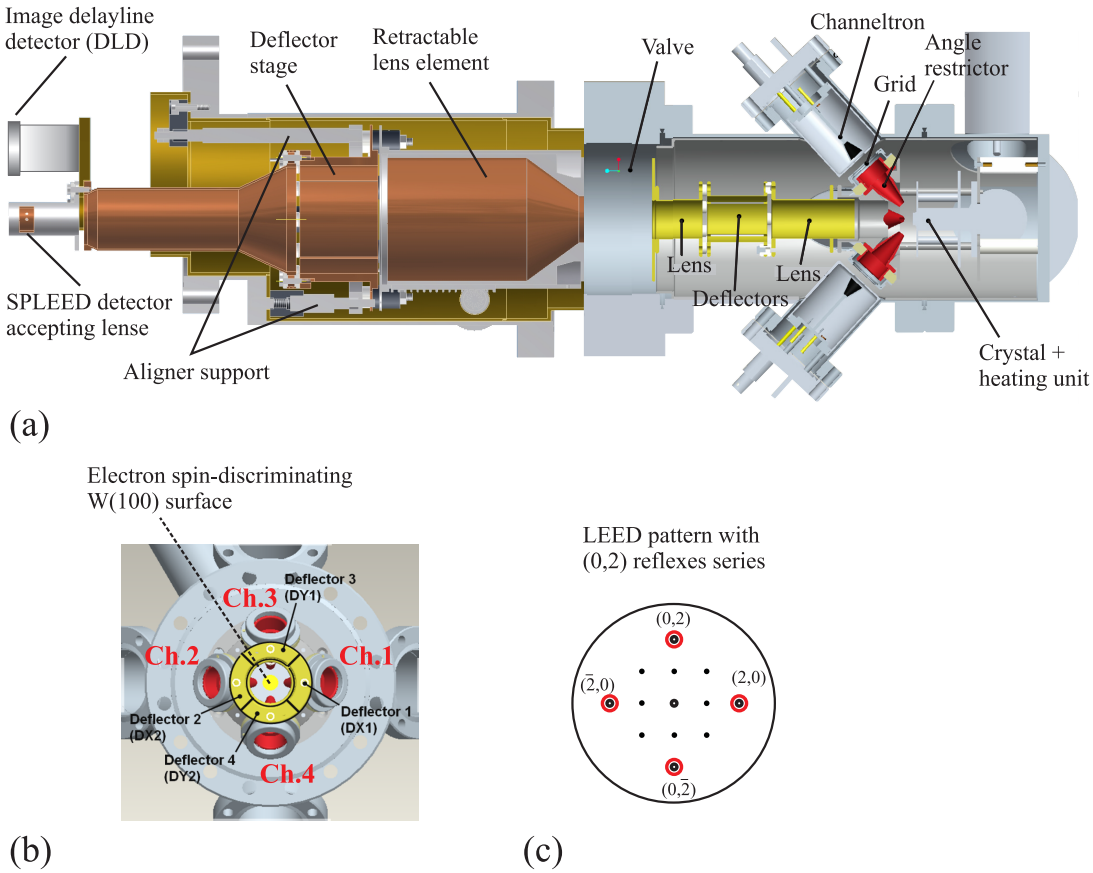

Figure 5.5: Cross sectional view of the high voltage SPLEED detector system combined with the DLD detector (a). (b) represents the front view of the spin-discriminating system and (c) shows the LEED pattern with (2,0) series of reflexes (marked with red circles) detected by channeltrons 1-4.

behind the crystal and four channeltrons for detection of the backscattered electrons in the (2,0) family of reflexes that is shown in Figure 5.5(b) and (c) respectively. The SPLEED detector operates at a scattering energy (i.e. impact energy of the electrons on the analyzer crystal) of nominally 104.5 eV for maximum figure of merit of spin detection [51].

Yu and co-workers demonstrated the time dependence of the Sherman function of the SPLEED-type detector [50]. The main reason of such a time dependence is that the surface of the W(001) crystal is changed in time due to adsorption of residual gas (mostly hydrogen and CO) from the experimental chamber thereby affecting the Sherman function by lowering it with time. Therefore before performing the measurements and during the measurements the spin-discriminating system should be treated. For the surface treatment an oxygen doser is located in the SPLEED detector chamber. It consists of a silver tube heated by an inner thermocoax heater. It allows a precise regulation of high-purity oxygen from ambient air via the temperature of the Ag tube set by the heating current. The preparation of the W(100) single crystal was performed according to the standard procedure, described below. The hot oxygen treatment is carried out under a partial oxygen pressure of $5{\cdot}10^{-8}$ mbar for about 10 sec when the crystal is heated to about 1350 K. This procedure was repeated in cycles for 15 times. Upon this treatment bulk carbon contaminations of the crystal segregate to the surface of the W-crystal and are oxidized and desorbed. After this the system is normally left to cool down for about 30 min. The CO-flash is the procedure when the crystal is heated up to 1500 K for 10 sec. It should be done to remove the CO contaminant from the W(100) surface prior the measurements start. During the oxide flash the W(100) crystal is heated up to 2300 K for about 7 sec in order to remove the oxide that is still left after performing a CO flash from the crystal surface and finally prepare it for the measurements. After oxide-flash the system is left to cool down at least for 10 min before the measurements that is also due to the time-dependence of the Sherman function which is increased in the first 20-min-period after the heat treatment. During this time the tungsten surface undergoes the thermal as well as adsorbate-induced surface reconstruction. The cold oxygen treatment is performed under a partial oxygen pressure of $5{\cdot}10^{-8}$ mbar for 10 min. Adsorbates on the W(100) crystal are oxidized and the crystal is passivated against further contamination with carbon (CO of residual gas). This procedure (without hot oxygen treatment) is done before a long break, in particular, at the end of a day or a beamtime.

6 HAXPES on CoFeB-based magnetic tunnel junctions

6.1 Introduction

Since the discovery of the tunneling magnetoresistive (TMR) effect in 1994 by Miyazaki [7] much interest has been attracted to investigation of this effect in magnetic tunnel junctions (MTJs). The resistance of an MTJ, constructed in general from two ferromagnetic electrodes separated by a thin insulating barrier, is much higher when no field is applied to the MTJ and the magnetization of the two electrodes is antiparallel (R_{ap}) than that when saturating field is applied and the magnetization of the two electrodes is parallel (R_{p}). This phenomenon originates from spin-dependent electron tunneling through a thin insulating barrier and according to the well-known Julliere model [6] the TMR ratio is defined as $(R_{\mathrm{ap}} - R_{\mathrm{p}})/R_{\mathrm{p}}$ which in turn can be explicitly written in terms of left and right electrodes spin-polarizations: $2P_{\mathrm{L}}P_{\mathrm{R}}/(1-P_{\mathrm{L}}P_{\mathrm{R}})$. Switching possibility by an externally applied magnetic field opens a wide range of potential applications of such structures in high performance non-volatile magnetoresistive random access memories (MRAMs) and as magnetic sensors in hard disc drive heads.

Much effort has been made in investigation of MTJs with an amorphous Al_2O_3 barrier [8, 52]. Though the barriers from this material can be easily grown with high degree of homogeneity without any pinholes, the TMR ratios achieved in such MTJs are quite modest (only up to 70% at RT) [52]. Moreover, since the technological production of Si integrated circuits with MTJs requires high temperature treatment, the thermal instability of Al_2O_3 barriers rather limits the range of their applications [53]. In addition, the absence of any epitaxial relationship on the interfaces between the ferromagnetic electrodes and amorphous barrier makes the modeling and calculations of the TMR quite difficult due to the non-conservation of the electron momentum parallel to the barrier ($k_{\parallel}$) [16, 15]. In 2001 Butler and Muthon [16, 15] found out that the symmetry of both the Bloch states in the electrodes and evanescent states in the barrier define the tunneling probability of the electrons. They predicted a giant TMR ratio of 1000% for the epitaxial Fe(001)‖MgO(001)‖Fe(001) stack. Thus when the wave functions of the tunneling electrons in the electrodes have identical symmetry as the states within the barrier, $k_{\parallel}$ is conserved giving rise to the coherent tunneling

mechanism. Particularly it was shown that the Bloch states propagating in the Fe electrodes with $\Delta_1(s+p_z+d_{(2z^2-x^2-y^2)})$, $\Delta_5(p_x+p_y+d_{(xy)}+d_{(yz)})$, $\Delta_{2'}(d_{xy}+d_{y^2-z^2})$ and Δ_2 ($d_{x^2-y^2}$) symmetries couple well with the evanescent states of Δ_1, Δ_5, Δ_2 and $\Delta_{2'}$ symmetry, respectively, existing in the MgO barrier, and have a different decay rate within the barrier. Moreover, the states of Δ_1 symmetry, present at ε_F only in the majority channel, and therefore are completely spinpolarized, have the slowest decay rate causing giant values of the TMR ratio [16, 15]. Following this approach, even larger values were predicted for epitaxial Co and Fe based MTJs [54]. Realization of such huge TMR ratios as a goal and compatibility of MgO barriers with high temperature treatment inherent for technological processing, particularly for further applications in MRAM, provoked intense studies of MTJs with single-crystalline MgO barriers.

Experimentally a TMR ratio of 220% at RT for CoFe/MgO/CoFeB with a polycrystalline CoFe electrode and amorphous CoFeB was demonstrated by Parkin in 2004 [13]. Even larger TMR ratio of 230% was successfully reached at RT for a spin-valve type MTJ with amorphous CoFeB layers. As a noteworthy result here it was demonstrated that the crystallinity of the MgO layer is being improved when grown from an amorphous CoFeB electrode rather than from polycrystalline CoFe. Consequently the sharpness of the interface is being improved as well. These factors make experimentally fabricated structures closer to fully epitaxial ones described in theory by fulfilling the conditions for coherent tunneling and therefore giving rise to the obtained large TMR ratios.

As it is known, CoFeB layers are always amorphous in the as-deposited state. Further heat treatment is essential on the way to improvement of the quality of such MTJs. Formation of an epitaxial *bcc* (001) texture of the CoFeB electrode, along with the electronic structure of its interface with the MgO barrier, during the annealing process is responsible for the reduction of conductance in such MTJs [55]. The crystallization process during annealing was extensively studied by several groups. Thus the deposition of an additional Ru layer underneath the CoFeB layer (MTJ with synthetic ferrimagnetic pinned layer) initiates the crystallization of CoFeB from MgO (001), forming a (001)-oriented *bcc* structure, and not from the CoFe layer underlying the CoFeB electrode that leads to the formation of a (110) texture when the Ru spacer is absent. Besides this, the Ru spacer plays a key role as barrier that suppresses the diffusion of Mn from the pinning antiferromagnetic layer through all overlaying layers into the MgO barrier that undoubtedly is one of the reasons for the drop of the TMR at temperatures higher than 325°C. Hence, TMR ratios up to 361% at RT can be achieved after annealing at 425°C and using a Ru spacer with an optimal thickness of 2.5 nm [56]. Introducing a pseudo-spin-valve structure that does not contain a pinning AFM layer can solve the problem of Mn and Ru atoms diffusion at high temperatures into the MgO barrier as it was shown by Hayakawa and co-workers [57]. As a result a TMR ratio of

472% at RT was achieved after annealing at 450°C, that virtually was not possible for exchange-biased spin-valves even though the sharpness of the CoFeB/MgO interface was significantly improved under high annealing temperatures.

The chemical composition as well as the thickness of the CoFeB electrode notably effects the measured TMR ratios in MTJs. During annealing CoFeB is preferably crystallized from the adjacent MgO layer into the well ordered *bcc* (001) texture when Fe is prevailed in its composition, while a Co-rich electrode tends to form an fcc texture lowering TMR [57]. This is related to the CoFeB/MgO interface energy in the case of a Co-rich composition that reduces the nucleation rate leading to nonuniform crystallization. Using Fe-rich electrodes annealed at 475°C allowed to reach TMR ratios of up to 500% at RT in MTJs with optimized thickness of the bottom electrode of 4.3 nm [58].

The thickness of the bottom electrode in such junctions comes into play at temperatures higher than 475°C when diffusion of Ta atoms affects the crystallinity of CoFeB electrodes. Therefore increasing of the bottom electrode thickness can suppress Ta diffusion providing further increase of TMR ratios with increasing of annealing temperature. As it was demonstrated by Ikeda [59] that even higher TMR ratios can be achieved when going to even higher temperatures of annealing (>500°C) if taking into account the larger thickness of the bottom electrode that was optimized to the value of 6 nm and served as a reliable barrier against Ta diffusion.

These effects of improvement of the MgO crystallinity, sharpness of the interface and crystallization of the CoFeB electrodes can only partially explain the behaviour of the TMR ratio with increasing annealing temperature: its gradual increase up to about 520°C and the sudden drop at higher temperatures. Perhaps one of the major roles is played by the B content, its impact to a TMR ratio dependence and the process of B diffusion with increase of annealing temperature. Considering the influence of B on the spin-dependent conductance in MTJs, Burton and co-workers [60] reported that B atoms likely remain at the interface weakening the bonds of Fe and Co atoms with O atoms of the MgO barrier. Hence the conductance through states of Δ_1 symmetry is lowered leading to a reduction of TMR values. On the one hand several papers claimed that increasing the annealing temperature initiates the penetration of B atoms from the interface region of the CoFeB electrode into the MgO barrier [61, 62, 63], though a higher O concentration in the lower electrode (particularly already in the as-deposited sample) suggests that the results can be influenced by the destructive depth profiling using Ar^+ bombardment or can be related to the production method of a particular MTJ [64]. On the other hand it was evidently shown that B mostly diffuses to the adjacent Ta layer that afterwards blocks its diffusion with increase of annealing temperature. Reduction of B content in the electrode, and particularly in the vicinity of the interface region, reduces the CoFeB crystallization temperature inducing the

crystallization of the electrode from its interface with MgO in well ordered *bcc* (001) texture causing the growth of the TMR ratio.

X-ray photoemission spectroscopy (XPS) is one of the most universal and powerful tools for investigation of chemical states and the electronic structure of materials. Utilizing hard X-rays increases the inelastic mean free path of the electrons within the solid and thus makes XPS a bulk sensitive probe for solid state research (see [27] and references there) and especially a nondestructive technique to study buried layers [65]. The present study is devoted to a nondestructive analysis of the chemical composition of annealed CoFeB tunnel junctions using high resolution hard X-ray photoelectron spectroscopy (HAXPES). The aim is to explore the role of the B content in the magnetic electrodes and B diffusion for the observed improvement of the TMR with increasing annealing temperature.

6.2 Details of calculations

Self-consistent band structure calculations of the electronic and magnetic properties of $Co_xFe_yB_z$ with fixed Fe : Co ratio ($x/y = 3 : 1$) and decreasing B content from $Fe_{0.6}Co_{0.2}B_{0.2}$ to $Fe_{0.75}Co_{0.25}$ were carried out by means of the spin polarized (SP) fully relativistic (R) Korringa-Kohn-Rostoker Green's function formalism (SPR-KKR package [66] as implemented in the Munich-SPRKKR program which allows to describe the random chemical disorder very efficiently within the so-called coherent potential approximation [67, 68] to account for the random distribution of the atoms on the sites of the lattice. The exchange-correlation was treated using the local density approximation within the Vosko-Wilk-Nussair form [69]. A base, $26 \times 26 \times 26$ mesh was used for integration. The mesh corresponds to a minimum of 1470 (out of 19200) k-points in the irreducible wedge of the Brillouin zone. The size of the muffin-tin radii was set automatically to result in space-filling spheres. f-states ($l = 3$) were included in the basis of all atoms.

FeCo appears in the form of random as well as ordered alloys. To capture the most essential features caused by chemical disorder the properties of $Co_xFe_yB_z$ were calculated in $Im\overline{3}m$ (completely disordered $A2$ structure), $Pm\overline{3}m$ (partially ordered $B2$ structure) and $Fm-3m$ (completely ordered DO_3 structure) symmetries (space group numbers: 229, 221 and 225 respectively) using a fixed lattice parameter of $a = 2.8645$ Å.

For the random alloy with $A2$ structure all atoms are equirandomly mixed over the whole lattice occupying the 2a Wyckoff position of the body centered cubic lattice with weights corresponding to the occupation numbers x, y, and z. In this case the structure is described by the following chemical composition formula: $[Fe_{3(2-x)/4}Co_{(2-x)/4}B_x]$ where the brackets mean a single atomic site. The $B2$ structure allows to account for the partial ordering which is suspected from the analysis of the present photoemission data. This type of the ordered alloy was simulated by putting Fe on the 1a Wyckoff position of the simple cubic lattice and - according to the composition - Co, B, and the remaining Fe on 1b that corresponds to $[Fe_{1-x}B_x][Fe_{(2+x)/4}Co_{(2-x)/4}]$ composition. The ordered DO_3 structure was realized by simulation of the face-centered cubic lattice where Fe atoms were situated in 4a and 8c Wyckoff positions while 4b tetrahedral sites were occupied by the Fe and Co atoms in the ratio 1 : 1 according the the composition formula Fe_3Co.

6.3 Samples description

For the present study, special multicomponent thin film arrangements were produced that correspond to half as well as full tunnel junctions as used in TMR devices (see [59]). The fabricated samples with half tunnel junction layer structure were as follows: ther-

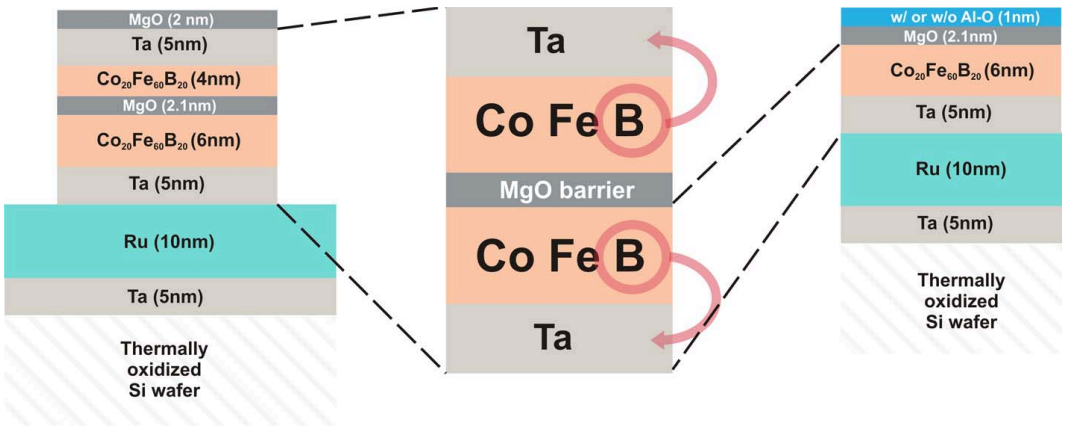

Figure 6.1: Sketch of the CoFeB-based films structure used for the photoemission experiments.
The layer structure corresponded to the lower part of a tunnel junction (I) is represented on the left. The full MTJ structure (II) is on the right. An additional AlO_x layer was used to protect the hygroscopic MgO layer for part of the samples.

mally oxidized Si wafer as substrate / Ru (10 nm) / Ta (5 nm) / $Fe_{60}Co_{20}B_{20}$ (6 nm) / MgO barrier (2.1 nm). Part of the samples was produced with a 20 nm thick MgO layer to estimate the influence of the MgO valence states on the valence band spectra of the underlying FeCoB layer. The samples corresponding to full tunnel junctions had the structure: SiO wafer / Ru (10 nm) / Ta (5 nm) / $Fe_{60}Co_{20}B_{20}$ (6 nm) / MgO barrier (2.1 nm) / $Fe_{60}Co_{20}B_{20}$ (6 nm) / Ta (5 nm) / Ru (10 nm) / MgO cap (2.1 nm) or slightly modified SiO wafer / Ru (10 nm) / Ta (5 nm) / $Fe_{60}Co_{20}B_{20}$ (6 nm) / MgO barrier (2.1 nm) / $Fe_{60}Co_{20}B_{20}$ (6 nm) / Ta (5 nm) / MgO cap (2.1 nm). The latter, without the top Ru layer, were used for comparison because of the low electron mean free path in Ru (see below). Further, parts of the samples were covered by 1 nm AlO_x as protective cap to prevent degradation of the MgO layer during transport through air. The structures of the layer stacks are shown in Figure 6.1. The conditions of MTJ fabrication and TMR measurement have been described elsewhere [56, 58, 59, 70]. The film structures were investigated by X-ray diffraction and high resolution transmission electron microscopy with energy dispersive X-ray spectroscopy. For similar junctions as used here, a TMR ratio of 604% at 300 K was found for junctions annealed to 798 K [59].

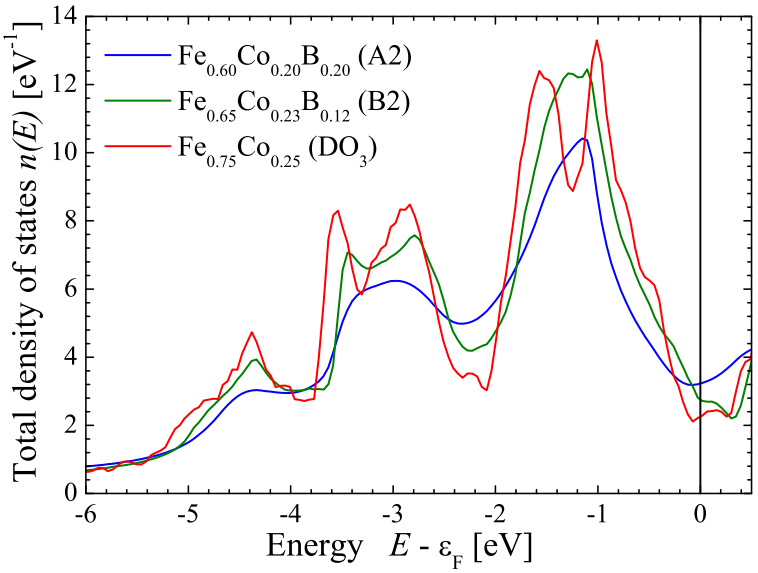

Figure 6.2: Total density of states of the $Co_xFe_yB_z$ alloy with $A2$, $B2$ and DO_3 structures for various B content.

6.4 Results and discussion

6.4.1 Electronic structure

Figure 6.2 compares the calculated total density of states of $Co_xFe_yB_z$ with fixed Fe : Co ratio ($x/y = 3:1$) and decreasing B content in the following: from $Fe_{0.6}Co_{0.2}B_{0.2}$ that was calculated assuming a random alloy with $A2$ structure to $Fe_{0.65}Co_{0.23}B_{0.12}$ for the partially ordered $B2$ structure and then further to $Fe_{0.75}Co_{0.25}$ for completely ordered DO_3 structure. This assumption originates from the fact that during the annealing process the structure of the CoFeB electrodes as well as their B content are changed leading to the observed behaviour of the TMR ratio. As one can see from this figure 6.2, in general, the shape of the DOS curves for all three types of structures with decreasing of boron amount is not markedly changed besides the fact that the loss of translational symmetry in the compound and therefore the finite lifetime broadening caused by a disorder leads to the smearing out of the final DOS curve. Thus the strongest smearing can be observed in the curve corresponding to the absolutely disordered case (A2) while the curve corresponding to completely ordered Fe_3Co compound looks rather structured. Furthermore it is obvious that different types of structures containing various amount of boron give various density of states at the fermi energy ϵ_F decreasing when going from the disordered A2 structure with highest B content to the ordered DO3 structure where B is absent.

Table 6.1 compares the calculated magnetic moments for $A2$ structure with change of the B content. The magnetic moments as found from the fully relativistic calculations

Table 6.1: Calculated magnetic properties for the random alloy with $A2$ structure. Values of the magnetic moments are given in multiples of the Bohr magnetron μ_B. The magnetic moments include the orbital moments. The average number n_V of valence electrons per atom is given for comparison with the Slater-Pauling rule (see Equation (6.1).

	n_v	m_{Fe}	m_{Co}	m_{tot}
$Fe_{0.60}Co_{0.20}B_{0.20}$	7.2	2.466	1.729	1.795
$Fe_{0.65}Co_{0.23}B_{0.12}$	7.62	2.512	1.802	2.039
$Fe_{0.75}Co_{0.25}$	8.25	2.588	1.908	2.419

include the orbital moments. Their influence is, however, small due to the well known quenching in cubic systems. Here, the ratio of orbital m_l to spin m_s moment is only about $m_l/m_s \approx 0.03$. It is seen that not only the total magnetic moment but also the atom specific moments at Fe and Co increase with decreasing B content. The same tendency is observed for the $B2$ structure (not shown here). That is, the increase of the total magnetic moment is not exclusively a consequence of the removal of the B atoms carrying no magnetic moment.

The $Fe_{1-x}Co_x$ alloys are known to be on the borderline between the localized and itinerant magnetism part of the Slater-Pauling rule [71, 72, 73, 74]. The increase of the magnetic moment with increasing number n_V of valence electrons suggests a localized behavior of the magnetic moments in $Co_xFe_yB_z$. In the case of localized moments, the Fermi energy is pinned in a deep valley of the minority electron density. This constrains the average number of minority d electrons $n_{d\downarrow}$ to be approximately three with the result for Fe and its bcc-like binary alloys (Fe-Cr, Fe-Mn, and partially Fe-Co):

$$\begin{aligned} m &= n_\uparrow - n_\downarrow = n_V - 2n_\downarrow \\ m &\approx n_V - 6 - 2n_{sp\downarrow} \end{aligned} \tag{6.1}$$

$n_{sp\downarrow}$ is the number of s and p minority electrons and the sum of majority and minority electrons $n_\uparrow + n_\downarrow = n_V$ is the average number of valence electrons per atom in the primitive cell. It was shown by Malozemoff *et al* [75] using *band-gap theory* that this holds principally also if using more realistic band structure models, even so they were initially derived from rigid band models. In particular, they have shown that the rule is still valid if metalloids are involved. From Equation (6.1) one expects magnetic moments in the range of about 1 to 2.5 μ_B depending on the occupation of the sp electrons. Deviations between Equation (6.1) and the calculated magnetic moments in Table 6.1 are attributed to the differences in the occupation numbers of the minority d electrons (not necessarily exactly 3) as well as the influence of the sp electrons. Overall,

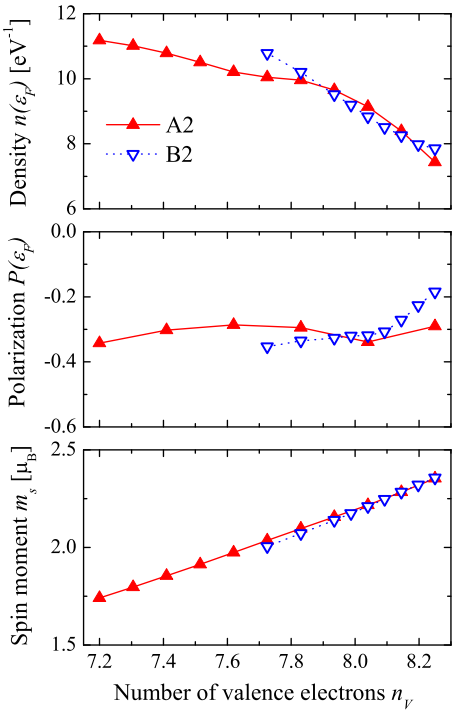

Figure 6.3: Calculated properties of the electronic structure of $Co_xFe_yB_z$ for $A2$ and $B2$ structures. The values corresponding to $B2$ structure were divided by the number of nonequivalent sites (for this type of disorder is 2) to allow the comparison.
(a) shows the density of states at the Fermi energy, (b) the corresponding spin polarization, and (c) the spin moment. All three quantities are given as function of the average number of valence electrons per atom.

the increase of the magnetic moment with removal of B is in agreement with a localized behavior of the magnetic moments at Fe and Co.

Figure 6.3 compares properties of the electronic structure that are important for the interpretation of the tunneling magneto resistance data. The calculations were performed for different composition and structure of $Co_xFe_yB_z$ with fixed iron : cobalt ratio ($x/y = 3:1$) and decreasing boron content from $Fe_{0.6}Co_{0.2}B_{0.2}$ to $Fe_{0.75}Co_{0.25}$. The random alloy and a $B2$-type ordered alloy were selected. In both structures the magnetic moment is nearly the same and increases with decreasing B content. This shows that not only the random but also the ordered alloy follows the Slater Pauling rule for localized moment systems as explained above.

Most interesting for the tunneling magneto resistance is the behavior of the electronic structure at the Fermi energy, in particular the density of states and the spin polarization as shown in Figure 6.3(a) and (b). The material is a weak ferromagnet because the electrons at ϵ_F that are responsible for transport are also responsible for the magnetic properties. For both structures the density of states $n(\epsilon_F)$ at the Fermi

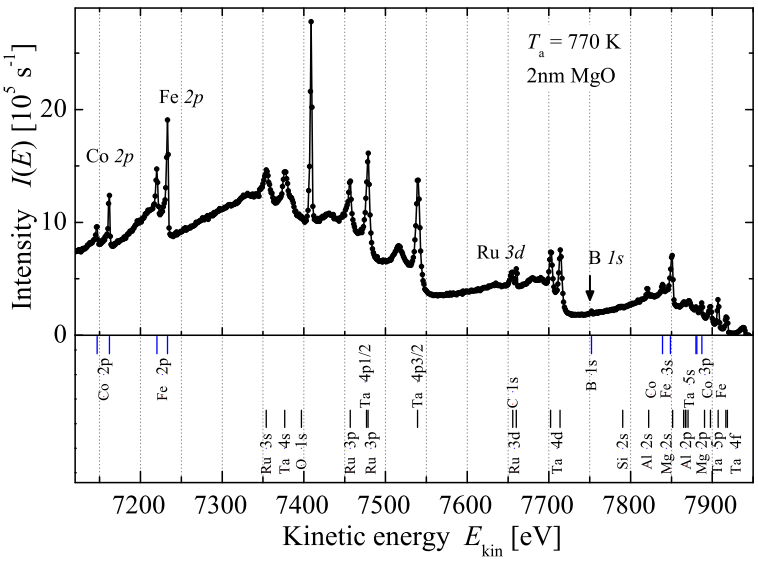

Figure 6.4: Wide energy scan hard X-ray photoemission spectrum of the $Co_xFe_yB_z$ sample annealed to 773 K. The raw intensity values correspond to the grey scale values provided by the spectrometer. Lines selected for a detailed study are assigned in the main figure. The remaining lines are separately indicated.

energy decreases with decreasing number of valence electrons. In the random alloy the absolute value of the spin polarization decreases when boron is removed and drops rather suddenly to a lower value when the pure $Fe_{0.75}Co_{0.75}$ is reached. The spin polarization of the ordered alloy behaves different, it shows a continuous decrease of its absolute value with decreasing B content. The lowest absolute value is also obtained for the B-free material.

6.4.2 Core level spectroscopy

Hard X-ray core level spectroscopy was used to investigate the influence of the annealing temperature on the chemical composition of the samples. The high kinetic energy of the emitted photoelectrons allows easily to study the core level of the buried layers.

Figure 6.4 shows a wide-range hard X-ray photoelectron spectrum of a multilayer sample annealed to $T_a = 773$ K. The spectrum covers an energy range of about 1 keV. The main excitations are marked. For the detailed investigation the lines with high intensity were selected and recorded with higher resolution in appropriate energy windows. The kinetic energies of the selected lines are all above 7 keV. The electrons from the valence band have nearly 8 keV kinetic energy and considerably lower intensities compared to most of the core levels.

Starting point was the study of the $2p$ emission of iron and cobalt to investigate the most important part of the metallic stack. The Fe and Co $2p$ core level spectra taken

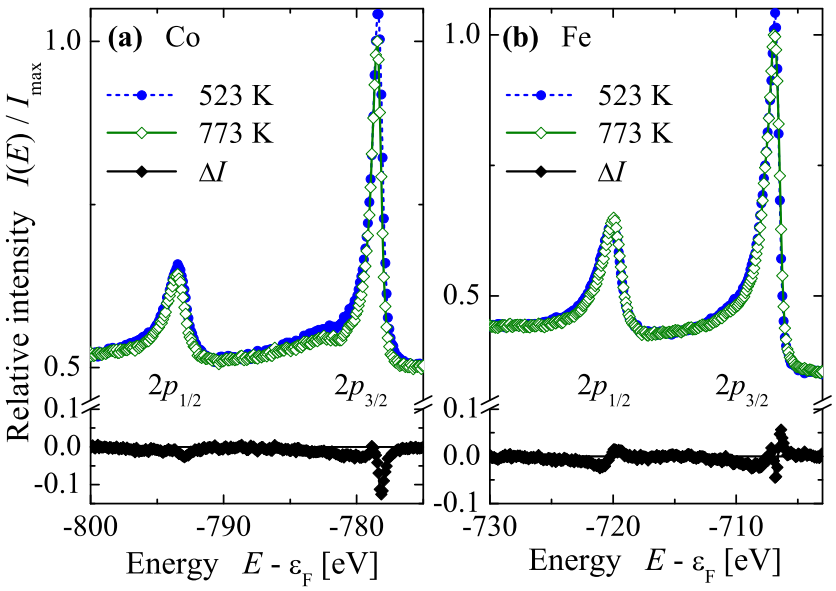

Figure 6.5: $2p$ core level emission from Co (a) and Fe (b) in $Co_xFe_yB_z$ at hν=7.9392 keV excitation energy.
The spectra were taken from samples annealed to 520 K and 770 K. The difference $\Delta I = I(520\text{ K}) - I(770\text{ K})$ is shown for better comparison.

from samples annealed to 523 K and 773 K are shown in Figure 6.5. The difference spectra of both constituents exhibit slightly smaller width of the $2p_{3/2}$ emission peaks for the sample annealed to the optimized annealing temperature of $T_a = 773$ K where the highest tunneling magneto resistance ratio is obtained. This points on an improved crystalline structure in the sample annealed to 770 K. Besides the change of the peak width, the shape of the difference spectra may give a hint on a very small chemical shift. Changes in the intensity are below the order of $\pm 0.3\%$. This observation includes spectra from samples with other annealing temperatures. It is concluded that the Fe and Co content in the CoFeB layer is rather stable against variation of the annealing temperature.

Very important information is contained in the Boron core level spectra. Figure 6.6(a) shows the B $1s$ core level spectra from samples that were annealed at different temperatures. The signal is drastically reduced in the sample annealed at 923 K. Due to the low intensity, a chemical shift can not be detected. In the sample with the optimized annealing temperature, the B $1s$ intensity is about 60% compared to the sample with the lowest annealing temperature as it can be noted from the fig. 6.6(b). Overall the decrease of intensity points to a decrease of the B content in the CoFeB layer with increasing annealing temperature. From the reduction of the signal it is obvious that a diffusion of B to the lower parts of the samples takes place. Wide-range spectroscopy of B$1s$ level revealed that the states detected in the experiment correspond to the states

of boron in metal that are shown as vertical bars. Furthermore it was found that no boron oxide is present in the samples even at very high annealing temperatures. Only a background signal at -194 eV is seen in Figure 6.6(c).

A second strong hint on the diffusion of B to the lower parts of the junction comes from the core level spectra of the tantalum $4f$ states. It is well known that the binding energy of those states is changed in different chemical environment leading to pronounced chemical shifts. The dependence of the Ta $4f$ emission is displayed in Figure 6.7 for different annealing temperatures. The appearance of a state with a chemical shift of about -0.7 eV at higher annealing temperatures is evident. This shift is in agreement with the formation of TaB. The intensity of the shifted component ("cs") increases on cost of the intensity of the initially non-shifted state ("0").

Assuming a diffusion of Ta into the above-lying CoFeB layer one would expect an increase of the overall intensity of the Ta $4f$ emission, opposite to the decrease of the B $1s$ intensity. From Figure 6.7(b), however, it is apparent that the total Ta $4f$ intensity does not change at least for annealing temperatures up to 770 K. At the highest annealing temperature even a reduction of the total intensity is observed. Therefore, an exchange of B by Ta in the CoFeB layer can be excluded. At the highest annealing temperature a long tail becomes visible at the low-energy side of the $4f_{5/2}$ state, this is one reason for the slightly reduced overall intensity. This might be a result of a further degradation of the Ta layer in the over-annealed sample.

The B $1s$ and Ta $4f$ core level spectra of the samples that refer to the upper electrode of the full tunnel junction (see fig. 6.1(II)) revealed the same tendency of diffusion of B atoms into the neighboring Ta layer. From Figure 6.8 the increase of the B signal with increasing annealing temperature is obvious. At the overheated sample (923 K) the Ta $4f$ states are completely shifted to the TaB binding energy, similar to the observation of the lower electrode. A BO_x signal is not detected. From this observation it is clear that B is always removed from the CoFeB layers and moves into the Ta layers.

It was also possible to investigate the ruthenium layer even though it is located much lower in the stack and covered by the Ta and CoFeB layers. The Ru $3d$ core level spectra are shown for the highest and lowest annealing temperature in Figure 6.9. Here, the spectra taken from samples with annealing temperatures of 520 K and 920 K were selected. The emission from the C $1s$ state is visible at the low energy side of the $3d_{3/2}$ state. This might emerge from CO adsorbed at the surface of the sample. Only at $T_a = 923$ K it becomes noticeably enhanced. Together with the observation at the Ta $4f$ states this may be another hint on the onset of degradation of the complete stack at too high annealing temperatures.

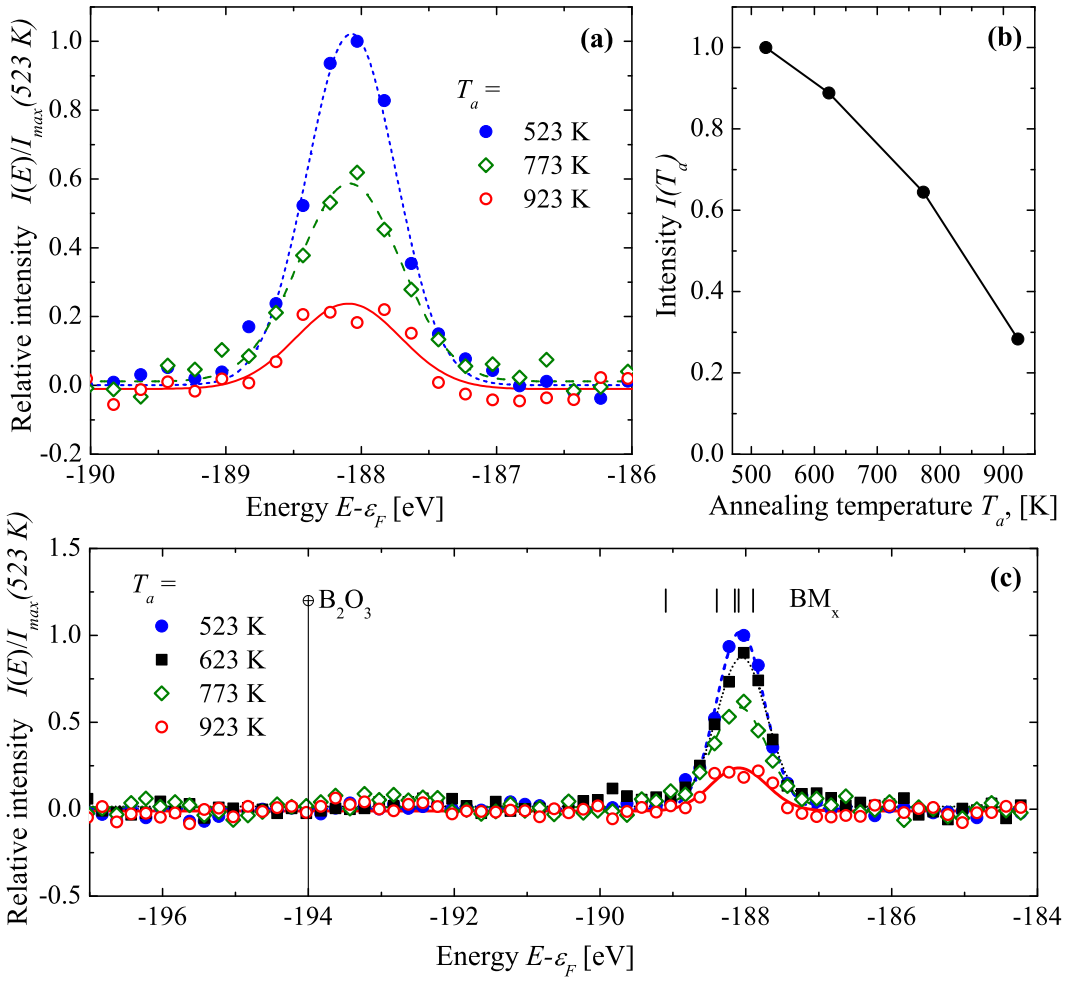

Figure 6.6: B 1*s* core level emission at hν=7.9392 keV excitation energy.
The spectra of the B 1*s* state with increasing annealing temperature T_a are shown in (a). Evaluation of the intensity as function of annealing temperature T_a is presented in (b). The intensities were calculated from the peak areas after a linear-type background subtraction and are given with respect to the area underneath the peak of the sample annealed at 523 K. (c) shows the wide-range spectrum of the B 1*s* level for the sample annealed at different temperatures. The bars indicate the various boron states in metal i.e. alloys, and the vertical line defines the position of the B_2O_3 state.

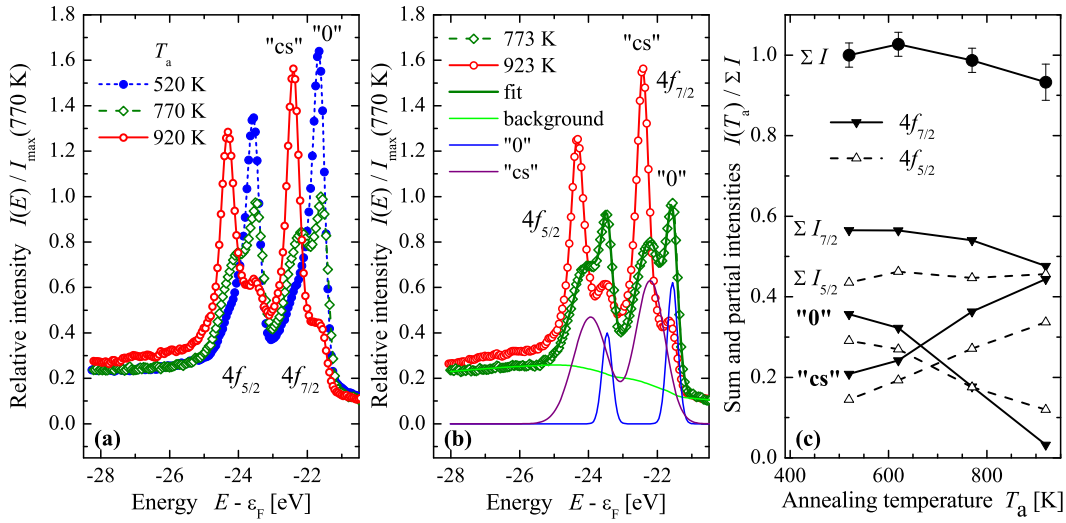

Figure 6.7: Ta $4f$ core level emission at hν=7.9392 keV excitation energy. (a) displays the spectra of the Ta $4f$ state with increasing annealing temperature T_a. The Ta $4f$ spectra taken from the $Co_xFe_yB_z$ samples annealed at 773 K and 923 K are shown in (b) together with the fit of the background and constituent states. (c) presents the evaluation of the partial and total intensities as function of T_a. The intensities were calculated from the peak areas and are given with respect to the area underneath the $4f_{7/2}$ peak of the sample annealed to 523 K. **"0"** and **"cs"** assign the initial and the chemical shifted states, respectively.

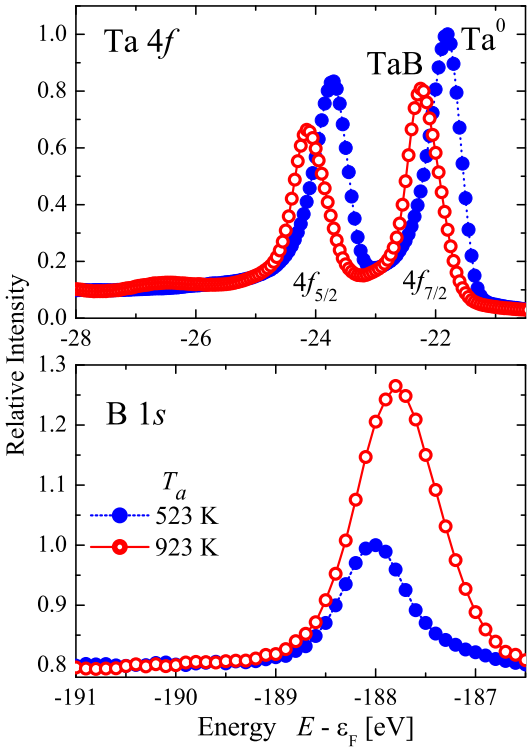

Figure 6.8: B 1s and Ta 4f core level spectra of the full tunnel junction (fig. 6.1(II)) at hν = 7.9392 keV excitation energy.
Displayed are spectra for two annealing temperatures T_a.

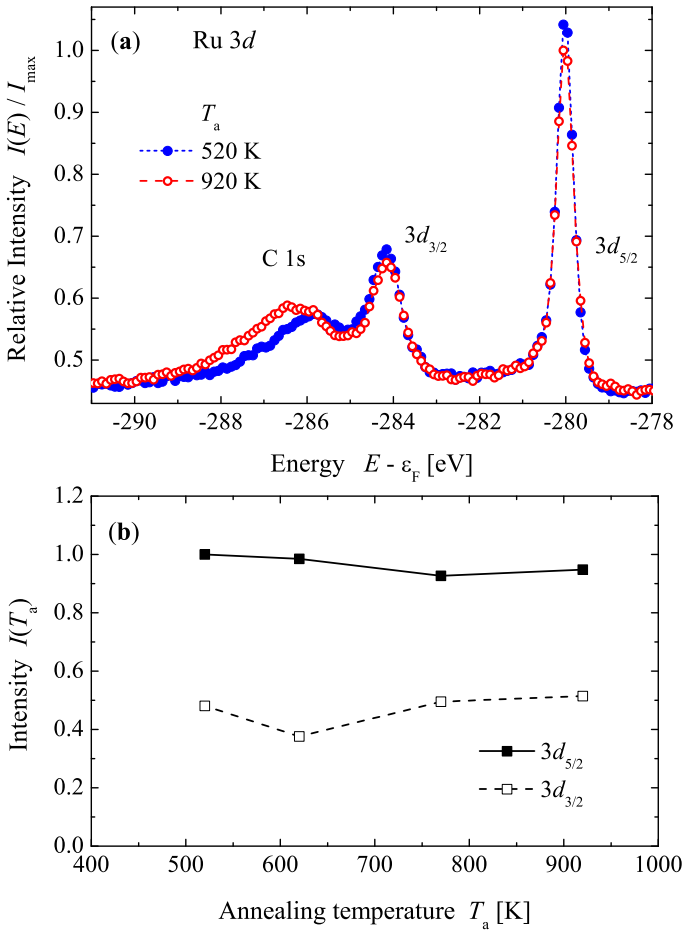

Figure 6.9: Core level emission of Ru 3d states taken at hν=7.9392 keV excitation energy.
(The spectra of the Ru 3d states for the samples annealed at T_a = 523 K and 923 K are shown in (a). The bottom panel (b) presents the evaluation of the intensities as function of T_a. The intensities were calculated from the peak areas and are given with respect to the area underneath the $3d_{5/2}$ peak of the sample annealed to 523 K.

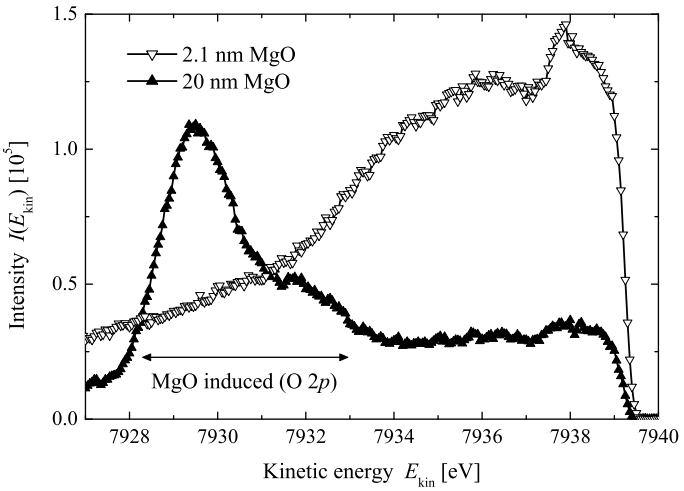

Figure 6.10: Comparison of HAXPES valence band spectra for different thickness of the top MgO layer. The raw, unscaled intensity values correspond to the grey scale values provided by the spectrometer.

6.4.3 Valence band spectroscopy

Starting point of the investigation of the valence band was the study of the influence of the states from the MgO cover layer on the visibility of the states from the CoFeB layer. Figure 6.10 compares the valence band spectra from samples covered by MgO layers of 2.1 nm and 20 nm thickness. The oxygen 2*p* states from MgO are the dominant signal for the sample with a 20 nm thick MgO layer, but the valence region is still visible. The comparison of the spectra reveals that the spectrum of the sample with 2.1 nm thick MgO cover is dominated by the emission from the CoFeB layer. A contribution of the MgO states can be neglected in the valence band spectra of the samples with thin cover layer. It was also checked that an additional 1 nm thick AlO_x protective layer does not change the results.

The spectra of the topmost part of the valence band are compared in Figure 6.11 for samples corresponding to the lower part of the MTJ (fig. 6.1(I)) shown in (a) and to the upper electrode of the MTJ (fig. 6.1(II)) (b) annealed at different temperatures. As one can see at low annealing temperatures (523 K, 623 K), the spectra exhibit a maximum at about -400 meV only for the lower electrode. Increasing the annealing temperature, this maximum is reduced and vanishes in the sample annealed to 773 K where the highest tunneling magneto resistance is observed. The absence of this maximum, specific for CoFeB compound, in the upper part of MTJ is explained by the fact that obtained signal from CoFeB layer is overlapped with the signal from overlying 5-nm-thick Ta layer and 2-nm-thick MgO layer. The limited probing depth, reduction of the signal rising from the deeper layers and higher crossections of Ta valence states than that for Co and Fe valence states lead to the reduction of obtained information from the CoFeB

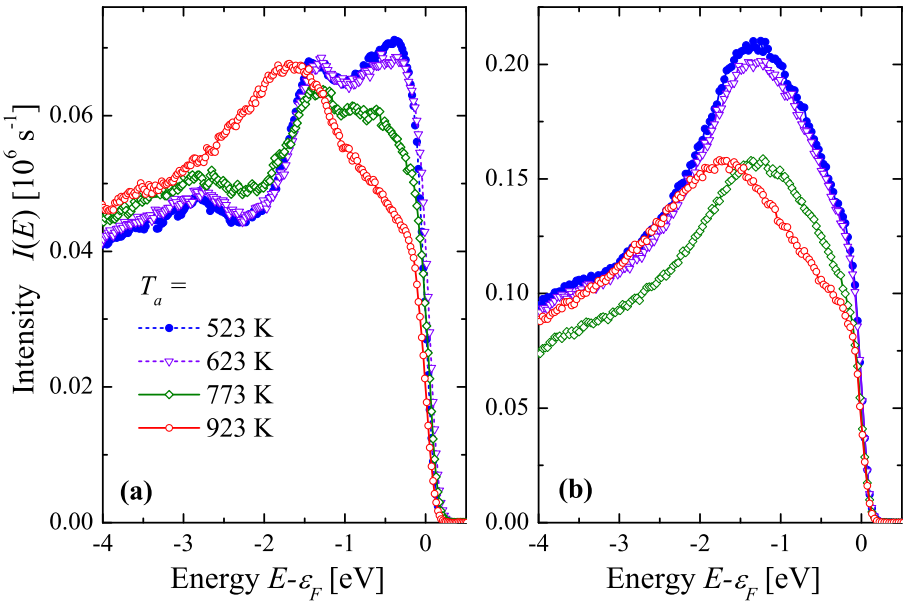

Figure 6.11: Valence band spectra of the samples annealed at different temperatures, T_a are compared after Shirley-type background subtraction.
The measurements were performed at room temperature. The curves corresponding to the lower part of the MTJ (fig. 6.1(I)) are shown in (a) while the spectra taken for the full MTJ (fig. 6.1(II)) are displayed in (b).

layer itself in such a complex multilayer stack. The maximum observed at -1.4 eV still persists at that annealing temperature in both upper and lower parts of the MTJ. Finally, in the samples annealed at 923 K the complete structure of the valence band is changed, indicating degradation of the multilayer stack, and the maximum is shifted by 300 meV away from the Fermi energy level for both electrodes.

Figure 6.12 compares the valence band spectra of the low temperature annealed sample (523 K) and the sample with optimized annealing temperature (773 K) to the calculated density of states. As mentioned in Section 6.4.1, there is no pronounced difference of the general shape of the calculated density of states recognized if changing the composition by removal of B. The measured spectrum of the sample annealed to T_a = 773 K corresponds well to the calculated density of states. Obviously, the spectrum of the sample with a low annealing temperature of T_a = 523 K exhibits an enhancement of states close to the Fermi energy that is in a good agreement with the observed enhancement of the DOS at the Fermi energy for the absolutely disordered alloy of A2 structure. The discrepancy in the intensity can be caused by the dependence of the line widths and their intensity on the binding energy following from lifetime broadening effect. This gives a hint that the structure at low annealing temperature is different from the expected cubic lattice or that parts of the sample are in an otherwise different state. This is in agreement to the observation that the CoFeB starts to

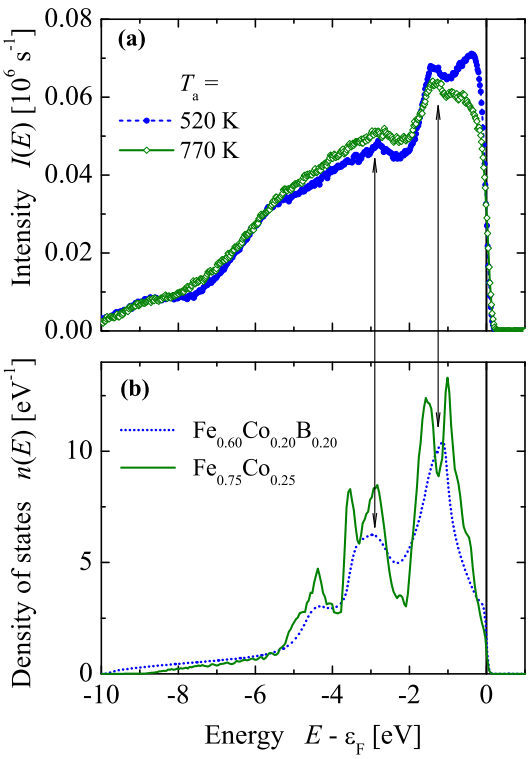

Figure 6.12: Comparison of HAXPES valence band spectra (a) and calculated total density of states (b).
The measurements were performed at room temperature. For better comparison a Shirley-type background was subtracted from the spectra and the density of states was convoluted by the Fermi-Dirac distribution for T=300 K.

crystallize in a *bcc*-type lattice with (001) oriented texture at annealing temperatures above 623 K.

Finally, the influence of the sample temperature on the valence band close to the Fermi energy was studied. Figure 6.13 shows valence band spectra close to ϵ_F with a change of the sample temperature from 20 K to 300 K. The spectra reveal that the used experimental resolution of better than 5×10^4 is sufficient to follow changes caused by the change of sample temperature. The spectra were taken from samples annealed to $T_a = 523$ K and 773 K. In both cases, the only pronounced change is the broadening of the Fermi edge according to the broadening of the Fermi-Dirac distribution at elevated temperature. Indeed, the spectra correspond to a signal averaged over the film thickness and changes directly at the CoFeB-MgO interface can not be completely excluded.

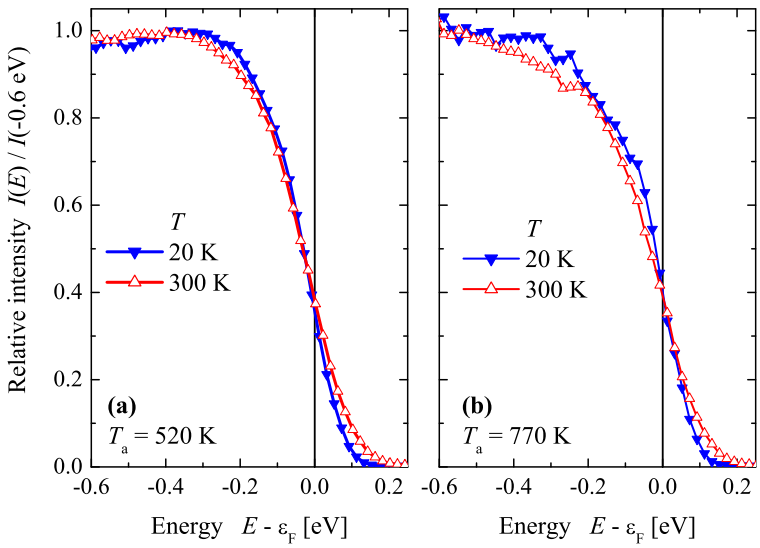

Figure 6.13: Temperature dependence close to the Fermi energy.
The valence band emission close to ϵ_F is compared for a change of the sample temperature from 20 K to 300 K for the samples annealed to T_a = 523 K (a) and 773 K (b).

6.5 Summary and conclusions

The present study demonstrates the feasibility of HAXPES to explore the electronic structure in deeply buried layers in a nondestructive way. Here, the enforced diffusion of B from the CoFeB into the Ta layers of a magnetic tunnel junction was investigated. The HAXPES spectra of the B 1s and Ta 4f core levels reveal that boron is rapidly diffusing into the contiguous tantalum layers upon annealing of the tunnel junction. In the lower half of the junction the B signal decreases with higher annealing temperatures, whereas it increases in the upper part of the junction. At the same time the chemically shifted Ta-B part of the Ta 4f signal increases in both layers. The improvement of the TMR is thus not only caused by an improvement of the structure but also by a change of the composition in the CoFeB layers. The degradation of the (001) orientation caused by Ta diffusion into the CoFe(B) layer [59], i.e. the lowering of tunneling spin polarization, explains the sudden drop of the TMR when the sample is over-heated.

7 HAXPES on Co_2MnSi-based magnetic tunnel junctions

7.1 Introduction

Spintronics attracts a scientific and technological interest first of all because it provides the efficient devices with much lower energy consumption compared to their electronic equivalents. One of the most important spintronic components is the so-called magnetic tunnel junction (MTJs) which allows to control the electric current by small magnetic fields. High-performance MTJs are characterized by a large tunneling magnetoresistance (TMR) ratio which first of all is defined by the properties of the materials used for the electrodes and therefore as a source of spin-polarized carriers in spintronic devices [4]. Many of the Co_2 based Heusler compounds have been suggested to be half-metallic ferromagnets (HMFs) that exhibit distinctive transport properties and provide a perfect spin-polarized electrical current. This behaviour of the Heusler compounds is determined by their intrinsic electronic structure in the vicinity of the Fermi energy (ϵ_F) where it is completely spin-polarized [20, 76].

Among the variety of other HMFs, Co_2MnSi is considered to be the most promising candidate for reaching large TMR ratios due to its large minority band gap of 0.81 eV and very high Curie temperature of 985 K [77, 78]. Large TMR ratios of 570% at 2 K and 67% at room temperature (RT) were revealed by Sakuraba *et al* [21] for junctions with Co_2MnSi film electrodes and AlO_x tunnel barrier. Such a huge decrease of the TMR ratio with increasing temperature typically occurs due to a thermal activation of magnons [79], whereas the significant deviations obtained at the same temperature in different experiments are related to the interfacial atomic disorder [80], interface oxidation, and spin scattering on defects [81, 82]. Ishikawa *et al* [83] reported about completely epitaxial MTJs with Co_2MnSi as a lower electrode, CoFe as an upper one and MgO tunnel barrier. TMR ratios of 90% at RT and 192% at 4.2 K were achieved for these films. The fabrication of fully epitaxial layers is extremely desirable for such structures due to significant reduction of depolarization mechanisms in electrode layer, tunnel barrier, and interfaces. Epitaxial growth of magnetic tunnel junctions with Co_2MnSi used for both electrodes with single-crystalline MgO barrier was demonstrated and even larger TMR ratios of 179% at RT and 683% at 4.2 K were successfully

achieved [84].

Recently magnetoresistive characteristics of fully epitaxial MTJ structures with $Co_2Mn_\alpha Si$ electrodes were investigated with respect to the Mn content α. It was shown that the TMR crucially depends on the stoichiometry of the ferromagnetic layers. In particular, for the Mn-poor regime the TMR decreased due to Co atoms substituting Mn on its regular positions. Besides for $\alpha > 1$ (Mn-rich regime) a TMR ratio of up to 1135% at 4.2 K and 236% at RT was reached that can be attributed to the absence of disorder [85]. These effects are essentially reflected in the density of states (DOS) nearby ϵ_F, therefore it is very important to study the dependence of the electronic structure of Co_2MnSi layers with respect to compositional variations.

The investigation of the electronic structure of materials as well as their chemical composition is feasible by X-ray photoelectron spectroscopy (XPS). Under laboratory conditions with energies obtained from commonly used Al- K_α (1486.6 eV) and Mg-K_α (1253.6 eV) sources this method is extremely surface sensitive with an electron escape depth in the order of few angstroms only [48]. The development of synchrotron facilities gave a unique opportunity to utilize high-energy radiation for hard X-ray photoelectron spectroscopy (HAXPES) that increases the probing depth by an increase of the inelastic mean free path of the photoemitted electrons. The high photon flux obtained on third generation synchrotron facilities along with an appropriate beam focusing which delivers high flux density onto the sample allows to reach high intensities of the photoemitted electrons [86, 87]. Together with high resolution this makes HAXPES a very effective technique in particular for investigation of the valence states. Being bulk sensitive, HAXPES becomes an extremely important instrument in examining of buried layers and interfaces in heterostructures such as MTJs.

The present study is focused on the effects of non-stoichiometry and chemical disorder and their impact on the spin polarization in the Co-Mn-Si alloy series. HAXPES was applied to investigate the electronic structure of the Co_2MnSi ferromagnetic layer with respect to its stoichiometry. *Ab-initio* calculations of the electronic structure were performed in addition and the related depolarizing mechanisms are analyzed.

7.2 Samples description

$Co_2Mn_\alpha Si$ films (50 nm) were deposited on the MgO substrate using an additional 10 nm thick MgO buffer layer. To protect the surface of Co_2MnSi layers, the films were covered by MgO layers of 2 nm thickness as is used in half TMR junctions (see Figure 7.1). The topmost AlO_x capping layer was added for protection of the hygroscopic MgO barrier. Magnetron sputtering was used for $Co_2Mn_\alpha Si$ and Al layers. The MgO layer were grown by electron beam evaporation. Each layer of the structure was deposited in an ultrahigh vacuum chamber with a base pressure of about $6 \cdot 10^{-8}$ Pa.

The AlO_x cap layer was finally prepared by exposing the deposited Al layer to an O_2 atmosphere of 10^5 Pa for 2 hours. Co-sputter deposition from an additional Mn target was applied to vary the Mn content (α) in the $Co_2Mn_\alpha Si$ thin films. In the present experiments three different sets of samples were used that are corresponded to the three different contents of Mn and Si that are Mn: 1.23, Si: 0.93 (Mn-excess); Mn: 1.01, Si: 1.01 (nearly stoichiometric); Mn: 0.69, Si: 1.01 (Mn-deficiency) [85].

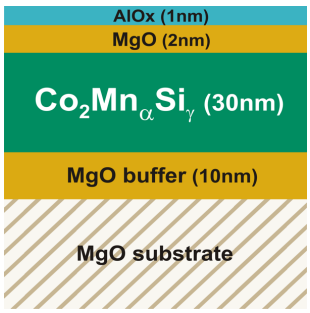

Figure 7.1: Schematic sketch of the sample structure corresponding to the lower part of a MTJ with a $Co_2Mn_\alpha Si_\gamma$ electrode. $\alpha = 0.69; 1.01; 1.23$ and $\gamma = 1.01; 1.01; 0.93$, respectively.

7.3 Results and discussion

7.3.1 Core level spectroscopy

The core level photoelectron spectra of $Co_2Mn_\alpha Si$ thin films show rather similar features for different compositions and excitation energies. The spectra of the Co and Mn $2p$ states measured for the $Co_2Mn_{1.23}Si_{0.93}$ thin film using excitation by 3.24 and 7.94 keV photons are presented in Figure 7.2. The observed spin-orbit splitting of the $2p$ states is about 11.2 eV for Mn and 14.95 eV for Co.

It is clearly seen in Figure 7.2 that both states of the Mn $2p$ spin-orbit doublet are further split into several components, most pronounced at 2 and 4 eV below the main spin-orbit split components. These spectral features are observed due to a complex multiplet splitting. This effect was demonstrated in theoretical calculations on atomic Mn [88, 89] as well as in the experiments on Mn based Heusler alloys [90]. The appearance of a reach multiplet structure stretched down in energy from the main $2p$ maximum caused by exchange interaction of the $2p$ core hole with the valence electrons in the partially filled $3d$ shell was shown. The positions of the satellites maxima do not show any considerable dependence on the excitation energy while their relative intensity is reduced when excited by lower energy photons. Such redistribution in the intensities is caused by the changes either in the differential cross-sections for different multiplet states, the angular asymmetry parameters, or both.

The Co $2p$ core spectra of $Co_2Mn_\alpha Si$ thin films reveal also pronounced satellites that are located at about 4 eV below the Co $2p_{3/2}$ main peak. The observed satellite of the Co $2p$ state in Co_2MnSi may be explained by an energy loss due to a $3d-n's$ interband transition. This is typically observed for fcc lattices and appears also in absorption spectra [91]. Additionally, it may be caused by exchange interaction similar to the multiplet observed at Mn but caused by the $3d$ open shell configuration of Co.

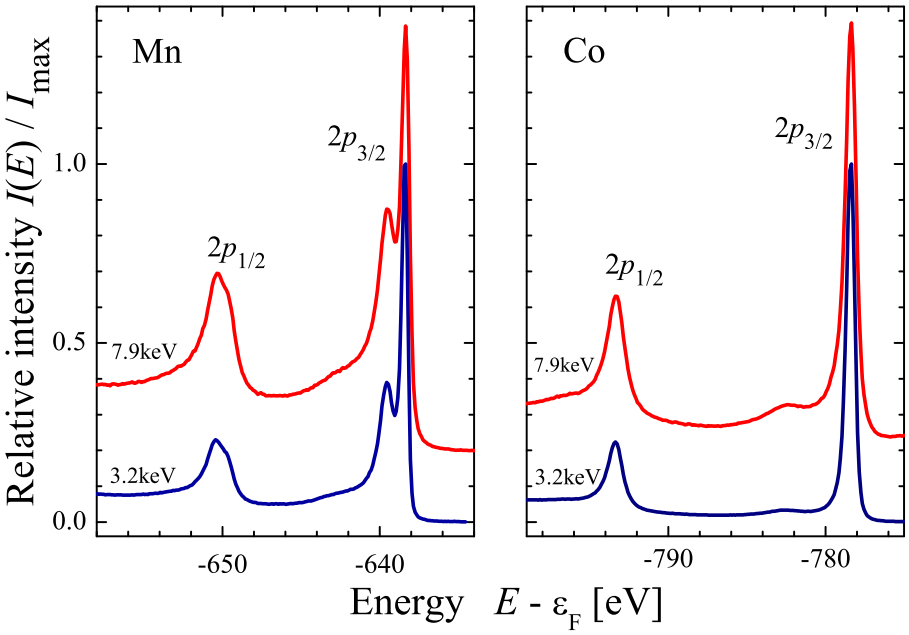

Figure 7.2: Photoelectron spectra of the Co and Mn $2p$ core levels from $Co_2Mn_{1.23}Si_{0.93}$ excited by photons of 3.24 and 7.94 keV energy. The spectra were taken at 300 K. They are normalized to the maximum intensity of the $2p_{3/2}$ peak.

Table 7.1 summarizes the ratios of the Co to Mn intensities from the respective peaks in the core level spectra for both films with excess and deficiency of Mn upon two different excitation energies (3.24 and 7.94 keV at 300 K). The intensities were calculated from the peak areas. The background correction and peak fitting to the multiple components performed for the doublets of Mn and Co yield some uncertainties. Nevertheless, the calculated Co/Mn intensity ratio shows a rather stable decrease of about 3.7 and 3.2 in the $2p_{1/2}$ and $2p_{3/2}$ multiplets when the $Co_2Mn_\alpha Si$ composition is changed from 2 : 0.69 : 1.01 to 2 : 1.23 : 0.93. The higher value of the Co/Mn intensity ratio in the $2p_{1/2}$ states (see Table 7.1) may arise from a smearing of the Mn $2p_{1/2}$ peak due to the reduced life-time of the Mn $2p_{1/2}$ core hole. However, the revealed behavior of the ratio of the photo-efficiency from the Co and Mn $2p$ states is mostly effected by (i) the photoelectron escape conditions defined by the combination of film homogeneity with the escape depth of the electrons upon a certain excitation energy and (ii) by the dependence of the cross section on the element and the excitation energy.

Table 7.1: Co/Mn intensity ratio of the $2p$ states for different $Co_2Mn_\alpha Si$ composition and excitation energies.

Co/Mn		
Multiplet component	1/2	3/2
Excitation energy 3.24 keV		
$Co_2Mn_{1.23}Si_{0.93}$	7.90	6.67
$Co_2Mn_{0.69}Si_{1.01}$	28.83	21.22
Excitation energy 7.94 keV		
$Co_2Mn_{1.23}Si_{0.93}$	2.98	1.99
$Co_2Mn_{0.69}Si_{1.01}$	11.60	6.29

Hence, the close factor of changes in the Co/Mn intensity ratio upon modification of the $Co_2Mn_\alpha Si$ composition observed for different excitation energies point out at the homogeneity of the studied films. The Co/Mn intensity ratio calculated from the area of the photoemission maxima does not reproduce the stoichiometry in $Co_2Mn_\alpha Si$ film because of the different energy dependence of the partial cross section of the $2p$ states for Co and Mn [92]. The calculated Co/Mn intensity ratio is about 3 times reduced at higher excitation energy (7.94 keV) because of the different slope in the cross section behavior for the $2p$ orbitals of Co and Mn [92].

Figure 7.3 displays the photoelectron spectra from the shallow core states of the $Co_2Mn_{0.69}Si_{1.01}$ thin films underneath a MgO barrier and AlO_x capping layer. The excitation energies were 3.24 and 7.94 keV. The spectra are normalized to the intensity of the Co $3p$ peak and present the features common for all samples of the studied Co_2MnSi thin films. Upon excitation by 3.24 keV X-rays, the peaks from Mg and Al states are more pronounced compared to the case of 7.94 keV photo excitation. In the latter case, the peaks from the elements of the buried $Co_2Mn_{0.69}Si_{1.01}$ film clearly increase. Such a redistribution of the intensity of the shallow core level is due to the energy dependence of the inelastic mean free path of the electrons [92, 93]. In case of a higher excitation energies, the inelastic mean free path of the electrons increases and the contribution of the buried $Co_2Mn_{0.69}Si_{1.01}$ layer is enhanced. Upon the changes of the excitation energy, the profile of the photoemission peaks around 100 eV below ε_F is considerably changed. This peak results from the combination of the Si $2p$ and the Co $3s$ states. In this case, both, Co and Si signals correspond to the buried layer. The observed relative changes in their intensities are caused by the differences of the cross section for Si $2p$ and Co $3s$ electrons while changing the excitation energy [92]. From the core level photoelectron spectroscopy it is concluded that the studied $Co_2Mn_\alpha Si$

multilayers are of high homogeneity.

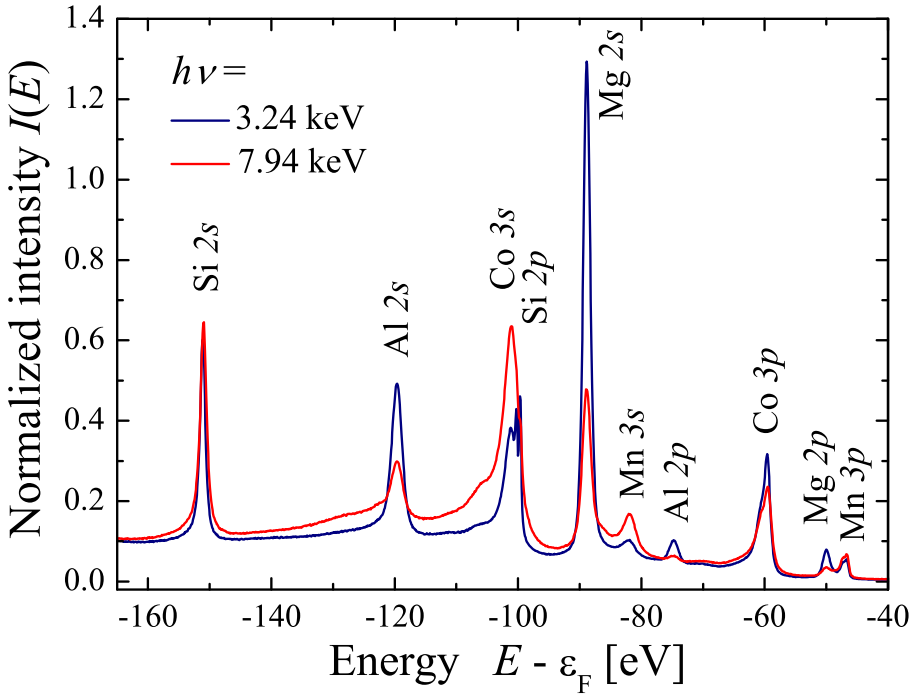

Figure 7.3: Photoelectron spectra in the range of shallow core levels of $Co_2Mn_{0.69}Si_{1.01}$ underneath the MgO barrier and AlO_x capping layer upon excitation with different photon energies. The spectra are normalized to the maximum intensity of the Co $3p$ line.

7.3.2 Valence band spectroscopy

The photoelectron spectra of buried $Co_2Mn_\alpha Si$ films measured for the valence states are shown in Figure 7.4. The measurements were again taken with different photon energies. The composition dependence of the $3d$ orbital derived density of states is better distinguished for low energy excitation (3.24 keV). This is explained by the different behavior of the cross sections for the s, p, and d orbitals while changing photon energy [92]. The cross section for d orbitals decreases much stronger with increasing photon energy than that of s or p states. The electron mean free path is however reduced for electrons with smaller kinetic energies what may also lead to changes in the spectra if using different excitation energies.

The main features of the valence band spectra of the studied thin films agree well with those observed for stoichiometric Co_2MnSi bulk samples [93, 65]. The spectra of the Co_2MnSi films show however a more smeared structure due to the band broadening. This broadening of the bands is explained by the disturbed translational periodicity due to the random site occupation in off-stoichiometric Co_2MnSi layers.

The smearing of the characteristic Heusler *sp* hybridization gap (around - 8.2 eV) and contributions of the *p*-like states around -9 eV is more pronounced at lower excitation energy. This is an effect of the MgO overlayer where the onset of the O 2*p* states appears at about -5 eV with a maximum at -9.2 eV [93, 65]. Especially at the lower excitation energy the electron mean free path is lower and a stronger influence of those states on the spectra is expected. Therefore, the Si a_{1g} states and the *sp* hybridization gap appear less pronounced due to the presence of MgO overlayer. The identical oxide layers allow still to compare the spectra taken at the same energy from the films with different composition. In the spectrum corresponding to the Mn excess sample one observes shifts of the two well pronounced maxima at energies of about -10 eV and -6.4 eV towards lower energy in comparison to the spectrum of the Mn deficient sample. Such shifts are attributed to changes in the Si a_{1g} states and point on a weaker bond between Si atoms and the surrounding Co atoms in the sample with excessive concentration of Mn ($\alpha = 1.23$). Moreover such shrinking of the whole valence band spectrum towards ε_F is in complete agreement with the theoretically calculated electronic structure when excessive Mn substitutes the Si site. For the low photon energy spectrum (Figure 7.4 (a)) the small feature arising at about -8.2 eV in the Mn deficiency case indicates the change in *p*- states contribution to the photoelectron spectrum, which can be attributed to the presence of Si atoms substituting Mn ones on their natural positions.

With respect to transport properties of the Heusler compounds it is more important to consider the details of the electronic structure in the vicinity of ε_F. Therefore, high resolution spectra of the relevant energy range are shown in Figure 7.5. The maximum in the density of *d* states at -1.35 eV is clearly resolved in the spectra. It arises from flat Co t_{2g} minority and Mn e_g majority states. In particular the Co t_{2g} minority states form the lower energy part of the minority band gap [65] and thus the minority valence band maximum. The intensity at -1.35 eV varies when the Mn content is changed, that is the peak appearing at this energy for the Mn deficiency case is shifted closer to the Fermi edge for the sample with excess of Mn. The same situation is observed in the spectra taken with 7.94 keV excitation energy (Figure 7.5 (b)). The composition dependence of that *d* states intensity is more pronounced upon excitation by X-rays of 3.24 keV energy. The intensity from the steep Co t_{2g} majority bands arises directly at ε_F. The spectra taken at 7.94 keV photon energy reveal that the distribution of those states is more smeared in the sample with $\alpha = 1.23$ compared to $\alpha = 0.69$. In the latter case the intensity is higher and results in a sharper Fermi edge.

In Figure 7.5 (b) one clearly distinguishes the appearance of an additional peak at about -0.2 eV in the spectrum of the Mn-deficient sample. In that case some density of states emerges in the vicinity of the Fermi energy. This is well confirmed by the calculated electronic structure for the sample with Mn deficit where such states appear

obviously in the minority bands (Figure 7.7 (a)). For the case of 7.94 keV photon energy the relative differences between off-stoichiometric and stoichiometric samples are illustrated in Figure 7.5(c). The significant redistribution in the density of states close to ε_F is observed only for the case of Mn deficiency which is in a good agreement with electronic structure calculations.

The experimentally observed changes in the valence spectra of $Co_2Mn_\alpha Si$ system are affected, firstly, by substitution of Si and Co atoms by excessive Mn atoms for the sample with a Mn concentration $\alpha = 1.23$ and, secondly, by the increased number of electrons for the sample with the deficit Mn concentration of $\alpha = 0.69$. As a consequence, the total magnetic moment as well as the spin polarization at ε_F steeply decreases leading to significant deviations of the TMR with respect to the changes of the Mn content in the sample.

7.3.3 Electronic structure of off-stoichiometric Co_2MnSi

For further analysis of non-stoichiometry effects in the Co-Mn-Si alloy series *ab-initio* calculations of the electronic structure were performed. The convenient way to account for the random disorder is the coherent potential approximation (CPA) [94, 68] which is easily formulated in terms of the Green's function formalism. This approach is alternative to the previous study of Co-Mn-Si alloy by the so-called cluster expansion method [95] which takes into account the local order effects, however is limited by the finite cluster sizes. For this reason the so-called KKR (Korringa-Kohn-Rostoker) Green's function method implemented within the Munich SPR-KKR program package [66] was used. Since it was shown for the stoichiometric compound that the local correlations do not significantly influence the electronic structure in the vicinity of the ε_F, [96] the exchange-correlation potential is treated in terms of local density approximation (LSDA) using the Vosko-Wilk-Nusair parametrization [69].

As it was shown in recent experiments [85, 97] the TMR ratio crucially depends on the Mn composition. The TMR signal appears at $\alpha \approx 0.6$ and monotonously increases until it reaches its maximum at $\alpha \approx 1.3$. Further increase of α rapidly suppresses the TMR which completely vanishes at $\alpha > 1.5$. This behaviour of the TMR is similar in both regimes: at 4.2 and 300 K. For the Mn-poor regime ($\alpha < 1$) the TMR decrease was explained mainly by formation of Co_{Mn} antisites which impose the extra states into the half-metallic band gap. Based on the evaluated energies and related probabilities [95, 98] of possible defects in Co-Mn-Si alloys it follows that formation of voids at the missing Mn positions is unfavorable, that is the lack of Mn is fully supplied by Co and Si antisites with Co:Si constant ratio of about 2:1 [97]. This results into the composition formula of $Co_2[Co_{2\left(\frac{1-\alpha}{\alpha+3}\right)}Mn_{1-3\left(\frac{1-\alpha}{\alpha+3}\right)}Si_{\left(\frac{1-\alpha}{\alpha+3}\right)}]Si$ for the Mn-poor regime ($\alpha < 1$). For the Mn-rich case ($\alpha > 1$) the extra Mn atoms tend to

Table 7.2: Site occupations of the primitive cell for different values of Mn relative content α.
For $\alpha < 1$ Co:Mn:Si amounts related to 2:1:1, for $\alpha > 1$ Mn is distributed equirandomly at Co and Si sites. The site occupation for the $L2_1$ structure is given for comparison.

Composition	α	Co (8a)	Co_{Mn} (4a)	Mn (4a)	Mn_{Co} (8a)	Mn_{Si} (4b)	Si_{Mn} (4b)	Si (4b)
$Co_2Mn_{0.8}Si$	0.8	100%	10.5%	84.2%	0	0	5.3%	100%
$Co_2Mn_{0.95}Si$	0.95	100%	2.5%	96.2%	0	0	1.3%	100%
Co_2MnSi	1	100%	0	100%	0	0	0	100%
$Co_2Mn_{1.2}Si$	1.2	95.2%	0	100%	4.8%	4.8%	0	95.2%
$Co_2Mn_{1.4}Si$	1.4	90.9%	0	100%	9.1%	9.1%	0	90.9%
Co_2MnSi	$L2_1$	100%	0	100%	0	0	0	100%

substitute Co with a bigger probability than Si, however in both cases the energy of the corresponding antisites is substantially higher than that for the Mn-poor regime. Since the CPA anyway allows to calculate the partial (type-resolved) quantities, a equirandom substitution of Co and Si by extra Mn atoms is assumed, that is for the Mn-rich regime the composition formula becomes $[Co_{(\frac{4}{3+\alpha})}Mn_{(\frac{\alpha-1}{3+\alpha})}]_2Mn[Si_{(\frac{4}{3+\alpha})}Mn_{(\frac{\alpha-1}{3+\alpha})}]$.

In a regular $L2_1$ structure of the X_2YZ Heusler compounds the atoms occupy the Wyckoff positions 8a (X_2) (T_d), 4a (Y) (O_h), and 4b (Z) (O_h) of the primitive cell with $Fm\overline{3}m$ symmetry (space group 225). More descriptively, the site occupations at the relevant α values are summarized in Table 7.2 in the following: Co_{Mn} corresponds to Co replacing Mn at the 4*a* position, Mn_{Co} - to Mn replacing Co at 8*a*, Mn_{Si} - to Mn replacing Si at 4*b* and Si_{Mn} - to Si replacing Mn at its 4*b* position.

As it follows from Figure 7.6 (a), theoretical the TMR ratio estimated from the Jullière model [6] fairly agrees with experiment [85, 97]. Since it is derived from the spin polarization shown in Figure 7.6 (b), which in turn depends on the density of states at the Fermi energy, $P = (n^{\downarrow} - n^{\uparrow})/(n^{\downarrow} + n^{\uparrow})$, the TMR behaviour can be explained by analyzing the density of states at different Mn content (Figure 7.7). It immediately follows that the reduction of the spin polarization and the TMR in the Mn-poor regime is due to an intensive filling of the half-metallic band gap. More detailed analysis reveals that this effect is indeed caused by Co_{Mn} antisite states shown in Figure 7.8. In contrast, in the Mn-rich case the corresponding decrease of spin-polarization is the simultaneous effect of all types of Mn atoms due to an increase of the interaction along the short tetrahedral bonds, that is of $Mn_{Mn,Si}$ (Mn in its native 4a position and Mn_{Si} antisites, respectively) with Mn_{Co} antisites.

As it follows from the total density of states in Figure 7.9 the intensity at the Fermi energy in both Mn-poor and Mn-rich regimes raises up when going away from the stoichiometry. As discussed above, in the first case this occurs due to the filling of the band gap in the minority-spin (Co_{Mn} antisites), in the second - due to increase of intensity in the majority-spin channel (Mn_{Co} antisites). This agrees well with the pronounced step- like structure in the range of -1 to 0 eV in the measured VB-XPS spectra (Figure 7.5) for the Mn-poor regime since the Co_{Mn} impurity- like states in the band gap give a sharp intensity peaks. In addition the calculations also show the smearing of the *sp*-hybridization gap centered at about -8 eV which is observed in VB-XPS for the Mn-poor regime as well (Figure 7.4(a)). As it follows from Figure 7.9 (a) the smearing occurs due to Si_{Mn} antisite impurity-like states (Figure 7.10) imposed in the hybridization band-gap.

7.4 Summary and conclusions

Sputter deposition of $Co_2Mn_\alpha Si$ with an additional Mn target may be considered as a promising method to tune the composition of such ferromagnetic layers and thus there electronic structure. This technique provides the possibility to vary the features of the electronic band structure within the valence bands and as a direct consequence the magnetoresistive characteristics of Co_2MnSi based tunnel junctions.

As it follows from present band-structure calculations and comparison with the earlier TMR measurements, the Mn-deficiency regime is the most dangerous for the spin-polarization, since it develops the most destructive mechanism - the Co_{Mn} antisites which impose the electronic states in the half-metallic band gap. This is also reflected in the more sharp spiky structure of measured VB-XPS spectra in the range of -1 to 0 eV. Both present experimental and theoretical results agree with the previous studies and the proposed composition formula.

For the Mn-rich system the rapid loss of the TMR signal for $\alpha > 1.5$ cannot be explained in terms of the calculated spin-polarization, which is reduced only slightly by formation of Mn_{Co} and Mn_{Si} antisites. Theoretically the system remains nearly half-metallic.

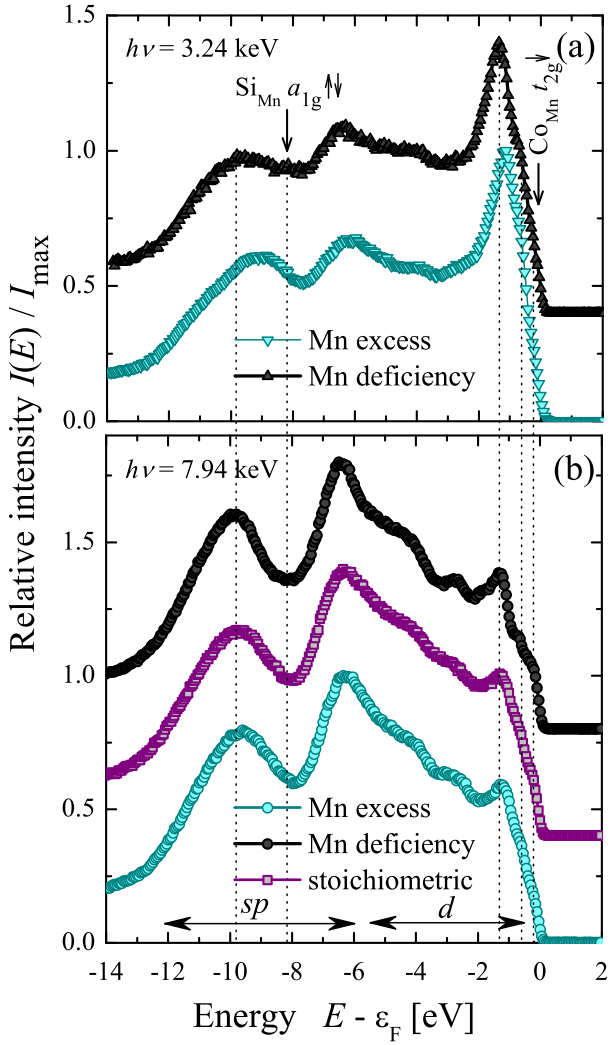

Figure 7.4: Valence band spectra of $Co_2Mn_\alpha Si$ thin films.
The spectra are taken for $\alpha = 0.69$ (Mn deficiency), $\alpha = 1.01$ (stoichiometric) and $\alpha = 1.23$ (Mn excess); Si content is in all cases about 1.0. The excitation energy was set to 3.24 keV in (a) and to 7.94 keV in (b).

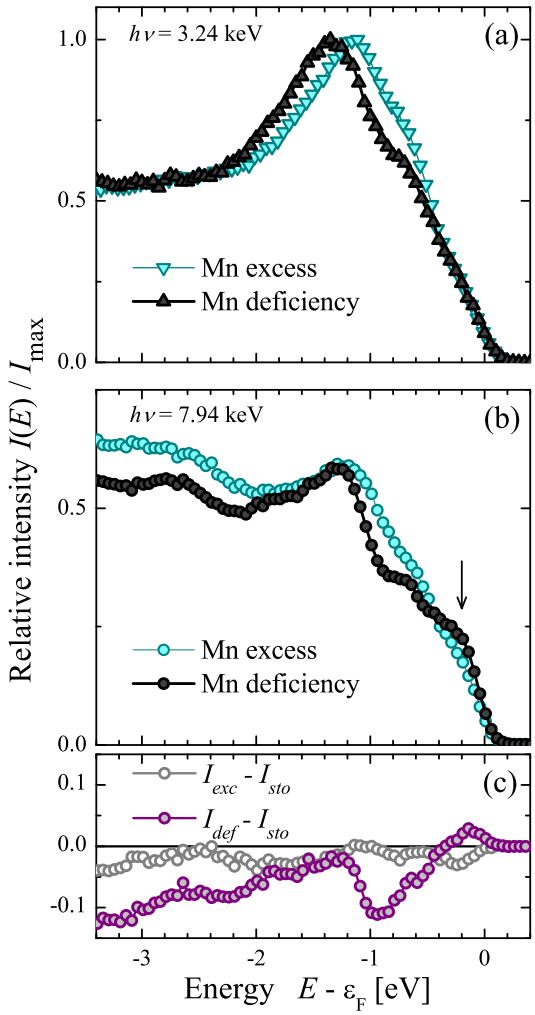

Figure 7.5: Photoelectron spectra of $Co_2Mn_\alpha Si$ films close to εF. The measurements are performed at 3.24 keV (a) and 7.94 keV (b) excitation energies. (c) shows the intensity differences in the spectra of Mn-excess (I_{exc} - I_{sto}) and Mn-deficiency samples ($I_{\mathrm{def}} - I_{\mathrm{sto}}$) with respect to the sample with stoichiometric composition. The differences are calculated for the spectra obtained at 7.94 keV energy.

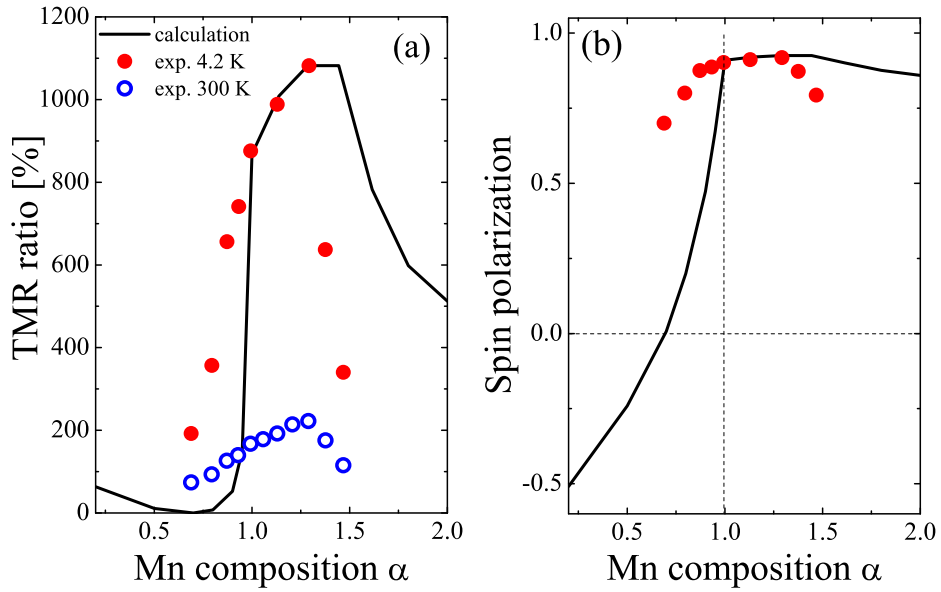

Figure 7.6: (a) The TMR ratio as a function of Mn composition α derived from the calculated spin polarization is compared to the experimentally measured values. (b) Calculated spin polarization as a function of Mn composition α and the spin polarization derived, using Jullière model [6], from experimentally obtained TMR values.

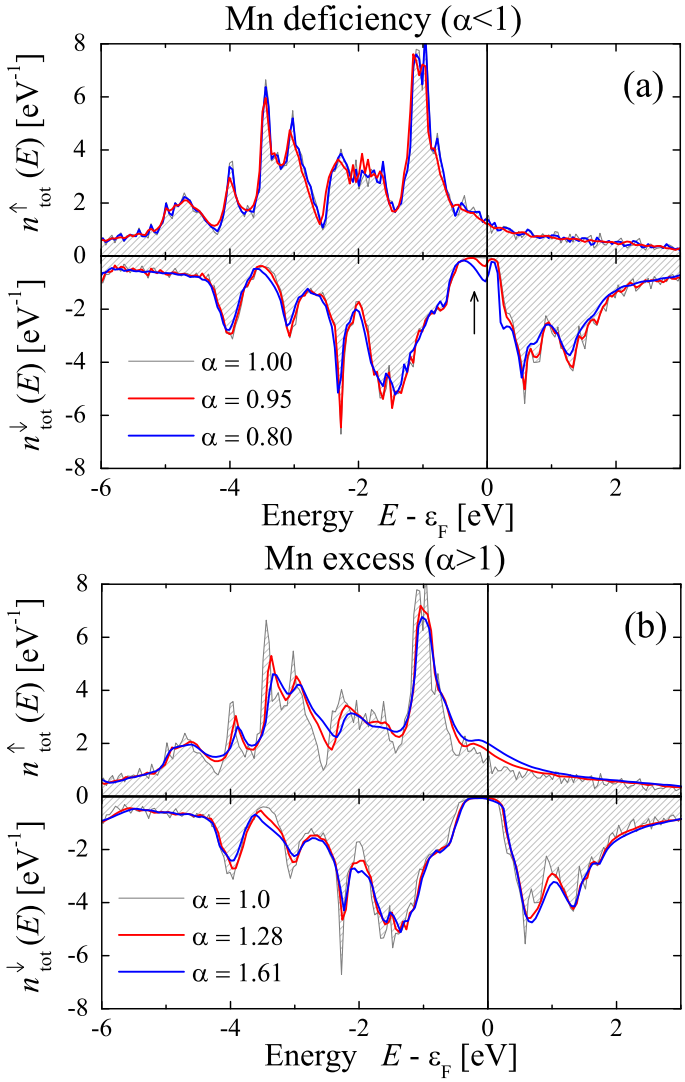

Figure 7.7: Spin-resolved total DOS calculated for (a) Mn-poor ($\alpha < 1$) and (b) Mn-rich ($\alpha > 1$) regimes.

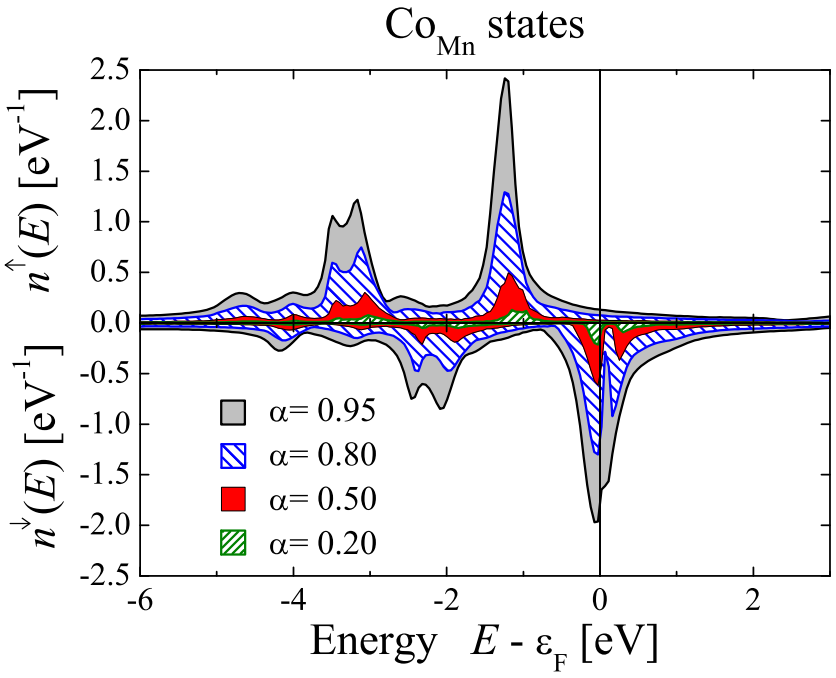

Figure 7.8: DOS of the corresponding Co_{Mn} antisites for $\alpha < 1$ case.

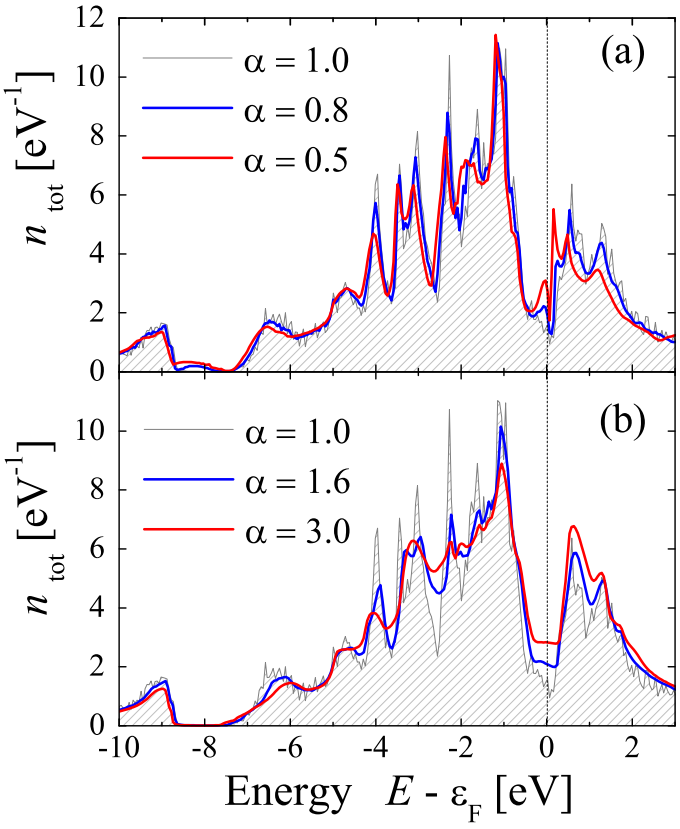

Figure 7.9: Total DOS (sum of both spins) calculated for (a) Mn-poor ($\alpha < 1$) and (b) Mn-rich ($\alpha > 1$) regimes.

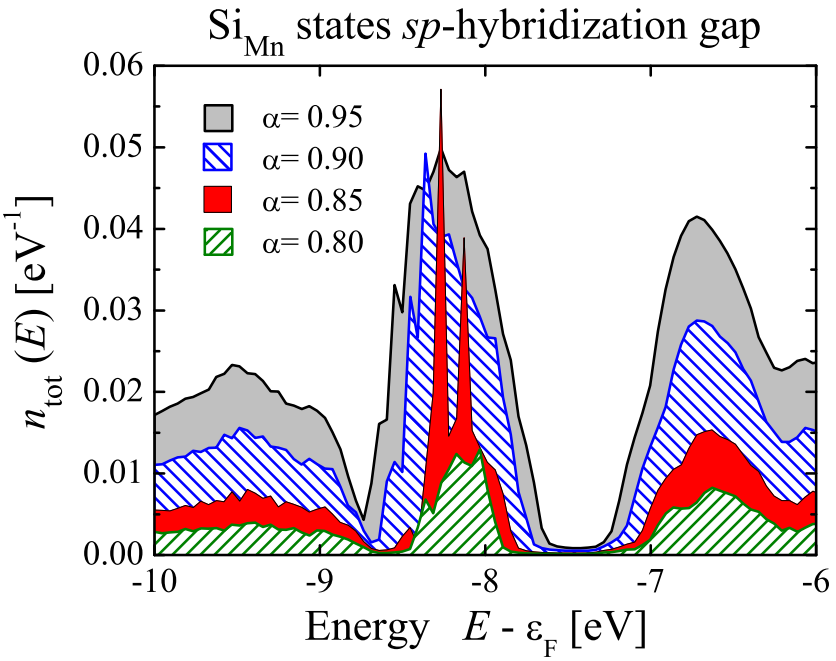

Figure 7.10: Total DOS of Si_{Mn} antisites within the *sp*-hybridization gap for the Mn-poor regime.

8 Magnetic circular dichroism in angular distribution of photoelectrons (MCDAD) from buried layers

8.1 Introduction

Rapid breakthroughs in the area of spintronics have led to the development of electronic devices with improved performance. Being a principal constituent part of such devices, complex multilayer structures have caused considerable interest in exploring their unique properties and at the same time have made this task rather sophisticated. Along with investigation of micromagnetic properties, an improved understanding of magnetoelectronic properties of deeply buried layers and interfaces in magnetic multilayer structures is of the most importance in the viewpoint of their potential applications in the field of magnetic recording, as data storage devices and sensors.

Magnetic circular dichroism (MCD) in photoabsorption and photoemission has become a very powerful tool for the element-specific investigation of the magnetic properties of alloys and compounds. Thus far, such studies have been mainly carried out using soft X-rays, resulting in a rather surface sensitive technique due to the low electron mean free path of the resulting low energy electrons. The application of hard X-rays [99] results in the emission of electrons with high kinetic energies and thus, it increases the probing depth [100]. The bulk sensitivity of this technique was recently proved and for $h\nu > 8$ keV, the bulk spectral weight was found to reach more than 95% [101]. Hard X-ray photoelectron spectroscopy (HAXPES) has been found to be a well-adaptable non-destructive technique for the analysis of chemical and electronic states [65, 102]. It was recently shown that HAXPES can be combined easily with variable photon polarization when using phase retarders [103]. Linear dichroism in the angular distribution of the photoelectrons is achieved using linearly polarized hard X-rays and is succesfully applied to identify the symmetry of valence band states in Heusler compounds [104]. In combination with excitation by circularly polarized X-rays [103], this method will serve as a unique tool for the investigation of the electronic and magnetic structure of deeply buried layers and interfaces.

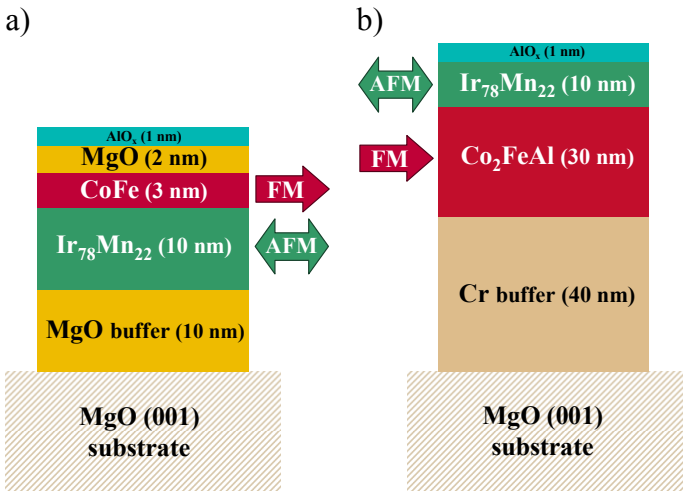

Figure 8.1: Sketch of the exchange-biased films used in the dichroism experiments. The multilayer structure in (a) corresponds to the lower part of the electrode and is realized in on-top configuration with CoFe ferromagnetic layer. The structure shown in (b) presents on-bottom configuration with Co_2FeAl ferromagnetic layer. In both films a 1-nm-thick AlO_x layer is used as a protective cap.

8.2 Samples description

The present study reports on the MCDAD experiment in the HAXPES range on different types of exchange-biased structures with epitaxially grown ferromagnetic layers of CoFe and Co_2FeAl, these being typical materials used in tunnel magnetoresistive devices. (see Figure 8.1) The on-top approach multilayers were deposited in the sequence MgO(100) substrate / MgO buffer layer (10 nm) / $Ir_{78}Mn_{22}$ (10 nm) / CoFe (3 nm) / MgO barrier (2 nm) / AlO_x (1 nm) [105] that corresponds to the lower exchange-biased electrode of a magnetic tunnel junction (MTJ). After growth the stacks were annealed at 350°C for 1 h in vacuum of 5×10^{-2} Pa in a magnetic field of 0.4 MAm^{-1} to provide exchange biasing of the CoFe layer film through the IrMn/CoFe interface (see also [106]). The on-bottom configuration was realized in the multilayer sequence MgO(100) substrate / Cr buffer layer (40 nm) / Co_2FeAl (30 nm) / $Ir_{78}Mn_{22}$ (10 nm) / AlO_x (1 nm) [107]. The sample stacks were annealed at 400°C for 1 h in vacuum under a magnetic field of 0.4 MAm^{-1} to provide exchange biasing to the Co_2FeAl thin film through the Co_2FeAl/IrMn interface (see also [107]). In both cases, the topmost AlO_x layers served as a protective coating. All metal layers were deposited by magnetron sputtering and electron beam evaporation was used to epitaxially grow the MgO barrier. IrMn serves as an exchange-biasing layer that keeps CoFe or Co_2FeAl magnetized in preset directions.

8.3 Results and Discussion

Figure 8.2 shows the $2p$ core-level spectra of Co that were taken from an exchange-biased CoFe film that was covered by oxide films. Pronounced difference was observed in the spectra taken with photons having opposite helicity for a fixed direction of magnetization. The pure difference $\Delta I = I^+ - I^-$ presented in the figure is already free of the influence of the background and gives the correct shape of the magnetic dichroism. That means, it contains all characteristic features of the magnetic dichroism. For quantification and comparison of the dichroic effects, the MCDAD asymmetry was determined from

$$A = \frac{(I^+ - I^-)}{(I^+ + I^-)} = \frac{\Delta I}{2I} \tag{8.1}$$

after subtracting a Shirley-type background from the spectra to find the asymmetry caused only by the direct transition. The background subtraction leads, however, to a very low intensity in the beginning, in the end of the spectral energy range as well as in the range between the spin-orbit split peaks in both spectra (that is in the ranges of the spectra where no signal from the transition itself is expected). This, in turn, leads to very high and rather unphysical values of the calculated asymmetry in these energy ranges. From the above remark on ΔI it is therefore advantageous to show the differences of the intensities and to mark the asymmetry for characteristic energies only. Here the largest obtained asymmetry value is -42% at Co $2p_{3/2}$.

As one can see, the spin-orbit splitting of the Co $2p$ states is clearly resolved, as expected. When going from $p_{3/2}$ to $p_{1/2}$, the dichroism changes its sign across the $2p$ spectra in the sequence: $-++-$; as appears characteristic of a Zeemann-type m_j sublevel ordering. This sequence of signs is directly expected from Equation (4.12) and the state multipoles ρ_{10} given in Table 4.1 when identifying the states of the magnetically split $2p$ doublet as $|j, m_j\rangle$ in the single particle description. The details of the MCDAD reveal, however, that the situation is more complicated. In particular, the dichroism in the Fe $2p$ spectra does not vanish in the region between the spin-orbit doublet. The multiplet formalism to describe the spectra in more detail will be given below.

MCDAD has previously been used to investigate the itinerant magnetism of ferromagnetic elements such as Co, Fe, and Ni, where it was explained in terms of single-particle models [35, 108, 109, 110]. As demonstrated in the case of Ni, however, the single-particle approach poorly describes all the peculiarities of the complex spectra. van der Laan and Thole considered the MCDAD phenomenon by taking into account the influence of electron correlation effects in the frame of atomic many-particle models that were successfully used to describe both localized and itinerant magnetism phenomena [40, 111, 42, 34]. Many-body effects play an important role when using polarized

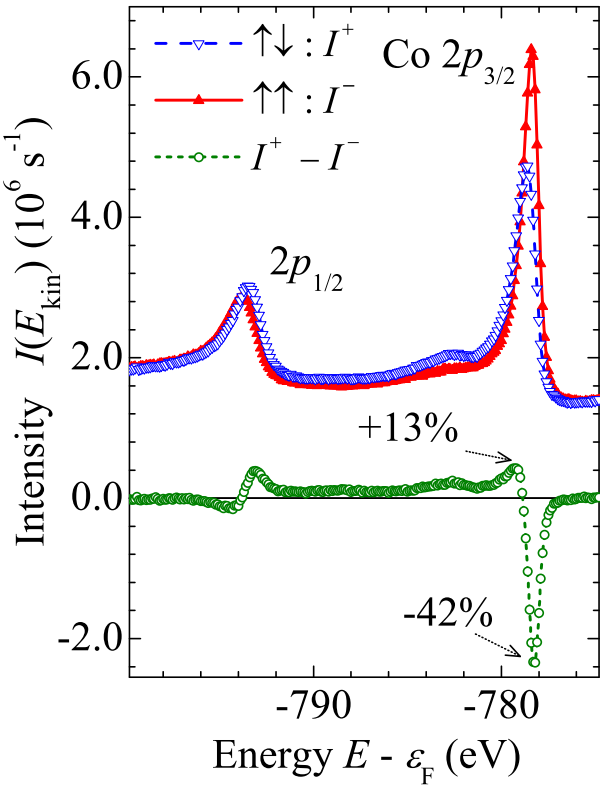

Figure 8.2: Polarization-dependent photoelectron spectra of the Co $2p$ core-level emission from CoFe on top of an IrMn exchange-biasing layer and the difference of two spectra. Asymmetry values are marked at selected energies.

incident photons. The correlation between spin and orbital moments, $2p$ core-hole, and spin-polarized valence band results in a rich multiplet structure that spreads out over a wide energy range of a spectrum [112]. In strongly correlated systems, the bulk magnetic and electronic properties are quite different from the surface ones. However, as observed previously, MCDAD with radiation in the soft X-ray range is highly sensitive to the surface where the dichroism is influenced by symmetry breaking [113]. Because of the strong inelastic electron scattering in this energy range, the escape depth of the photoemitted electrons of a few Å becomes comparable to the thickness of a monolayer. The tuning of the excitation energy also affects the photoionization cross sections. At high energies, the intensities from the d states of transition metals are reduced as compared to the partial cross sections of the s and p states [100, 114, 92]. The shape and magnitude of the asymmetry depend on the partial bulk to surface spectral weights; hence, only at high energies, the dichroism effects appear to be related to the bulk properties.

It was carefully proven that the dichroism vanished in the geometry in which the projection of the photon vector is perpendicular to the magnetization, independently of whether the photon helicity or the magnetization was reversed. This indicates that the films are perfectly magnetized in the direction forced by the exchange-biasing layer magnetization. As an example, Figure 8.3 confirms the absence of the dichroic signal at the Co $2p$ states of the CoFe film in agreement to the theoretical description given above.

Figure 8.4 shows the polarization dependence of the CoFe valence band spectra together with the resulting magnetic dichroism. The MCDAD observed for the valence band is much smaller as compared to the core-level photoemission. The largest asymmetry is approximately -2% at -1 eV below the Fermi energy. Such low asymmetry values were also observed when using low photon and kinetic energies [115]. Only for excitation close to threshold, higher asymmetries arise in the case of one- [116] and two-photon photoemission [117]. In the range of the valence states, the detection is further complicated by the signal from the underlying IrMn layer that does not contribute to the dichroism. Because of the thin layer of CoFe and the large escape depth of the nearly 8 keV fast electrons, the two layers cannot be distinguished in the valence band. It is worthwhile to note that the dichroic signal itself arises exclusively from the buried, ferromagnetic CoFe layer.

For studies aimed toward the development of novel devices, it is necessary to also detect the magnetic signal from deeply buried layers. To prove the reliability of the proposed method, experiments were also performed on samples in which the IrMn exchange-biasing layer was on top of the layer structure.

Figure 8.5 compares the MCDAD results for the shallow core levels of CoFe in the on-top configuration (a) and the deeply buried Co_2FeAl in the on-bottom configuration

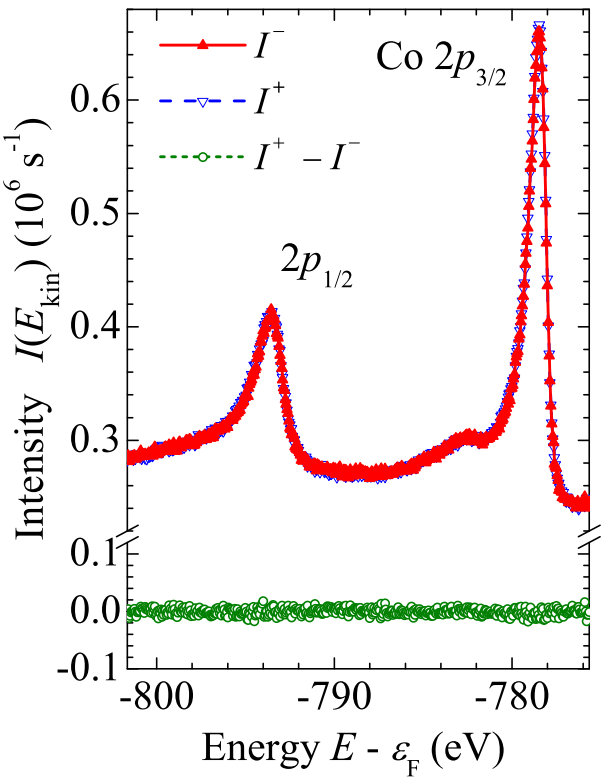

Figure 8.3: Illustration of the vanishing dichroism in photoemission when the photon polarization vector is perpendicular to the in-plane magnetization vector demonstrated for the Co $2p$ state of CoFe. Shown are the photoelectron spectra I^+, I^- and their difference $I^+ - I^-$ obtained with different helicity at fixed magnetization perpendicular to the photon beam.

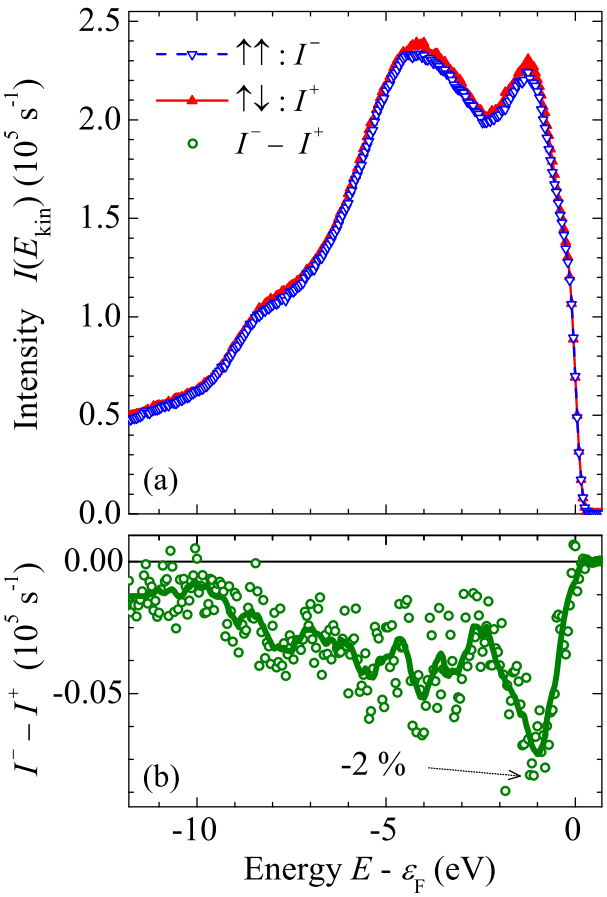

Figure 8.4: MCDAD in valence band of CoFe on top of IrMn.
The asymmetry is given at -1 eV below Fermi level.

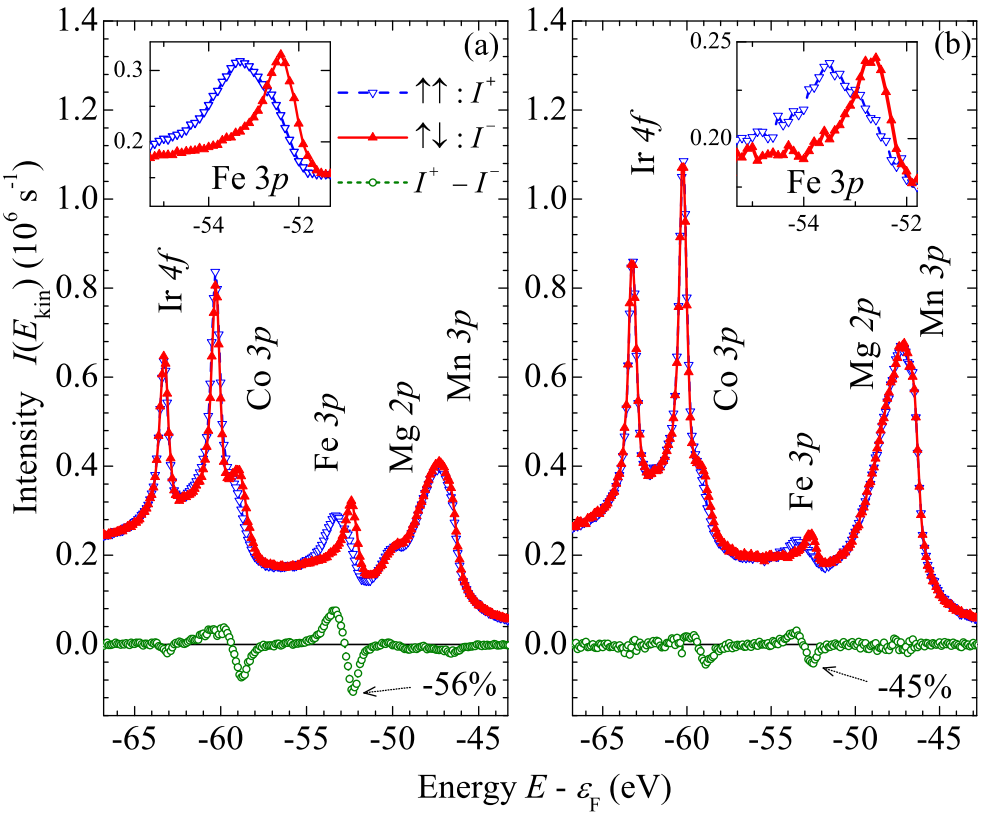

Figure 8.5: MCDAD for the shallow core level spectra obtained from the buried CoFe on top and Co_2FeAl beneath a 10-nm-thick IrMn film. The insets show an enlarged view of I^+ at the Fe 3p states.

beneath a 10-nm-thick IrMn film (b). For such complex multilayer structures, the situation becomes complicated in that the signals from all the elements contained in the system are detected. In both cases the shallow core levels of all elements of the multilayers are detected. The intensity differences between Fe and Co 3p emission or Ir 4f and Mn 3p in the different configurations are obvious and arise from the damping of the intensity when the electrons pass through the layers above the emitting layer. Strong signals are still detected from the buried elements even though the ferromagnetic Co_2FeAl layer lies 10 nm beneath the antiferromagnetic IrMn layer, as it is clearly seen in the inset of Figure 8.5(b). A large asymmetry is clearly observed at the Co and Fe signals, and these are the ones responsible for the ferromagnetic properties of the system. The asymmetries of -56% (CoFe) and -45% (Co_2FeAl) in the Fe 3p signal are quite evident. In Co 3p, it is well detected even though the direct spectra overlap with the Ir 4f states.

Figure 8.6 shows the polarization dependent HAXPES spectra and the MCDAD at the Fe 2p states of the buried CoFe (a) and Co_2FeAl (b) layers. The multiplet splitting at the Fe $2p_{3/2}$ is very well resolved and the MCDAD is well detected in both materials.

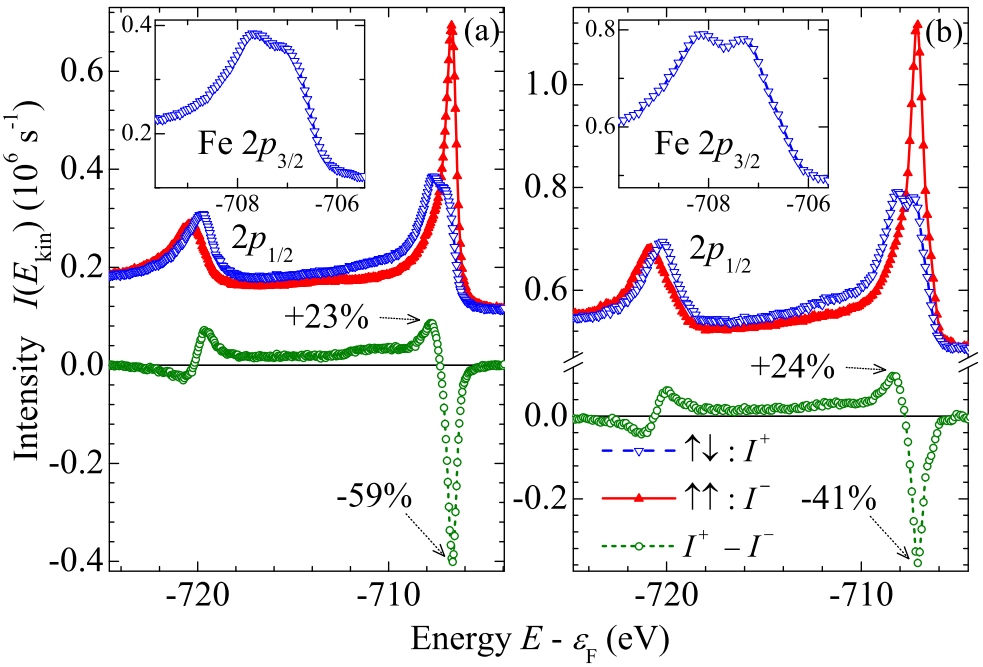

Figure 8.6: Polarization-dependent photoelectron spectra of the Fe $2p$ core-level emission from CoFe on top of an IrMn exchange-biasing layer, Co_2FeAl beneath IrMn and the corresponding differences of the spectra taken with the opposite helicity of light. Asymmetry values are marked at selected energies. The insets show an enlarged view of I^+ at the Fe $2p_{3/2}$ states in both cases.

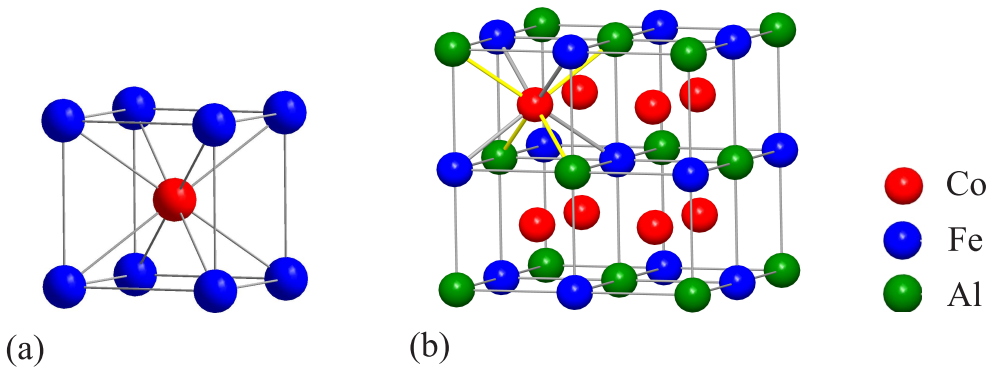

Figure 8.7: The crystal structure of CoFe (a) and Co_2FeAl (b).

The emission from the Co_2FeAl has a lower intensity and the resolution was therefore reduced to 250 meV in order to keep the counting rates comparable to those of the CoFe measurements. (Note that this does not influence the spectra much as they are governed by a lifetime broadening that is in the same order of magnitude.) It was shown [118] that linear magnetic dichroism (LMDAD) along with the circular one can be successfully applied to investigate the electronic and magnetic properties of surfaces and interfaces. The LMDAD asymmetry observed at Fe $2p_{3/2}$, however, was only at most -9% for a low excitation energy. In our studies the maximum asymmetries are -59% for CoFe and - 41% for Co_2FeAl at Fe $2p_{3/2}$, and this is ideal for the analysis of the magnetic properties.

A closer inspection to the MCD spectra (see insets of Figures 8.6 (a) and (b)) revealed a striking distinction between the Fe $2p$ spectra of the two layer systems. Even though taken with a slightly lower resolution, the multiplet splitting of the Fe $2p_{3/2}$ emission from Co_2FeAl appears more pronounced as compared to the corresponding spectrum from CoFe. The mean splitting ΔE of the Fe $2p_{3/2}$ states is 0.8 eV and 1.0 eV for CoFe and Co_2FeAl, respectively. Co_2FeAl is supposed to be a half-metallic ferromagnet with a magnetic moment of 5 μ_B in the primitive cell and about 2.8 μ_B per Fe atom [119], whereas CoFe is a regular band ferromagnet with a very high magnetic moment (about 2.5 μ_B at Fe) [120]. In both cases the Fe moment is clearly above that of pure Fe (2.1 μ_B). One of the major differences is the localized magnetic moment of Fe in Co_2FeAl that is caused by a strong localization of the t_{2g} bands. In the ordered case of both compounds, the Fe atoms are in a cubic environment and are surrounded by 8 Co atoms, as it is demonstrated in Figure 8.7(a) and (b). Co_2FeAl forms a perfect 2^3 CsCl supercell with every second Fe atom of CoFe replaced by Al 8.7(b). This causes additional Co-Al bonds that reduce the Co-Fe d-state overlap. The result is a localized moment at the Fe sites. From this viewpoint, Fe in Co_2FeAl is in closer to an covalent than a metallic state. For the Fe atoms, this causes a more pronounced interaction of the core hole at the ionized $2p$ shell with the partially filled $3d$ valence shell.

As mentioned above, the single particle theory is not capable to explain the details of the spectra and their dichroism. It is necessary to respect the coupling between the ionized core and open valence shells. In the present case this is the interaction between the $2p^5$ core hole and the open $3d$ valence shell of Fe. Therefore, multiplet calculations were carried out to explain the experimentally obtained results for the two different materials. They were performed by means of CTM4XAS 5.2 (Charge Transfer Multiplet Calculations for X-ray Absorption Spectroscopy) program [121], using its X-ray photoelectron spectroscopy (XPS) option. The results are shown in Figure 8.8. The simulations were made for a Fe^{3+} ionic ground state with $4s^0 3d^5$ configuration that describes well the emission from the Fe-$2p$ states of both systems, CoFe and Co_2FeAl. The Slater integrals (F_{dd}, F_{pd}, and G_{pd}) were reduced to 0.65; 0.55; 0.65 and 0.7; 0.5;

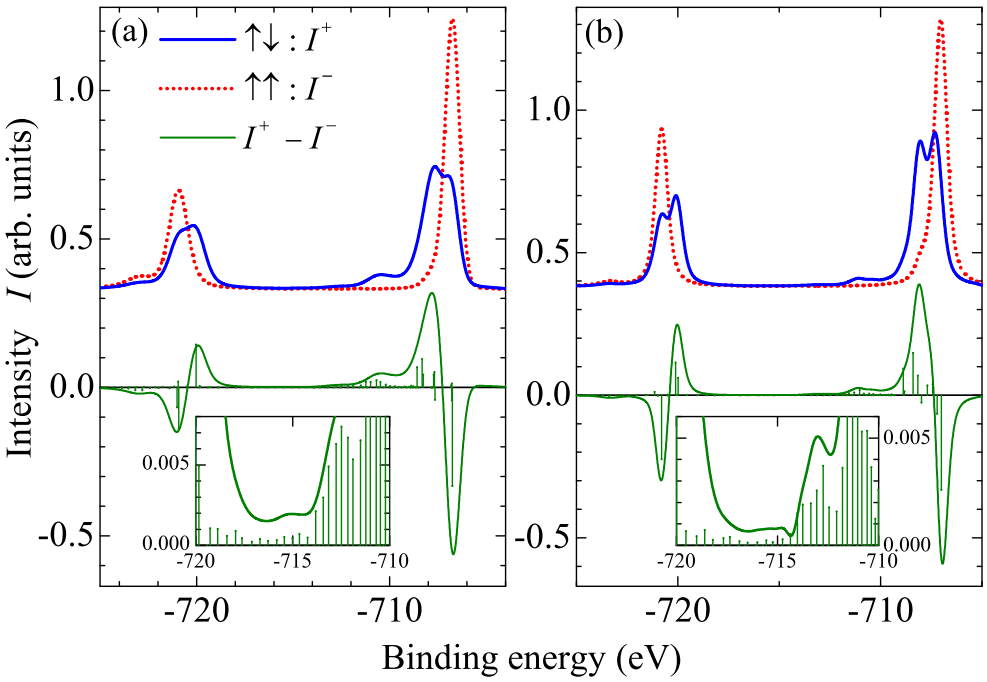

Figure 8.8: Calculated polarization-dependent photoelectron spectra of the Fe $2p$ core-level emission obtained by means of atomic multiplet calculations and their difference for CoFe (a) and Co_2FeAl (b). The insets show the enlarged views of the difference curve in the region between spin-orbitally splitted components of Fe $2p$ states. The bars mark the multiplet states.

0.5 of the free atom values to describe the spectra of CoFe and Co_2FeAl, respectively. As exchange interaction plays an important role in ferromagnetic materials, the effect of exchange splitting was taken into account by setting the magnetic splitting parameter M to 50 meV for CoFe and 450 meV for Co_2FeAl. The obtained values for the splitting ΔE of the Fe $2p_{3/2}$ states are 0.9 eV and 1.1 eV for CoFe and Co_2FeAl, respectively. The applied parameters resulted in a quite good agreement between calculated and experimental spectra and dichroism . Possible, slight disagreements may be attributed to the fact that the observed spectra depend on the degree of localization or itineracy of the magnetic moment at the Fe site through the coupling of the $2p^5$ core hole with the d valence bands. Fractional d state occupancies (for example d^{5+x}, $0 < x < 1$) that might better describe the partial delocalization of d electrons of Fe in metallic systems, however, are not available in the atomic model. The insets in Figure 8.8 present a enlarged view of the region of the dichroism between the main lines of the multiplet. In those insets one clearly recognizes the appearance of multiplet states over the entire energy range. These states form the characteristic structure of the dichroism that is in a good agreement with the experiment.

It is worthwhile to note that such differences between two very similar alloys are not resolved by X-ray circular dichroism (XMCD) in soft X-ray photo absorption [122, 123]. This is found easily if comparing the here shown photoelectron spectra and dichroism to previously reported XMCD spectra of Fe containing Heusler compounds [124, 125, 126, 127, 119, 128] were the XMCD spectra and dichroism appear rather without any resolved splitting of the $L_{2,3}$ lines.

8.4 Summary and conclusions

In summary, MCDAD in hard X-ray photoelectron spectroscopy was used to study the magnetic response of the core level of buried, remanently magnetized layers. Using bulk-sensitive HAXPES-MCDAD, it was shown that IrMn exchange-biasing layers keep thin films of CoFe or Co_2FeAl remanently magnetized in a well- defined direction. Dichroism in the valence band spectroscopy is complicated in metal/metal layers; however, the situation will improve in metal/insulator structures in which the insulator does not contribute to the states at the Fermi energy [65]. The magnetic dichroism from core levels, including shallow core levels, of CoFe and buried Co_2FeAl multilayer has asymmetries up to above 58% when it is excited by circularly polarized hard X-rays and is thus much larger as compared to that in the case of excitation by soft X-rays. As a noteworthy result, the differences in the Fe $2p$ emission from a regular ferromagnet (CoFe) and a suggested half-metallic ferromagnet (Co_2FeAl) were demonstrated. The splitting observed in Co_2FeAl points on the covalent character of the compound.

Overall, the high bulk sensitivity of HAXPES combined with circularly polarized

photons will have a major impact on the study of the magnetic phenomena of deeply buried magnetic materials. The combination with recently proposed standing wave methods [26, 129] will allow an element-specific study of the magnetism of buried layers and make feasible the investigation of the properties of magnetic layers not only at the surface but also at buried interfaces.

9 Spin polarimetry and MCDAD from buried layers

9.1 Introduction

Spin-resolved exploration of the electronic structure of buried ferromagnetic layers and interfaces is of a great importance. It is needed for the selection of optimal materials for spintronic devices. For example, the efficiency of magnetic tunnel junctions (MTJs) is largely defined by the spin dependent electronic properties of half-metallic electrode materials [20, 76] employed.

Hard X-ray photoelectron spectroscopy (HAXPES) was proven to be a bulk sensitive probe of the electronic band structure [100, 65]. A rather high bulk sensitivity of this technique results from the large inelastic mean free path (10-20 nm) of high- energy photoelectrons (6-10 keV) and allows to explore the electronic band structure of buried layers and interfaces. This work presents results of an extension of a HAXPES experiment with a spin polarimeter implemented at BL47XU beamline (SPring-8, Japan). This combination facilitates complete studies of the electronic band structure on buried layers resolving electron energy, momentum and spin degrees of freedom.

Presently available spin detection techniques are based on the spin dependence in electron scattering and diffraction originating from spin-orbit interaction or exchange scattering. Spin resolved photoelectron emission studies were performed up to now for photoelectrons with kinetic energies in the UPS / XPS range (< 2 keV) implying a high surface sensitivity. Implementation of spin detection in a bulk sensitive spin-resolved HAXPES experiment implies rather strong requirements on the electron focusing system and conditions of a high potential within the spin detecting system. This is crucial for the case of low energy electron scattering at the electron scattering type spin analyzers. Photoelectron spin polarization analysis is hampered by a strong reduction of intensity at the spin discriminating stage by 3 orders of magnitude. In combination with the low photoionization cross sections at high kinetic energies [100, 92, 27] this leads to low countrates.

Related information on the majority and minority spin character of the electronic states may also be revealed in magnetic linear and circular dichroism in X-ray absorption [130] and photoelectron emission [30, 34]. Magnetic dichroism phenomena in

photoelectron emission exemplify a preferential interaction of polarized X-rays with electrons of a particular spin direction defined by the experimental geometry. They allow also to elucidate a spin splitting in core multiplet states [131] due to the exchange interaction of the core hole with the spin-polarized bands of the valence electrons. The present studies involve a comparative analysis of spin resolved photoelectron spectra together with data on magnetic circular and linear dichroism in angular distribution (MCDAD, MLDAD) in photoelectron emission.

9.2 Samples description

The experiment has been performed on an exchange-biased $Co_2FeAl_{0.5}Si_{0.5}$ (CFAS) thin films shown to be a half-metallic Heusler compound with a high spin polarization exhibiting the lowest temperature dependence among the known half-metals [132]. CoFe(10 nm) / $Ir_{22}Mn_{78}$(10 nm) / CoFe(0.5 nm) / CFAS(15 nm) / MgO(2 nm) / AlO_x(1 nm) multilayers were deposited on a MgO(100) substrate. An exchange bias field of 12 kAm^{-1} was applied for the in-plane magnetization by in-vacuum annealing of the multilayer stack at 300°C followed by cooling in a magnetic field of 400 kAm^{-1}.

The spin polarized electronic states of buried magnetic layers were studied with special emphasis on the bulk sensitivity of HAXPES and the correlation of the spin resolved spectra with magnetic linear and circular dichroism in photoelectron emission from a CFAS layer buried under a 3 nm protective coating. The results are discussed in terms of a multiplet model explaining the magnetic dichroism in photoelectron emission.

9.3 Results and Discussion

Fig. 9.1 shows the spin resolved spectra of the Fe $2p_{3/2}$ state upon excitation with p-polarized 5.95 keV photons. A maximum polarization of about 50% is obtained after background subtraction according to the equation refeq:polarization.

$$P = \frac{1}{S}\frac{(N_1 - N_2)}{(N_1 + N_2)}, \tag{9.1}$$

with $N_{1,2}$ denoting the countrates in the spin detector channels and the Sherman function S being set to 0.25 [50]. The spectra for majority and minority spin were determined from:

$$I_{\uparrow,\downarrow} = I_{total}\,(1 \pm P)\,/2. \tag{9.2}$$

For details on the spin polarization detection see Refs. [47, 44].

The structure of the Fe $2p_{3/2}$ m_j multiplet (shown as bars in Fig. 9.1c) was taken from the band structure calculation of $Co_2FeAl_{0.5}Si_{0.5}$ performed by the fully relativistic

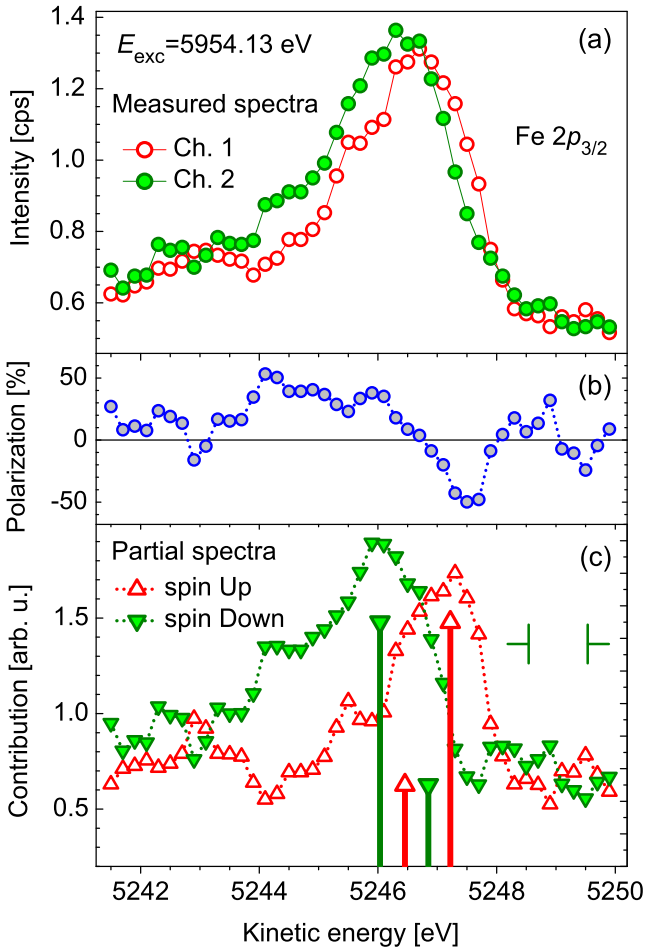

Figure 9.1: Countrates in the spin detector channels (a), spin polarization (b) and spin-resolved spectra of Fe $2p_{3/2}$ photoelectrons (c) from the buried CFAS layer. The energy resolution interval (1 eV) is shown with the vertical slit mark.

KKR Green's function method (SPR-KKR) [66]. The bars topped with filled and hollow triangles depict the states with negative and positive spin projection m_s values; the larger and smaller bars correspond to the $|m_j|$=3/2 and $|m_j|$=1/2 states, respectively. The sub-states of the $2p_{3/2}$ core electrons with well defined spin up (m_j=3/2; m_s=+1/2) and spin down (m_j=-3/2; m_s=-1/2) are clearly reproduced by maxima in the spin-resolved spectra (Fig. 9.1c). The electron spin (m_s) is not well defined for $2p_{3/2}$ states with $m_j = \pm 1/2$ since the respective m_j values ($m_j = m_l + m_s$) may be obtained with different m_l and m_s combinations. The $2p_{3/2}$ state with m_j=-1/2 is, however, revealed as a shoulder in the spin down component. Thus, the features of Fe $2p_{3/2}$ core states are well reproduced in the measured spin resolved spectra showing a good agreement with the one-step model of photoelectron emission.

One should however note the broadening of the measured spin resolved spectra. This broadening may originate from a relatively poor resolution of the spin resolved measurements, but this is not the only reason. After electron escape from the Fe $2p$ orbital, the coupling of the $2p^5(^2P_{3/2})$ core hole with $3d^5(^6S_{5/2})$ valence electrons results in a variety of ionic $^{7,5}P_{|L+S|\geq J\geq|L-S|}$ configurations (see Ref. [133] for details). The difference in the energy levels of the ionic states implies a broad kinetic energy distribution for the emitted electrons and broadening of the photoemission spectra, particularly at the side of higher binding energies [134].

Fig. 9.2 shows the correlation between spin resolved spectra and magnetic circular as well as linear dichroism. Magnetic circular dichroism (MCDAD) in photoelectron emission (acceptance angle of $\pm 7^\circ$ tilted by 2° with respect to the sample surface normal) was measured with the helicity vector $\vec{\sigma}$ of circularly polarized 7.94 keV photons directed nearly parallel (σ^+) and antiparallel (σ^-) to the magnetization vector $\vec{M}$ of the in-plane magnetized sample. A maximal MCDAD value of 45% has been reached for the Fe $2p_{3/2}$ photoelectrons from the CFAS layer. The 1.3 eV gap between the maxima of the spin resolved spectra agrees well with the exchange splitting revealed by MCDAD measurements. Such a relatively large exchange splitting proves the magnetic moment to be localized at the Fe sites in CFAS. The extrema of the MCDAD signal show a slight shift to higher binding energies as compared with the maxima of the spin resolved peaks.

Magnetic linear dichroism (MLDAD) was measured with s-polarized photons (7.94 keV) and the sample magnetization along or perpendicular to the $\vec{E}$ vector of the X-rays. The MLDAD signal changes its sign around 706.8 eV (Fig. 9.2b) where the "minority" signal in the spin resolved spectra starts to increase. The MLDAD shows a well pronounced negative asymmetry with 12% amplitude in the range of the Fe $2p_{3/2}$ state with the spin of minority sign. The higher probability for the emission of the Fe $2p$ electron with minority spin (as it is recognized for $\vec{M}\|\vec{E}$, Fig. 9.2c) is caused by the higher probability for coupling of the Fe $2p^5$ hole with Fe $3d^5$ electrons resulting in

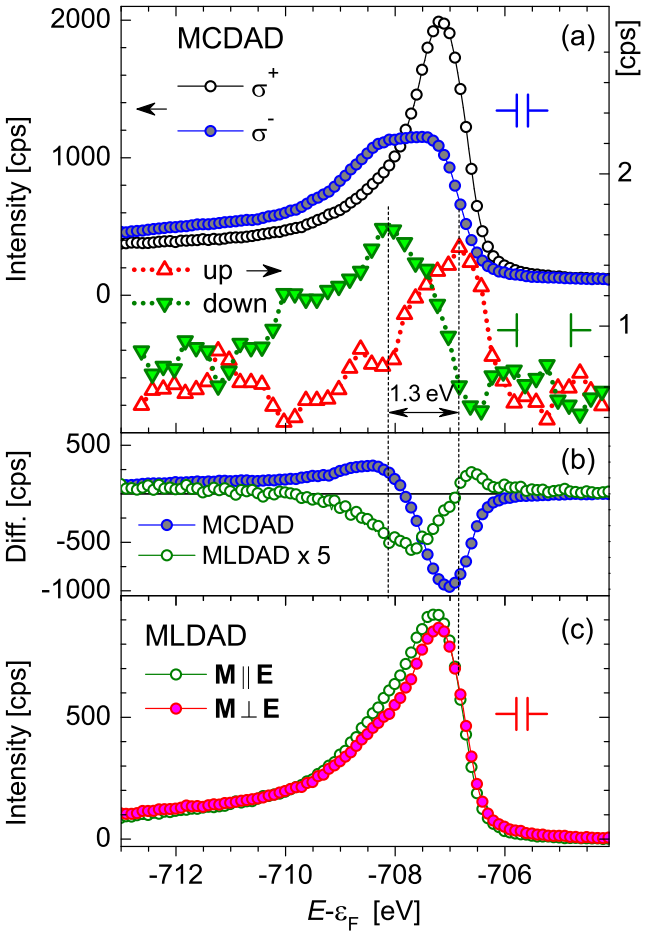

Figure 9.2: Comparison of spin-resolved Fe $2p_{3/2}$ spectra with MCDAD and MLDAD for photoelectron from a buried CFAS layer. The corresponding energy resolution intervals are shown with the vertical slit marks.

the state with maximal majority spin. Thus, the magnetic dichroism in photoelectron emission elucidates the spin-polarized electronic states and allows to recognize the spin sign relatively to the majority d states of the valence band. MLDAD measurements show a higher intensity for the electrons with minority spin when the magnetization vector $\vec{M}$ is aligned parallel to the $\vec{E}$ vector of the photons.

9.4 Conclusions

In summary, a spin resolved HAXPES experiment has been successfully performed on a buried magnetic layer. The implemented Spin-HAXPES technique facilitates the direct observation of spin polarization of emitted electrons. The measurements prove that a spin polarization of about 50% is retained during the transmission of the photoelectrons emitted from the Fe $2p_{3/2}$ state through a 3 nm thick oxide capping layer. The reported spin resolved spectra agree well with the magnetic circular and linear dichroism. The informations from spin polarization and magnetic dichroism are different and their combination provides a detailed insight into the dynamics of photoemission from a ferromagnetic material. The reported experiment paves the way to spin-resolved spectroscopy of buried layers and buried interfaces, issues being inaccessible by the classical low energy approach.

The magnetic states can be elucidated from the magnetic dichroism measurements providing much higher detecting efficiency [133] than achieved in spin resolved measurements with a spin detector. However, this does not exclude the necessity in direct spin resolved measurements with spin detectors since the technique of spin polarized state restoration from MCDAD and MLDAD is not well established.

10 Conclusions and outlook

This work is focused on investigation of electronic structure, magnetic properties, magnetic ordering and spin-resolved electronic structure of a number of ferromagnetic and half-metallic ferromagnetic materials used as functional layers in complex multilayer structures by means of hard x-ray photoelectron spectroscopy and techniques based on it.

Recently the highly increasing demand of the worldwide market in new computer technologies has trigged a great scientific interest in investigations and design of advanced materials that can be implemented in the novel spintronic devices. The performance of of such devices depends on the quality of the produced magnetoresistive structures as well as on the intrinsic magnetic properties of the materials employed in such devices. Therefore it is extremely important from fundamental and technological point of view to investigate the electronic structure of these materials responsible for their unique properties.

Photoelectron spectroscopy is a widely used technique for probing the chemical composition and electronic structure of materials. An important experimental parameter of photoemission is its probing depth. Spintronic devices are nanometer-scale multilayer structures where the functional magnetic layers are deeply buried. Unfortunately in standard laboratory conditions we are restricted in this parameter that makes bulk materials and buried layers inaccessible for non-destructive investigation. To overcome this drawback nowadays we can use high intense X-ray sources such as synchrotron facilities that extend the common photoelectron spectroscopy to the hard x-ray regime. The application of hard x-rays increases the inelastic mean free path of the emitted electrons within the solid and thus makes hard x-ray photoelectron spectroscopy (HAXPES) a bulk sensitive nondestructive probe for solid state research. The HAXPES studies were performed on Ta-CoFeB-MgO-CoFeB-Ta multilayer structures that are characterized by huge TMR ratios of more than 600% reached during the annealing process. The enforced diffusion of B from the CoFeB into the adjacent Ta layer upon increasing of annealing temperature was revealed by core-level spectroscopy. Dramatic changes close to the Fermi edge are observed that are in a good agreement with ab-initio calculations and can be attributed to the removal of B from the system. The dependence of the tunnelling magnetoresistance on the annealing temperature is explained by the combined effects of an improved crystalline structure together with a change in the spin

polarization at the Fermi energy caused by the removal of boron from the CoFeB layer and Ta diffusion at high annealing temperature.

Being half-metallic ferromagnets (HMFs) many of the Co_2 based Heusler compounds are widely used as electrodes in tunnelling magnetoresistance (TMR) devices due to their distinctive transport properties that provide a perfect spin-polarized electrical current. This behaviour of the Heusler compounds is determined by their intrinsic electronic structure in the vicinity of the Fermi energy (ε_F) where it is completely spin-polarized. The valence states of buried off-stoichiometric $Co_2Mn_\alpha Si$ thin films were investigated by high resolution hard x-ray photoelectron spectroscopy. The dependence of the TMR ratio upon changes of α is explained by the changes in the electronic structure near the Fermi energy with varying Mn content α. The results are in good agreement with the performed *ab-initio* calculations. Sputter deposition of $Co_2Mn_\alpha Si$ with an additional Mn target is proven to be a promising method to tune the composition of such ferromagnetic layers and thus their electronic structure.

Along with investigation of electronic structure an improved understanding of magnetoelectronic properties of deeply buried layers and interfaces in magnetic multilayer structures is of highest importance in the viewpoint of their potential applications as components in spintronic devices. Magnetic circular dichroism (MCD) in photoabsorption and photoemission has become a very powerful tool for the element-specific investigation of the magnetic properties of alloys and compounds. In combination with hard x-rays this method serves as a unique tool for the investigation of the electronic and magnetic structure of deeply buried layers and interfaces. The measurement of magnetic dichroism in angular-resolved hard x-ray photoemission (HAXPES-MCDAD) were performed on Co_2FeAl and CoFe in-plane magnetized buried layers with IrMn exchange-biasing layer on top or below ferromagnetic layer, respectively. A pronounced magnetic dichroism is found in the Co and Fe $2p$ states of both materials. It was shown that IrMn exchange-biasing layers keep thin films of CoFe or Co_2FeAl remanently magnetized in a well-defined direction. The localization of the magnetic moments at the Fe site conditioning the peculiar characteristics of the Co_2FeAl Heusler compound, predicted to be a half-metallic ferromagnet, is revealed from the magnetic dichroism detected in the Fe $2p$ states. The experimentally obtained results are shown to be in good agreement with multiplet calculations performed.

Thus the magnetoresistive characteristics of magnetic tunnel junctions are the key point in obtaining high performance in spintronic devices, the spin dependent electronic properties are of high importance in searching and selecting of constituent materials used as electrodes in tunnel junctions. Thus, the direct nondestructive element-specific spin-resolved measurements of the electronic structure are of great desire for investigation of such complex multilayer systems employed widely in spintronics. A first spin-resolved HAXPES (spin-HAXPES) experiment using a spin polarimeter of the

SPLEED-type has been successfully performed on a buried $Co_2FeAl_{0.5}Si_{0.5}$ magnetic layer. The measurements proved that a spin polarization of about 50% is retained during the transmission of the photoelectrons emitted from the Fe $2p_{3/2}$ state through a 3-nm-thick oxide capping layer. The reported spin resolved spectra agree well with the magnetic circular and linear dichroism. The information from spin polarization and magnetic dichroism are different and their combination provides a detailed insight into the dynamics of photoemission from a ferromagnetic material. The performed experiment paves the way to spin-resolved spectroscopy of buried layers and buried interfaces, issues being inaccessible by the classical low energy approach.

List of Abbreviations

PES	photoelectron spectroscopy
HAXPES	hard x-ray photoelectron spectroscopy
MTJ	magnetic tunnel junction
MR	magnetoresistance
GMR	giant magnetoresistance
AFM	antiferromagnetic (antiferromagnet)
FM	ferromagnetic (ferromagnet)
Sy-AFM	synthetic antiferromagnet
SV	spin valve
EB-SV	exchange-biased spin valve
RT	room temperature
TMR	tunnel magnetoresistance
DOS	density of states
XPS	x-ray photoemission spectroscopy
SR	synchrotron radiation
LEED	low energy electron diffraction
SPLEED	spin polarized low energy electron diffraction
MLDAD	linear magnetic dichroism in the angular distribution of electrons
MCDAD	circular magnetic dichroism in the angular distribution of electrons
MCD	circular magnetic dichroism
XMCD	x-ray magnetic circular dichroism

UPS	ultra-violet photoelectron spectroscopy
DLD	delayline detector
SP	spin polarization
CPA	coherent potential approximation
LSDA	local density approximation
VB	valence band

List of Figures

List of Tables

Bibliography

[1] P. Grünberg, R. Schreiber, Y. Pang, M. B. Brodsky, and H. Sowers. *Phys. Rev. lett.*, 57:2442, 1986.

[2] M. N. Baibich, J. M. Broto, A. Fert, F. Nguyen van Dau, F. Petroff, P. Etienne, G.Creuzet, A. Friederich, and J. Chazelas. *Phys. Rev. lett.*, 61:2472, 1988.

[3] C. Chappert, A. Fert, and F. Nguyen van Dau. *Nat. Mat.*, 6:813, 2007.

[4] S. A. Wolf, D. D. Awschalom, R. A. Buhrman, J. M. Daughton, S. von Molnár, M. L. Roukes, A. Y. Chtchelkanova, and D. M. Treger. *Science*, 294:1488, 2001.

[5] W. H. Butler. *Sci. Technol. Adv. Mater.*, 9:014106, 2008.

[6] M. Jullière. *Phys. Lett.*, 54A:225, 1975.

[7] T. Miyazaki and M. Tezuka. *J. Magn. Magn. Mater.*, 139:L231–L234, 1995.

[8] J. S. Moodera, L. R. Kinder, T. M. Wong, and R. Meservey. *Phys. Rev. Lett.*, 74:3273, 1995.

[9] R. Meservey and P. M. Tedrow. *Phys. Rep.*, 238:173, 1994.

[10] S. S. P. Parkin *etal*. *Proc. IEEE*, 91:661, 2003.

[11] S. Yuasa, T. Nagahama, A. Fukushima, Y. Suzuki, and K. Ando. *Nat. Mater.*, 3:868, 2004.

[12] S. Yuasa, A. Fukushima, T. Nagahama, K. Ando, and Y. Suzuki. *Jpn. J. Appl. Phys.*, 43-4B:L588, 2004.

[13] S. S. P. Parkin, C. Kaiser, A. Panchula, P. M. Rice, B. Hughes, M. Samant, and S.-H. Yang. *Nat. Mat.*, 3:862, 2004.

[14] S. Yuasa and D. D. Djayapravira. *J. Phys. D: Appl. Phys.*, 40:R337–R354, 2007.

[15] W. H. Butler, X.-G. Zhang, and T. C. Schulthess. *Phys. Rev. B*, 63:054416, 2001.

[16] J. Mathon and A. Umerski. *Phys. Rev. B*, 60:1117, 1999.

[17] P. H. Dederichs, Ph. Mavropoulos, O. Wunnicke, N. Papanikolaou, V. Bellini, R. Zeller, V. Drchal, and J. Kudrnovský. *J. Magn. Magn. Mater.*, 240:108, 2002.

[18] F. Heusler, W. Starck, and E. Haupt. *Verh DPG*, 5:220, 1903.

[19] F. Heusler. *Verh DPG*, 5:219, 1903.

[20] J. Kübler, A. R. Williams, and C. B. Sommers. *Phys. Rev. B*, 28:1745–1755, 1983.

[21] Y. Sakuraba, M. Hattori, M. Oogane, Y. Ando, H. Kato, A. Sakuma, T. Miyazaki, and H. Kubota. *Appl. Phys. Lett.*, 88:192508, 2006.

[22] H. Hertz. *Annalen der Physik und Chemie*, 267:983, 1887.

[23] S. Hüfner. *Photoelectron spectroscopy. Principles and applications.* Springer, Berlin-Heidelberg, 2003.

[24] C. S. Fadley. Academic Press, London-New York-San Francisco, 1978.

[25] S. Tanuma, C. J. Powell, and D. R. Penn. *Surf. Interface Anal.*, 43:689–713, 2011.

[26] C. S. Fadley. *J. Electron Spectrosc. Relat. Phenom.*, 178-179:2–32, 2010.

[27] K. Kobayashi. *Nucl. Instrum. Methods Phys. Res. A*, 601:32–47, 2009.

[28] C Carbone and E Kisker. *Solid State Commun.*, 65:1107, 1988.

[29] Cherepkov N A. *Sov. Phys.-JETP*, 38:463, 1974.

[30] L. Baumgarten, C. M. Schneider, H. Petersen, F. Schaefers, and J. Kirschner. *Phys. Rev. Lett.*, 65:492, 1990.

[31] D. Venus. *Phys. Rev. B*, 48:6144, 1993.

[32] M. Getzlaff, Ch. Ostertag, G. H. Fecher, N. A. Cherepkov, and G. Schönhense. *Phys. Rev. Lett.*, 73:3030, 1994.

[33] N. A. Cherepkov, V. V. Kuznetsov, and V. A. Verbitskii. *J. Phys. B: At. Mol. Opt. Phys.*, 28:1221–1239, 1995.

[34] G. van der Laan and B. T. Thole. *Phys. Rev. B*, 52:15355, 1995.

[35] F. U. Hillebrecht, Ch. Roth, H. B. Rose, W. G. Park, E. Kisker, and N. A. Cherepkov. *Phys. Rev. B*, 53:12182, 1996.

[36] C M Schneider and J Kirschner. *Crit. Rev. Solid State Mater. Sci.*, 20(3):179–283, 1995.

[37] G. H. Fecher, V. V. Kuznetsov, N. A. Cherepkov, and G. Schönhense. *J. Electron Spectrosc. Relat. Phenom.*, 122:157, 2002.

[38] K. Blum. *Density Matrix Theory and Application*. Plenum, New York, 1981.

[39] B. T. Thole and G. van der Laan. *Phys. Rev. Lett.*, 67:3306, 1991.

[40] B. T. Thole and G. van der Laan. *Phys. Rev. B*, 44:12424, 1991.

[41] B. T. Thole and G. van der Laan. *Phys. Rev. B*, 50:11474, 1994.

[42] B. T. Thole and G. van der Laan. *Phys. Rev. B*, 49:9613, 1994.

[43] G. H. Fecher. *J. Elect. Spectros. Rel. Phenom.*, 114-116:1165, 2001.

[44] J. Kirschner. Polarized electrons at surfaces. In G. Hohler, editor, *Polarized Electrons at Surfaces*, volume 106 of *Springer Acts in Modern Physics*, page 155. Springer, Berlin, 1985.

[45] H.-J. Elmers. *Handbook of Magnetism and Advanced Magnetic Materials*. Wiley, New York, 2007.

[46] J. Sawler and D. Venus. *Rev. Sci. Instrum.*, 62(10):2409, 1991.

[47] J. Kessler. Polarized electrons. In *Polarized Electrons*, volume 1 of *Springer Series on Atoms and Plasmas*, page 299. Springer, Berlin, 1985.

[48] M. P. Seah and W. A. Dench. *Surf. Interface Anal.*, 1:2, 1979.

[49] M. Suzuki, N. Kawamura, M. Mizukami, A. Urata, H. Maruyama, S. Goto, and T. Ishikawa. *Jpn. J. Appl. Phys.*, 37:L1488, 1998.

[50] D. Yu, C. Math, M. Meier, M. Escher, G. Rangelov, and M. Donath. *Surface Science*, 601:5803, 2007.

[51] J. Kirschner and R. Feder. *Phys. Rev. Lett.*, 42:1008, 1979.

[52] D. Wang, C. Nordman, J. M. Daughton, Z. Qian, and J. Fink. *IEEE Trans. Magn.*, 40:2269, 2004.

[53] S. Cardoso, P. P. Freitas, C. de Jesus, and J. S. Soares. *J. Appl. Phys.*, 87:6058, 2000.

[54] X.-G. Zhang and W. H. Butler. *Phys. Rev. B*, 70:172407, 2004.

[55] R. Matsumoto, S. Nishioka, M. Mizuguchi, M. Shiraishi, H. Maehara, K. Tsunekawa, D. D. Djayaprawira, N. Watanabe, Y. Otani, T. Nagahama, A. Fukushima, H. Kubota, S. Yuasa, and Y. Suzuki. *Solid State Comm.*, 143:574–578, 2007.

[56] Y. M. Lee, J. Hayakawa, S. Ikeda, F. Matsukura, and H. Ohno. *Appl. Phys. Lett.*, 89:042506, 2006.

[57] J. Hayakawa, S. Ikeda, Y. M. Lee, F. Matsukura, and H. Ohno. *Appl. Phys.Lett*, 89:232510, 2006.

[58] Y. M. Lee, J. Hayakawa, S. Ikeda, F. Matsukura, and H. Ohno. *Appl. Phys. Lett.*, 90:212507, 2007.

[59] S. Ikeda, J. Hayakawa, Y. Ashizawa, Y. M. Lee, K. Miura, H. Hasegawa, M. Tsunoda, F. Matsukura, and H. Ohno. *Appl. Phys. Lett.*, 93:082508, 2008.

[60] J. D. Burton, S. Jaswal, E. Y. Tsymbal, O. N. Mryasov, and O. G. Heinonen. *Appl. Phys. Lett.*, 89:142507, 2006.

[61] J. Y. Bae, W. C. Lin, H. J. Kim, T. D. Lee, K. W. Kim, and T. W. Kim. *J. Appl. phys.*, 99:08T316, 2006.

[62] Y. Jang, C. Nam, K.-S. Lee, B. K. Cho, Y. J. Cho, K.-S. Kim, and K. Kim. *Appl. Phys. Lett.*, 91:102104, 2007.

[63] D. J. Kim, J. Y. Bae, W. C. Lim, K. W. Kim, and T. D. Lee. *J. Appl. phys.*, 101:09B505, 2007.

[64] J. J. Cha, J. C. Read, R. A. Buhrman, and D. A. Muller. *Appl. Phys. Lett.*, 91:062516, 2007.

[65] G. H. Fecher B. Balke, A. Gloskowskii, S. Ouardi, C. Felser, T. Ishikawa, M. Yamamoto, Y. Yamashita, H. Yoshikawa, S. Ueda, and K. Kobayashi. *Appl. Phys. Lett.*, 92:193513, 2008.

[66] H. Ebert and M. Battocletti. *Solid State Comm.*, 98:785, 1996.

[67] P. Soven. *Phys. Rev.*, 156:809–813, 1967.

[68] W. H. Butler. *Phys. Rev. B*, 31:3260, 1985.

[69] S. H. Vosko, L. Wilk, and M. Nusair. Accurate spin-dependent electron liquid correlation energies for local spin density calculations: a critical analysis. *Can. J. Phys.*, 58:1200, 1980.

[70] S. V. Karthik, Y. K. Takahashi, T. Ohkubo, K. Hono, S. Ikeda, and H. Ohno. *J. Appl. Phys.*, 106:023920, 2009.

[71] J. C. Slater. *Phys. Rev.*, 49:537, 1936.

[72] L. Pauling. *Phys. Rev.*, 54:899, 1938.

[73] J. Kübler. *Theory of Itinerant Electron Magnetism.* Clarendon Press, Oxford, 2000.

[74] G. H. Fecher, H. C. Kandpal, S. Wurmehl, C. Felser, and G. Schönhense. *J. Appl. Phys.*, 99:08J106, 2006.

[75] A. P. Malozemoff, A. R. Williams, and V. L. Moruzzi. *Phys. Rev. B*, 29:1620, 1984.

[76] R. A. de Groot, F. M. Müller, P. G. van Engen, and K. H. J. Buschow. *Phys. Rev. Lett.*, 50:2024, 1983.

[77] S. Picozzi, A. Continenza, and A. J. Freeman. *Phys. Rev. B*, 66:094421, 2002.

[78] P. J. Brown, K. U. Neumann, P. J. Webster, and K. R. A. Ziebeck. *J. Phys. Condens. Matter*, 12:1827, 2000.

[79] S. Zhang, P. M. Levy, A. C. Marley, and S. S. P. Parkin. *Phys. Rev. Lett.*, 79:3744, 1997.

[80] T. Miyajima, M. Oogane, Y. Kataka, T. Yamazaki, M. Tsukada, Y. Kataoka, H. Naganuma, and Y. Ando. *Appl. Phys. Lett.*, 92:192503, 2008.

[81] J. Schmalhorst, S. Kämmerer, M. Sacher, G. Reiss, A. Hütten, and A. Scholl. *Phys. Rev. B*, 70:024426, 2004.

[82] N. D. Telling, P. S. Keatley, G. van der Laan, R. J. Hicken, E. Arenholz, Y. Sakuraba, M. Oogane, Y. Ando, and T. Miyazaki. *Phys. Rev. B*, 74:224439, 2006.

[83] T. Ishikawa, T. Makurame, H. Kijima, K. i. Matsuda, T. Uemura, M. Arita, and M. Yamamoto. *Appl. Phys. Lett.*, 89:192505, 2006.

[84] T. Ishikawa, S. Hakamata, K. i. Matsuda, T. Uemura, and M. Yamamoto. *J. Appl. Phys.*, 103:07A919, 2008.

[85] T. Ishikawa, H.-X. Liu, T. Taira, K. i. Matsuda, T. Uemura, and M. Yamamoto. *Appl. Phys. Lett.*, 95:232512, 2009.

[86] H. Kitamura. *Rev. Sci. Instrum.*, 66:2007, 1995.

[87] H. Kitamura. *J. Synchrotron Radiat.*, 7:121, 2000.

[88] C. S. Fadley, D. A. Shirley, A. J. Freeman, P. S. Bagus, and J. V. Mallow. *Phys. Rev. Lett.*, 23:1397, 1969.

[89] P. Wernet, B. Sonntag, M. Martins, P. Glatzel, B. Obst, and P. Zimmermann. *Phys. Rev. A*, 63:050702, 2001.

[90] Y. M. Yarmoshenko, M. I. Katsnelson, E. I. Shreder, E. Z. Kurmaev, A. Slebarski, S. Plogmann, T. Schlatholter, J. Braun, and M. R. Neumann. *Eur. Phys. J. B*, 2:1, 1998.

[91] O. Gaier, J. Harmle, B. Hillebrands, M. Kallmayer, P. Pörsch, G. Schönhense, H. J. Elmers, J. Fassbender, A. Gloskovskii, C. A. Jenkins, C. Felser, E. Ikenaga, Y. Sakuraba, S. Tsunegi, M. Oogane, and Y. Ando. *Appl. Phys. Lett.*, 94:152508, 2009.

[92] G. H. Fecher, B. Balke, S. Ouardi, C. Felser, G. Schönhense, E. Ikenaga, J. Kim, S. Ueda, and K. Kobayashi. *J. Phys. D: Appl. Phys.*, 40:1576, 2007.

[93] S. Ouardi, A. Gloskovskii, B. Balke, C. A. Jenkins, J. Barth, G. H. Fecher, C. Felser, M. Gorgoi, M. Mertin, F. Schäfers, E. Ikenaga, K. Yang, K. Kobayashi, T. Kubota, M. Oogane, and Y. Ando. *J. Phys. D: Appl. Phys.*, 42:084011, 2009.

[94] B. Gyorffy. *Phys. Rev. B*, 5:2382, 1972.

[95] B. Hülsen, M. Scheffler, and P. Kratzer. *Phys. Rev. B*, 79:094407, 2009.

[96] S. Chadov, G. H. Fecher, C. Felser, J. Minár, J. Braun, and H. Ebert. *J Phys. D: Appl. Phys.*, 42:084002, 2009.

[97] M. Yamamoto, T. Ishikawa, T. Taira, G.-F. Li, K. i. Matsuda, and T. Uemura. *J. Phys.: Cond. Mat.*, 95:232512, 2010.

[98] S. Picozzi, A. Continenza, and A. J. Freeman. *Phys. Rev. B*, 69:94423, 2004.

[99] I. Lindau, P. Pianetta, S. Doniach, and W. E. Spicer. *Nature*, 250, 1974.

[100] K. Kobayashi, M. Yabashi, Y. Takata, T. Tokushima, S. Shin, K. Tamasaku, D. Miwa, T. Ishikawa, H. Nohira, T. Hattori, Y. Sugita, O. Nakatsuka A. Sakai, and S. Zaima. *Appl. Phys. Lett.*, 83:1005, 2003.

[101] S. Suga and A. Sekiyama. *Eur. Phys. J. Special Topics*, 169:227235, 2009.

[102] X. Kozina, S. Ouardi, B. Balke, G. Stryganyuk, G. H. Fecher, C. Felser, S. Ikeda, H. Ohno, and E. Ikenaga. *Appl. Phys. Lett.*, 96:072105, 2010.

[103] S. Ueda, H. Tanaka, J. Takaobushi, E. Ikenaga, J.-J. Kim, M. Kobata, T. Kawai, H. Osawa, N. Kawamura, M. Suzuki, and K. Kobayashi. *Appl. Phys. Exp.*, 1:077003, 2008.

[104] S. Ouardi, G. H. Fecher, X. Kozina, G. Stryganyuk, B. Balke, C. Felser, E. Ikenaga, T. Sugiyama, N. Kawamura, M. Suzuki, and K. Kobayashi. *Phys. Rev. Lett.*, 107:036402, 2011.

[105] M. Masuda, T. Uemura, K. i. Matsuda, and M. Yamamoto. *IEEE Trans. Magn.*, 44:3996, 2008.

[106] T. Marukame, T. Ishikawa, S. Hakamata, K. i. Matsuda, T. Uemura, , and M. Yamamoto. *Appl. Phys. Lett.*, 90:012508, 2007.

[107] W. Wang, H. Sukegawa, R. Shan, S. Mitani, and K. Inomata. *Appl. Phys. Lett.*, 95:182502, 2009.

[108] J. G. Tobin, K. W. Goodman, F. O. Schumann, R. F. Willis, J. B. Kortright, J. D. Denlinger, E. Rotenberg, A. Warwick, and N. V. Smith. *Surf. Sci.*, 395:L227, 1998.

[109] J. Henk, A. M. N. Niklasson, and B. Johansson. *Phys. Rev. B*, 59:13986, 1999.

[110] J. Bansmann, L. Lu, K. H. Meiwes-Broer, T. Schlathölter, and J. Braun. *Phys. Rev. B*, 60:13860, 1999.

[111] G. van der Laan and B. T. Thole. *Phys. Rev. B*, 48:210, 1993.

[112] G. van der Laan, S. S. Dhesi, and E. Dudzik. *Phys. Rev. B*, 61:12277, 2000.

[113] G. H. Fecher. *Europhys. Lett.*, 29:605, 1995.

[114] G. Panaccione, G. Cautero, M. Cuatero, A. Fondacaro, M. Grioni, P. Lacovig, G. Monaco, F. Offi, G. Paolicelli, M. Sacchi, N. Stojie, G. Stefani, R. Tommasini, and P. Torelli. *J. Phys.: Condens. Matter*, 17:2671, 2005.

[115] D. Venus. *Phys. Rev. B*, 56:2661, 1997.

[116] T. Nakagawa and T. Yokoyama. *Phys. Rev. Lett.*, 96:237402, 2006.

[117] K. Hild, J. Maul, G. Schönhense, H. J. Elmers, M. Amft, and P. M. Oppeneer. *Phys. Rev. Lett.*, 102:057207, 2009.

[118] G. Rossi, G. Panaccione, F. Sirotti, S. Lizzit, A. Baraldi, and G. Paolucci. *Phys. Rev. B*, 55:11488, 1997.

[119] S. Wurmehl, G. H. Fecher, K. Kroth, F. Kronast, H. A. Dürr, Y. Takeda, Y. Saitoh, K. Kobayashi, H.-J. Lin, G. Schönhense, and C. Felser. *J. Phys. D: Appl. Phys.*, 39:803–815, 2006.

[120] R. Richter and H. Eschrig. *J. Phys. F: Met. Phys.*, 18:1813–1825, 1988.

[121] E. Stavitski and F. M. F. de Groot. *Micron*, 41:687–694, 2010.

[122] C. T. Chen, F. Sette, Y. Ma, and S. Modesti. *Phys. Rev. B*, 42:11, 1990.

[123] C. T. Chen, Y. U. Idzerda, H.-J. Lin, N. V. Smith, G. Meigs, E. Chaban, G H. Ho, E. Pellegrin, and F. Sette. *Phys. Rev. Lett.*, 75:1, 1995.

[124] H. J. Elmers, G. H. Fecher, D. Valdaitsev, S. A. Nepijko, A. Gloskovskii, G. Jakob, G. Schönhense, S. Wurmehl, T. Block, C. Felser, P.-C. Hsu, W.-L. Tsai, and S. Cramm. *Phys. Rev. B*, 67:104412, 2003.

[125] H. J. Elmers, S. Wurmehl, G. H. Fecher, G. Jakob, C. Felser, and G. Schönhense. *Appl. Phys. A*, 79:557–563, 2004.

[126] C. Felser, B. Heitkamp, F. Kronast, D. Schmitz, S. Cramm, H. A. Dürr, H.-J. Elmers, G. H. Fecher, S. Wurmehl, T. Block, D. Valdaitsev, S. A. Nepijko, A. Gloskovskii, G. Jakob, G. Schönhense, and W. Eberhardt. *J. Phys.: Condens. Matter*, 15:7019–7027, 2003.

[127] S. Wurmehl, G. H. Fecher, H. C. Kandpal, V. Ksenofontov, C. Felser, H.-J. Lin, and J. Morais. *Phys. Rev. B*, 72:184434, 2005.

[128] S. Wurmehl, G. H. Fecher, H. C. Kandpal, V. Ksenofontov, C. Felser, and H.-J. Lin. *Appl. Phys. Lett.*, 88:032503, 2006.

[129] J. Zegenhagen, B. Detlefs, T.-L. Lee, S. Thiess, H. Isern, L. Petit, L. Andre, J. Roy, Y. Mi, and I. Joumard. *J. Electron Spectrosc. Relat. Phenom.*, 178-179:258–267, 2010.

[130] P. Carra and M. Altarelli. *Phys. Rev. Lett.*, 64:1286, 1990.

[131] C. S. Fadley and D. A. Shierley. *Phys. Rev. A*, 2:1109, 1970.

[132] R. Shan, H. Sukegawa, W. H. Wang, M. Kodzuka, T. Fukrubayashi, T. Ohkubo, S. Mitani, K. Inomata, and K. Hono. *Phys. Rev. Lett.*, 102:246601, 2009.

[133] X. Kozina, G. H. Fecher, G. Stryganyuk, S. Ouardi, B. Balke, C. Felser, G. Schönhense, E. Ikenaga, T. Sugiyama, N. Kawamura, M. Suzuki, T. Taira, T. Uemura, M. Yamamoto, H. Sukegawa, W. Wang, K. Inomata, and K. Kobayashi. *Phys. Rev. B*, 036402, 2011.

[134] F. de Groot and A. Kotani. Core level spectroscopy of solids. In *Core Level Spectroscopy of Solids*, volume 6 of *Advances in Condensed Matter Science*, page 490. CRC Press, Boca Raton, 2008.